PRECURSORY ERUPTIONS, MAGMA PRIMING AND ERUPTION DYNAMICS ASSOCIATED WITH THE CLIMACTIC 19TH FEBRUARY 1975 ERUPTION OF NGAURUHOE

A thesis

submitted in partial fulfilment

of the requirements for the degree

of

***Master of Science* in Earth Science**

at

The University of Waikato

by

Krystal Joan Geraghty

THE UNIVERSITY OF
WAIKATO
Te Whare Wānanga o Waikato

2019

Abstract

Ngauruhoe is an active central North Island composite volcano, located at the south end of the Taupo Volcanic Zone. This basaltic andesite to andesite cone is one of the most active vents of the larger Tongariro Volcanic Complex; the active summit scoria cone (c. 150 m in diameter) was constructed within the older crater (c. 400 m in diameter) during the eruptions of 1954 to 1975. Approximately 9 m of volcanic material was added to the inner crater rim during the 1975 eruption. Past eruptions from Ngauruhoe have been well-documented in various studies; however, these generally lack detailed observation and analyses of the 1975 eruption deposit meaning that pre-eruptive conditions and explosion dynamics associated with this eruption were left poorly constrained.

This research investigates the physical parameters and eruption controls that led up to the 1975 eruption, including the activity observed from 1968. Specifically, this study examines the pre-eruptive conditions, triggers and eruption mechanisms that led to eruption and emplacement of the 1975 inner crater rim deposit. A key part of this study involved identifying the relationship between, and source of, different clast types comprising the deposit, in addition to determining whether a solid plug and/or magma-water interaction contributed to the high explosivity of the 1975 eruption. By improving our understanding of magmatic and volcanic processes associated with this eruption, this study may assist with more reliable interpretation of monitoring data prior to and during such eruptions (not only at Ngauruhoe, but also basaltic-andesitic volcanoes worldwide). Fieldwork involved stratigraphic logging, high-resolution photography, and sample collection, in addition to sub-sample collection of the 1954-75 volcanic ash deposits stored on archive at GNS Science. Outcrop photos were subsequently point-counted to discriminate between the components, and collected samples described and characterised. Further laboratory analyses included optical microscopic petrography, component point counting, vesicularity studies, scanning electron microscopy, electron microprobe analysis, laser sizing, and quantitative software shape analysis.

This study has demonstrated the importance of crystal fractionation and magma mixing in the evolution of the magma that erupted during 1975. In particular, the transporting magma may have interacted with, and entrained, exotic crystals from a cooler, more evolved crystal mush zone formed by an antecedent magma. Further, magma ascent was associated with efficient gas segregation and transport to the surface along preferential percolation pathways. Efficient degassing in low viscosity magmas typically results in effusive activity; however, this study shows that the high explosivity of the climactic 19th February 1975 eruption was linked to the presence of a coherent, degassed, and hydrothermally altered caprock resulting in accumulation and coalescence of pressurised gas beneath the plug. This study discounts the previously ascribed theory that magma-water interaction controlled the high explosivity of this event. Instead, limited magma-water interaction likely produced the steam observed in the eruption column.

Based on the interpretations outlined above, it is now possible to explain the inner crater stratigraphy. The 1975 inner crater rim deposit is now divided into four facies, A through D, based on textural characteristics and componentry. Facies A (comprising dense sub-angular lapilli and vesicular scoria lapilli) and B (comprising black scoria lapilli/bombs and dense lapilli) were emplaced during vulcanian activity associated with disruption of a caprock, leading up the climactic eruption on the 19th of February 1975. Facies C (comprising loose scoria, dense lapilli, and large irregular domains of densely coalesced/agglutinated pyroclasts) and D (comprising dense lapilli to blocks, scoria lapilli, and bombs) were deposited during the continuous 'sub-plinian' eruption on the 19th of February 1975, from strombolian fire-fountaining activity at the base of the large eruption plume. Evidence for this is recorded by the mixture of scoria, agglutinated spatter, and dense clasts throughout these facies; which are indicative of a spatter-fed eruption.

Acknowledgements

I would like to thank the Department of Earth and Ocean Sciences at the University of Waikato (UoW) for the education I have gained during my five years as a student. There have been many ups and downs, but I have learnt so much and achieved more than I ever imagined I could. My biggest appreciation goes to my two incredible supervisors; Dr Adrian Pittari (UoW) and Dr Geoff Kilgour (GNS Science). This whole project would not have been possible without their ongoing knowledge, guidance, support, and patience. I am very grateful and will never be able to thank you both enough.

Thank you to Dr Geoff Kilgour and Annette Rodgers for assisting me in the field, both with sample collection and high-resolution photography of the 1975 inner crater rim deposit. I would also like to thank Kirsty Vincent and ChrisAnne Ross for their support on my second trip (it was an interesting hike to say the least!!). Thank you to the Department of Conservation (DoC) and Bubs Smith of the Ngāti Hikairo Iwi for granting us permission to carry out scientific research on a mountain of such high cultural and spiritual significance. Undertaking fieldwork on Ngauruhoe was an incredible experience and one that I will never forget.

I would also like to thank the EQC Earthquake Commission for providing funding towards this research project which covered helicopter costs for fieldwork, a weeks' worth of work on the electron microprobe, and accommodation for a second field trip. I am very grateful to have also received financial assistance from the UoW Research Masters Scholarship, the Science and Engineering Masters Fees Award, the UoW Taught Postgraduate Scholarships, the Broad Memorial Fund, the UoW Masters Student Grant, and the Hastie Research Award from the Geoscience Society of New Zealand. These sources of financial support have covered costs associated with research at GNS Science in Taupo and microprobe use in Wellington (including travel and accommodation costs), printing and binding thesis expenses, and living costs during the duration of this degree.

Thank you to the technicians who assisted with laboratory work including Kirsty Vincent, Annette Rodgers, Renat Radosinsky, and Helen Turner (UoW), and also

Dr Ian Schipper (Victoria University of Wellington). I am also very thankful for the assistance I received from Cheryl Ward (Academic Liaison Librarian) when it came to endnote and thesis formatting. You are a fantastic human being!

Last but not least, this massive feat would not have been possible without the support from my amazing family and friends. In particular, I would like to thank my Mum (Robyn Geraghty) and Dad (Bruno Geraghty), my partner (Callum Brown), and my friend and fellow volcanology buddy, ChrisAnne Ross. These people have truly been my rocks throughout this journey. Thank you all so very much, I could not have done it without you!

I would like to finish with some of my favourite quotes from my support team:

Bruno Geraghty: *"It's not rocket science, it's just rocks"*

Adrian Pittari: *"Volcanology is 1% inspiration, 99% perspiration"*

Table of Contents

List of Figures

List of Tables

Chapter One

Introduction

1.1 Introduction

1.1.1 Composite Cones and their Hazards

Composite cones are typically associated with intermediate to silicic magma (although mafic basaltic compositions are also possible) and can erupt both effusively (lava flows) and explosively (strombolian, vulcanian, subplinian and plinian eruptions) (de Silva & Lindsay, 2015). Eruptive behaviour has strong implications for the consequent volcanic hazard(s) most likely associated with a particular volcano; therefore, research aimed at better understanding the processes associated with the behaviour of frequently active cones has obvious significance (Hobden *et al.*, 2002). Ngauruhoe is a frequently active composite cone in New Zealand which has displayed a variety of eruptive styles over its eruptive history, making it an ideal volcano to study the eruptive styles and dynamics of a young composite cone (in addition to the well-preserved and relatively accessible lava flows and inner crater deposits). The study of eruption deposits may assist with interpreting pre-eruptive magma conditions and processes which lead to certain eruptive behaviour and emplacement processes, and the knowledge obtained may subsequently be applied to other open-system composite volcanoes worldwide.

1.1.2 Ngauruhoe Volcano

Ngauruhoe is an active basaltic-andesite to andesite (54.2–58.6 wt. % SiO_2) composite volcano in the central North Island of New Zealand, which has displayed a diverse range of eruption styles over very short time scales (Hobden *et al.*, 2002). Ngauruhoe erupted frequently between 1839 and 1975, with 73 eruptions of size greater than 10^5 m^3 recorded within this time frame (Bebbington & Lai, 1996). Activity has comprised effusive lava flows, strombolian-style eruptions, vulcanian-style explosions, and subplinian activity during the climactic 1975 eruption (producing a higher, more sustained eruption column) (Hobden *et al.*, 2002). There

have been no further significant eruptions since 1975, with only minor activity in 1977.

The past eruptions of Ngauruhoe have been well-documented; however, detailed observations and analyses of the 1975 eruption deposits are minimal. For example, Nairn *et al.,* (1976) and Nairn and Self (1978) describe the 1975 eruption from observations and distal eruption deposits when it would have been too dangerous to access the deposits in the crater. Some articles involve regional studies of Tongariro but do not focus specifically on the 1975 Ngauruhoe eruption, such as Greve *et al.* (2016), Hill *et al.* (2015), Miller and Williams-Jones (2016), Moebis *et al.* (2011) and earlier work by Hobden *et al.* (1996). Krippner (2009) studied the overall stratigraphy and eruption styles of the 1954-75 summit cone of Ngauruhoe, with emphasis on the 1954-55 eruptions. Therefore, the pre-eruptive conditions and explosion dynamics of the 1975 climactic eruption are not well understood, and related deposits have not been described and quantified in significant detail.

1.1.3 Justification for Research

This research addresses some key questions (outlined below) which arise from knowledge gaps within the relevant literature/previous work.

- What were the priming conditions, triggers, and eruption mechanisms that led to the 1975 eruptions of Ngauruhoe?
- Was there a solid plug remaining after the 1954-55 eruption, and did this contribute to the high explosivity of the climactic 1975 eruption?
- What is the relationship between, and source of, different clast types that make up the 1975 agglutinate (e.g. the scoria, fluidal spatter, and dense blocks that are intermixed within the deposits)?
- Was water-magma interaction the main trigger involved in the 1975 eruption, as suggested by Nairn and Self (1978)?
- Was juvenile magma involved in all eruptions that occurred between 1968-1975?
- What characteristics allow some andesitic magmas to generate eruptions with strombolian-style characteristics?

This study should assist with understanding the potential hazard of Ngauruhoe and other vents across the Tongariro Volcanic Complex. Better knowledge of priming conditions, triggers and eruption mechanisms may also assist with interpreting monitoring signals prior to and during such eruptions. This has significant implications to the safety of hundreds of people walking the Tongariro Alpine Crossing each day, and the findings may therefore be of interest to GNS Science and the Department of Conservation (DOC) for monitoring and land management purposes.

1.2 Research Aim and Objectives

The aim of this project is to determine the physical parameters and eruption controls that led to the explosive 1968 to 1975 eruptions of Ngauruhoe, particularly the pre-eruptive conditions and processes that led to the eruption and emplacement of the 1975 crater rim deposit. There are three main objectives which will assist in achieving the overall aim for this research:

1) to reconstruct stratigraphy and facies characteristics (including the geometry, textural characteristics, spatial variations, and componentry) of the 1975 deposit, and characterise and correlate distal ring plain deposits from eruptions leading up to and including the 1975 eruption;
2) to characterise and quantify the morphologies, textures, and petrographic components of the different clasts that make up the 1975 eruption deposit, in addition to the components and morphologies of the distal 1954-1975 ash samples; and
3) to characterise the detailed mineral and glass chemistry from the 1975 deposit.

1.3 Methodology

To achieve the objectives listed above, the following methods were involved: (1) stratigraphic logging, lithological outcrop descriptions, and sample collection of the 1975 eruption deposit, in addition to sub-sample collection of the 1954-1975 volcanic ashes stored on archive at GNS Science, (2) point counting of outcrop photos, and describing and characterising outcrop hand specimens and archive

ash samples, and (3) laboratory analyses, including optical microscopic petrography, component point counting, vesicularity studies, scanning electron microscopy (SEM), electron microprobe analysis (EPMA), laser sizing, and quantitative software shape analysis.

Each of these methods are presented in further detail within their relevant chapters, and raw data obtained are provided in the appendices.

1.4 Study Area

Ngauruhoe is a steep-sided, symmetrical, andesitic-basaltic composite cone, with a summit crater and nested summit cone reaching 2,287 m above sea level. It is situated approximately 25 km south-west of Turangi on Lake Taupo's southern shore (Figure 1.1) and is one of three central North Island volcanoes that delineate the southern limit of the Taupo Volcanic Zone (in addition to Ruapehu and Tongariro). During New Zealand's winter months Ngauruhoe is typically snow-covered, although snow can fall as early as March or as late as November. Patches of unmelted snow can sometimes still be present within the crater during summer despite the warmer weather and lack of snow fall.

Figure 1.1 The location of Mount Ngauruhoe (red locality symbol) within the central North Island of New Zealand, in relation to seven main population centres (*Mount Ngauruhoe, New Zealand*, 2019).

The focussed study area is located at the top of the inner crater rim, within the 1975 eruption deposit forming a vertical bluff on the northern and northeastern sections. It is accessible either by foot or by helicopter. Helicopter transport to and from the investigation site was particularly useful on the first trip for this project;

minimising time constraints in the field and assisting with sample removal. However, this was not financially feasible for the second trip and a day-hike was necessary to complete the fieldwork. Both field work missions were undertaken when snow was absent (from the end of January to mid-February), providing maximum visibility and accessibility to the 1975 crater rim deposit.

1.5 Thesis Structure and Chapter Outline

Chapter two is a review of literature and previous work relevant to this study. It provides the geological setting and an overview of Ngauruhoe, including its eruptive history, summit crater evolution, patterns of cone growth, inferences regarding the underlying magma system, and general petrography. The most recent and relevant previous work on Ngauruhoe is also summarised at the end of this chapter.

Chapter three addresses the first objective, including deposit morphology descriptions, stratigraphic logging and facies descriptions, basic identification of the 1975 clast types, and detailed quantification of the deposits from high resolution photographs. This chapter also characterises the 1954-1975 distal ash samples by compiling collection information, visual colour and grainsize characteristics, and laser sizer data.

Chapter four addresses the second objective and includes detailed analyses of the 1975 clasts; including petrographic descriptions and point counting of components under the optical microscope, SEM analyses (to further describe/illustrate morphologies, textures, and petrographic components), and quantitative vesicularity studies. The second part of chapter four includes clast shape, size, and componentry analyses of the 1954-1975 ash samples via stereoscopic observations, X-ray powder diffraction (XRD), SEM imagery, and image processing.

Chapter five addresses the third objective by presenting more detailed mineral and glass chemistry data for both the 1975 crater rim samples and the 1954-1975 distal ash samples from electron microprobe analyses. This chapter also provides

an estimate of the eruptible 1975 magma temperature based on equilibrium clinopyroxene-liquid geothermometry.

Finally, a discussion of findings is presented in chapter six, followed by a summary of the key conclusions and suggestions for future work in chapter seven.

Chapter Two

Literature Review and Previous Work

2.1 Geological Setting

2.2 New Zealand

New Zealand is located in the southwest Pacific Ocean and it straddles the Australian and Pacific plate boundary. This complex plate boundary is globally unique because of the variation along the arc from north to south. In the northern portion, oblique, westwards subduction of the Pacific Plate transitions to strike-slip south of Wellington, while in the far SW corner, eastward subduction of the Pacific Plate occurs (Bibby *et al.*, 1995).

2.3 Taupo Volcanic Zone (TVZ)

The oblique subduction is rotating the eastern North Island clockwise, leading to arc rifting which is partially represented by the TVZ. This subduction is occurring at a relative convergence rate of approximately 50 mm yr^{-1} (Figure 2.1) (Bibby *et al.*, 1995; Graham *et al.*, 1995; Wilson *et al.*, 1995). The TVZ is characterised by a northeast-trending volcanic arc and high rates of magma production in association with this subduction, combined with extension (Bibby *et al.*, 1995) and is c. 300 km long, and up to 60 km in width (Wilson *et al.*, 1995). As a result of the extension (occurring at c. 7 mm yr^{-1}) and active faulting, the continental crust within TVZ region is relatively thin (only 12-15 km thick) (Wilson *et al.*, 1995; Bibby *et al.*, 2002; Price *et al.*, 2005; Cassidy *et al.*, 2009). High magma production, combined with the thin crust has led to a high heat flow, and most of the North Island's geothermal fields lie within the central 6000 km^2 of the TVZ (which has an average heat flux of 700 mW m^{-3}) (Bibby *et al.*, 1995).

According to Wilson *et al.* (1995) andesitic volcanism in the TVZ began around 2 Ma, while significant rhyolitic activity (plus minor dacitic and basaltic activity) commenced around 1.6 Ma. The volcanic rocks of the TVZ can be separated into four main compositional groups. These include rhyolite (the most dominant magma erupted within the TVZ, with a bulk volume ≥ 15,000 km^3), andesite (an

order of magnitude less abundant than rhyolite), and the minor high-alumina basalt and dacite series (each <100 km^3) (Graham *et al.*, 1995; Wilson *et al.*, 1995). Volcanism at the northern and southern ends of the TVZ is dominated by andesitic composite volcanoes (Edgecumbe, Whale Island and White Island to the north, and the Ruapehu-Tongariro complex to the south) (Bibby *et al.*, 1995; Wilson *et al.*, 1995). Between these zones, there is a central segment approximately 125 km in length which is predominantly rhyolitic and characterised by rhyolitic domes, ignimbrite deposits, and collapse calderas (Bibby *et al.*, 1995; Wilson *et al.*, 1995). This segment of the TVZ is one of the most productive rhyolitic volcanic centres on Earth, with rhyolite making up more than 90% of the total extrusive magma flux from the TVZ (Graham *et al.*, 1995; Wilson *et al.*, 1995).

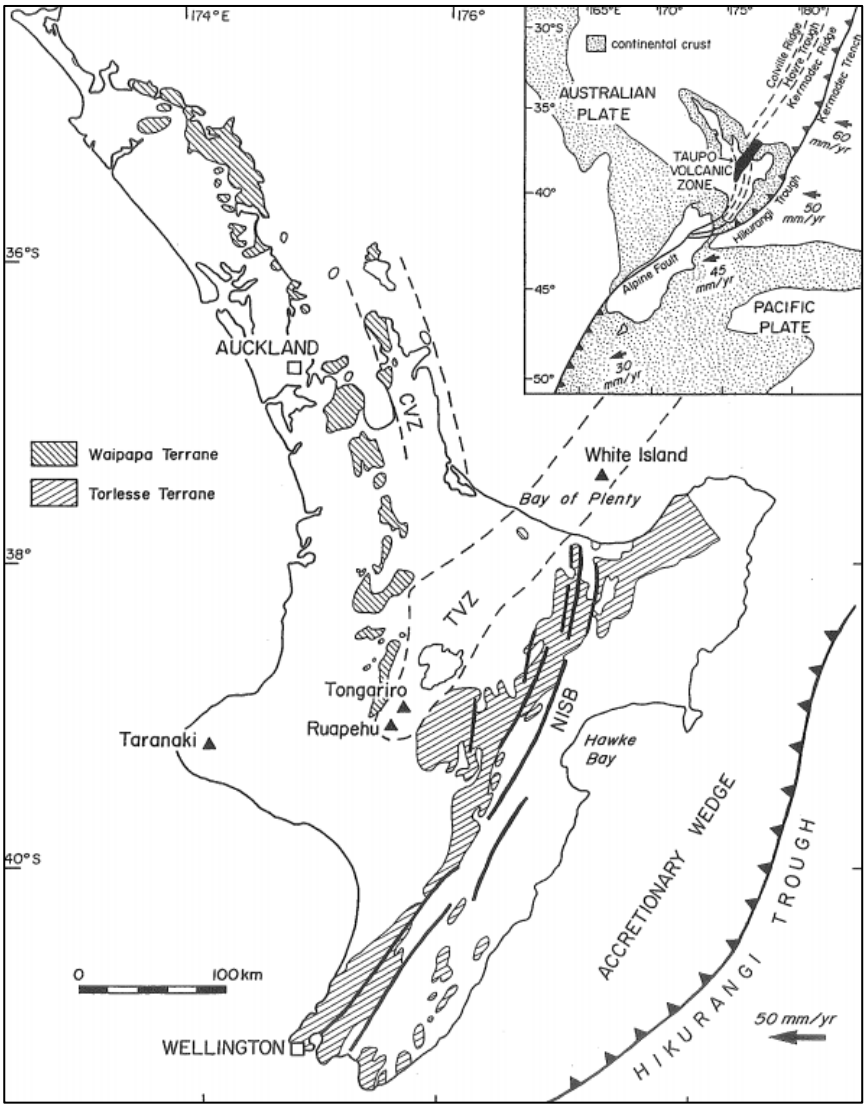

Figure 2.1. TVZ in relation to New Zealand's North Island, and its position relative to the Pacific and Australian plate boundary. The arrows in the map and inset show the direction and rate of the subducting Pacific Plate beneath the Australian Plate. CVZ = Coromandel Volcanic Zone. NSIB = North Island Shear Belt. Inset shows New Zealand straddling the plate boundary (with permission from Hobden, 1997, adapted from Graham *et al.,* 1995 and Cole, 1990).

2.4 Tongariro Volcanic Centre (TgVC)

The TgVC is located at the most southerly segment of the Taupo Rift structure, which is associated with extension within the TVZ (Villamor & Berryman, 2006; Cassidy *et al.*, 2009). Within this area the rift takes the form of a 40 km wide NNE-trending graben (Cassidy *et al.*, 2009). Most of the basement rock underlying the TgVC is complexly deformed and faulted Mesozoic sandstone and argillite metasediments of the Torlesse and Waipapa terranes (Figure 2.2) (Gregg, 1960; Cole, 1978; Graham *et al.*, 1995; Wilson *et al.*, 1995; Cassidy *et al.*, 2009; Alcaraz *et al.*, 2012). These greywacke basement rocks outcrop on both sides of the TVZ (Wilson *et al.*, 1995; Rowland & Sibson, 2001), and have been intersected in 69 drillholes in several geothermal fields (helping constrain their depth and continuation across the TVZ) (Alcaraz 2012). Younger Tertiary marine sediments overly basement rock on the western margin of the rift (Figure 2.2), and range in thickness from a few tens to a few hundreds of metres (Cassidy *et al.*, 2009).

The geology of the TgVC includes the two major massifs of Tongariro (total present volume ~75 km^3) and Ruapehu (total present volume ~110 km^3), and several smaller cones including Pihanga, Kakaramea, Ohakune, Hauhungatahi, Pukeonake, and Maungakatote (Figure 2.2) (Cole, 1978; Hobden *et al.*, 1996; Hobden, 1997; Cassidy *et al.*, 2009). Overlying Quaternary volcanic-derived deposits and ring-plain deposits, which fill the rift, are associated with these landforms (Figure 2.2) (Villamor & Berryman, 2006; Cassidy *et al.*, 2009). NNE-trending normal faults cut across the TgVC, and recent lavas have been erupted from vents which are also in a NNE-SSW alignment trending 027˚ (Cole, 1978; Hobden, 1997; Rowland & Sibson, 2001). Eruption of older lavas appears to have come from a NW-SE alignment of vents including Kakaramea and Pihanga (Figure 2.2) (Cole, 1978).

In addition to White Island, the most recent volcanic activity in the TVZ has been associated with some of the TgVC vents; including Te Maari (2012) and Ruapehu (2007) (Christenson *et al.*, 2010; Jolly *et al.*, 2010; Kilgour *et al.*, 2010; Breard *et al.*, 2014; Crouch *et al.*, 2014; Fitzgerald *et al.*, 2014; Fournier & Jolly, 2014; Godfrey *et al.*, 2014; Lube *et al.*, 2014; Procter *et al.*, 2014; Turner *et al.*, 2014).

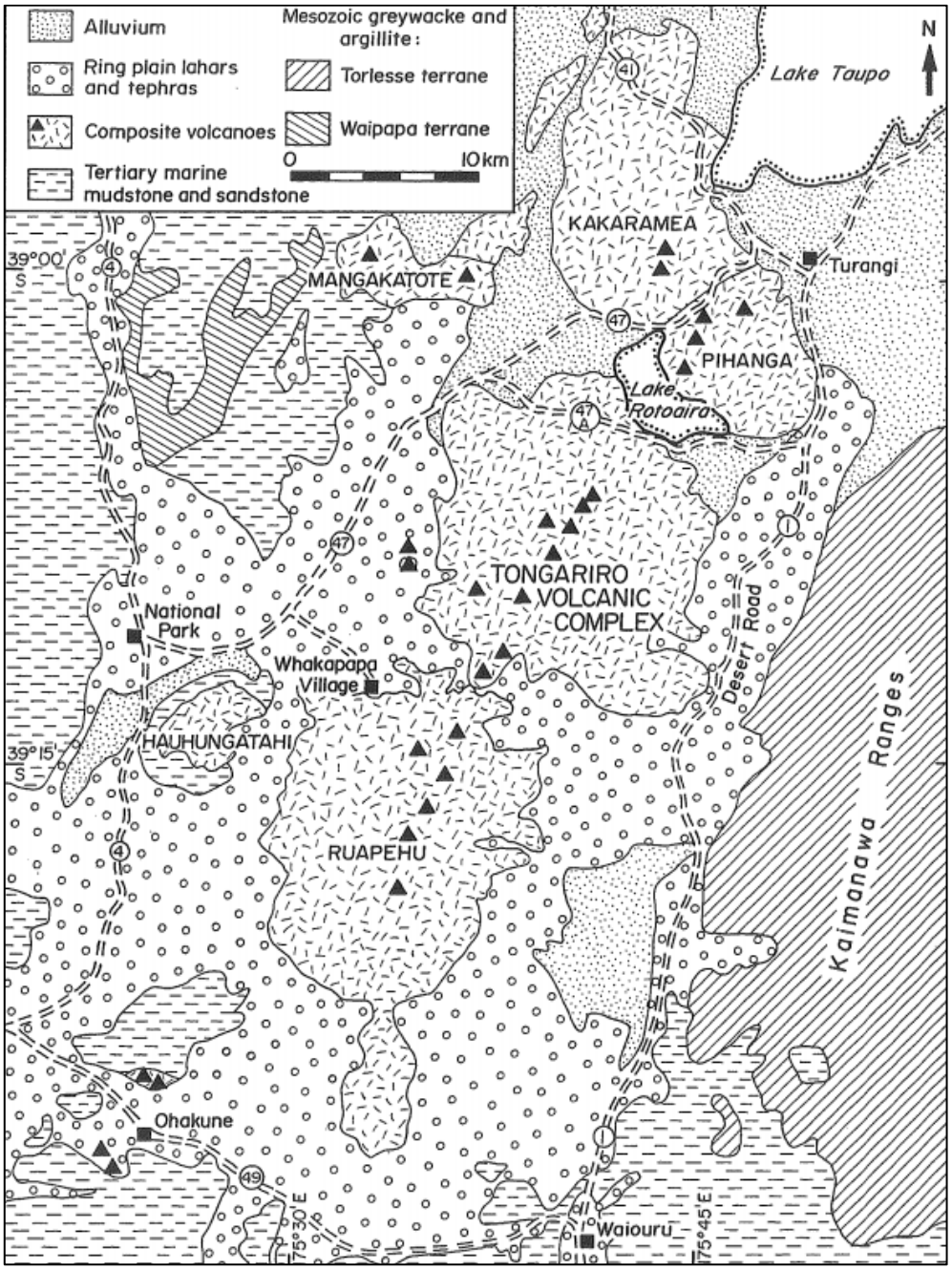

Figure 2.2. Map showing the various cones that make up the Tongariro Volcanic Centre (TgVC). The general geology of the TgVC and surrounding area is also displayed, including the distribution of Mesozoic basement terranes and Tertiary sediments. Main roads are also shown as double dashed lines (with permission from Hobden, 1997, adapted from Beetham & Watters, 1985, Hackett & Houghton, 1989, and Cole, 1990).

2.5 Tongariro Volcanic Complex

The Tongariro composite volcano is one of the volcanic complexes that constitutes the TgVC (Figure 2.2). A significant proportion of Tongariro is greater than 600 m high (1400 m above sea level, with a base level of 800 m) (Hobden, 1997). At least 12 volcanic vents coalesce and overlap within a 13 x 5 km vent corridor to form the complex (Figure 2.3) (Mathews, 1967; Hobden *et al.*, 1999; Arpa *et al.*, 2017).

In total the complex covers an area of approximately 200 km^2, with an eroded post-glacial volume of approximately 60 km^3 (not including the additional c. 15 km^3 of surrounding ring plain material) (Hobden, 1997; Hobden *et al.*, 2002). The Tongariro Volcanic Complex has been heavily eroded in the past by glaciations which have produced large U-shaped valleys (Manatepopo, Waihohonu and Oturere) and paired moraine ridges (Hobden, 1997). A recent PhD study by Eaves (2015) provides an important contribution to the earlier glacial history of Tongariro and Ruapehu, presenting the first age constraints and quantitative paleoclimate reconstructions for glacier fluctuations. Beneath the Tongariro massif, the basement forms a continuous, but faulted surface, as depicted in a gravity model by Miller and Williams-Jones (2016).

The time at which volcanism commenced at Tongariro is not exactly known. The oldest dated lavas suggest that volcanic activity commenced between 250-275 ka (Graham *et al.*, 1995; Hobden *et al.*, 1996). Lavas were originally divided into three groups by Mathews (1967) based on age. It is difficult to differentiate between his two younger groups, so volcanic activity at Tongariro has since been grouped into older pre-glacial (> 20,000 years ago) and younger post-glacial (<20,000 years ago) activity by Cole and Nairn (1975).

The younger post-glacial cones and craters of Tongariro roughly form a SW-NE lineation. This vent lineation includes the Te Maari Craters on the northern slopes (associated with the most recent activity), Red Crater, North Crater and Blue Lake crater in the central region, the Tama Lakes to the south, and Ngauruhoe to the southwest (Hobden, 1997). Ngauruhoe forms the highest part of the complex at 2,291 m above sea level (Nairn, 1976; Hobden, 1997; Hobden *et al.*, 2002). There are also ridges throughout the complex which are generally lower in relief compared to the younger cones, and have formed from the eroded remnants of older pre-glacial cones (Hobden, 1997).

Existing age information has been combined with K-Ar data deduced by Hobden *et al.* (1996) to show that the visible portion of the Tongariro Volcanic Complex has grown reasonably steadily since 273 ka, but has also included periods of rapid and relatively short-lived cone growth. Some cones have grown in less than 10 ka

at rapid rates (c. 1 km^3 ka^{-1}), while others have grown over 50 ka at rates less than 0.1 km^3 ka^{-1} (Hobden *et al.*, 2002).

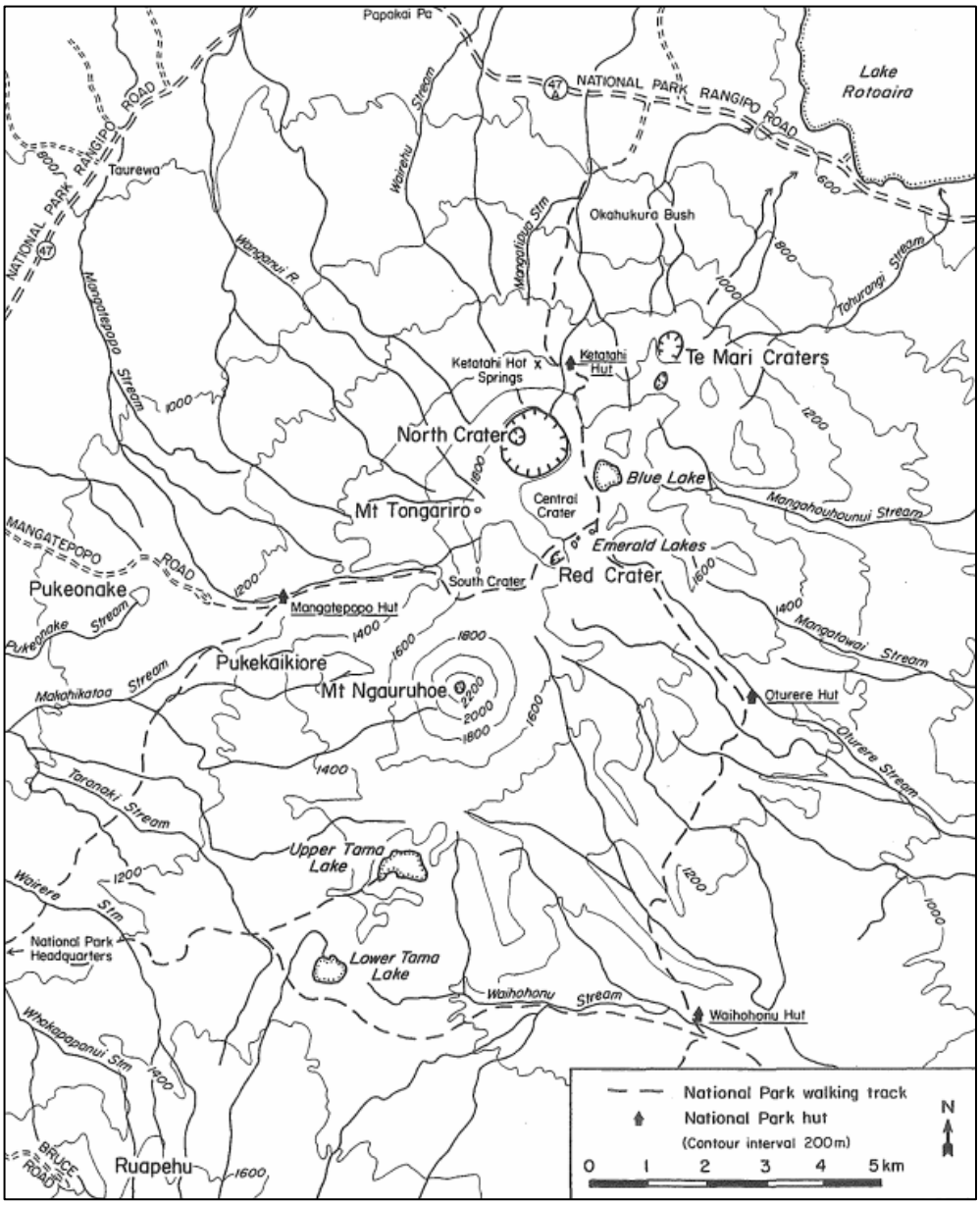

Figure 2.3 Map showing the topography and volcanic cones of the Tongariro Volcanic complex (Hobden, 1997).

Various vents across Tongariro were studied by Chizmar (2003), focussing on explosive eruptions and crater formation at Tama Lakes. Subsequently, Bardsley (2004) examined the deposits of Red Crater, while Basher (2005) explored the potential for hazards from the Te Maari Craters. Griffin (2007) analysed North Crater and associated products and processes of cone-building eruptions. Sanders (2010) studied the rheology and flow emplacement processes of the 1954 Ngauruhoe lavas, and Simons (2014) studied the volcanic history and eruption processes of Blue Lake Crater. This project will largely follow on from the MSc

research of Krippner (2009), in which the inner crater stratigraphy, componentry, petrography and geochemistry of the 1954-55 and 1974-75 eruptions of Ngauruhoe was studied.

Some of the recent research on Tongariro is included in a special issue of the Journal of Volcanology and Geothermal Research which was published in 2014. This comprises seventeen papers and focuses on the most recent Te Maari eruptions of 2012. The papers provide an account of the physical volcanology, hazard, impacts, and eruption management (including the risk management response, volcanic hazard mapping, and communication) (Cronin *et al.*, 2014; Jolly *et al.*, 2014c; Leonard *et al.*, 2014). Fitzgerald *et al.* (2014) mapped ballistic impact craters to create a calibrated 3D ballistic trajectory model which can be used to improve management of ballistic hazards at Tongariro. Other papers advance on pre-eruption framework and monitoring based on seismic precursors (Godfrey *et al.*, 2014; Hurst *et al.*, 2014) and recent compilations of historical accounts (Scott & Potter, 2014). This issue also includes papers regarding the eruption sequence, dynamics and mechanisms (Breard *et al.*, 2014; Efford *et al.*, 2014; Fournier & Jolly, 2014; Jolly *et al.*, 2014b; Lube *et al.*, 2014; Pardo *et al.*, 2014), plume dynamics (Crouch *et al.*, 2014; Turner *et al.*, 2014), and the pyroclastic flow that occurred (Jolly *et al.*, 2014a; Procter *et al.*, 2014).

Wadsworth *et al.* (2015) studied a basaltic-andesite dyke preserved in the eroded wall of a scoria cone at Red Crater and suggested that Strombolian eruptions may commonly conclude with magmatic drain-back following magma up-flow (based on textures and kinematic indicators). This may be important to note since Red Crater, Emerald Lake craters, and Ngauruhoe are all in a NNE-SSW alignment, and may be connected by dykes of similar orientation at depth (Wadsworth *et al.*, 2015).

There are also several recent geophysics papers on the internal structure of Tongariro. Hill *et al.* (2015) constructed a three-dimensional resistivity structure of Tongariro (including Ngauruhoe), and presented the first image of the hydrothermal and magmatic system underlying the volcano. The resistivity model depicts a shallow geothermal system and clear evidence for a shallow magma

accumulation zone (~4-12 km deep). It also shows a sub-vertical connection between the magma storage zone and overlying hydrothermal system, which is suggested to represent the preferable magma ascent path. Miller and Williams-Jones (2016) produced a new 3D geophysical model, providing a greater level of insight into the internal structure and extent of the hydrothermal system. They conclude that the hydrothermal system under Tongariro is constrained by faults which are unlikely to be associated with future eruptions since they do not appear to have acted as magmatic pathways in the past. Instead, their model suggests that the main area of magma ascent would likely be via a substantial magma feeder system beneath Ngauruhoe. This conclusion is consistent with the low resistivity zone imaged by Hill *et al.* (2015), and the low velocity zone depicted by Rowlands *et al.* (2005). Their model also agrees with Wadsworth *et al.* (2015) because there is a lack of high density anomalies associated with various vents across Tongariro, suggesting that magma drainage in the feeding conduit may be common at vents other than just Red Crater.

Greve *et al.* (2016) conducted a paleomagnetic study on Holocene lavas from the Tongariro Volcanic Centre to refine and reduce uncertainties in age estimates and improve the chronology of effusive eruptions from Tongariro. Twelve new paleo-direction estimates were constrained for Ngauruhoe lavas, and one new estimate was made for a lava flow from Red Crater.

2.6 Ngauruhoe Volcano

2.6.1 General Information on Ngauruhoe

Ngauruhoe is a composite cone located to the southwest of the Tongariro massif and is the largest and one of the most active vents of the larger Tongariro Volcanic Complex. Ngauruhoe is a basaltic andesite to andesite symmetrical composite cone, with steep flanks of about 30˚, and a height of approximately 900 m above the Tongariro saddle (2,287 m above sea level) (Hobden *et al.*, 2002). The growth of Ngauruhoe buried the remnants of several eroded older cones, and it is the morphology of those older cones that have essentially influenced the placement of lava flows and led to a sectoral cone growth pattern (Hobden *et al.*, 2002). Until recently it has been thought that eruptions and growth of Ngauruhoe began ~2.5

ka, as dated by the beech leaves within tephras of the Mangatawai Formation (Gregg, 1960; Topping, 1973; Hobden *et al.*, 2002). However, a paper published by Moebis *et al.* (2011) recognises a new minimum age for Ngauruhoe of 7,000 years ago. This is based on the geochemistry of at least 127 discrete tephra layers in ring-plain deposits that have been attributed to Ngauruhoe by a fine-resolution millimetre-scale stratigraphic approach. Ngauruhoe has grown to cover a total area of 15 km^2 with a volume of 2.2 km^3 (Hobden *et al.*, 2002; Moebis *et al.*, 2011).

2.6.2 Overview of Eruptive History

Ngauruhoe has been nearly continuously active since European arrival in New Zealand up until 1977, with eruptions occurring every 2 or 3 years (and typically persisting on the timescale of days to months) (Gregg, 1960; Hobden *et al.*, 2002; Hill *et al.*, 2015). Bebbington and Lai (1996) document 73 eruptions of size greater than 10^5 m^3 between 1839 and 1975. Eruptions from Ngauruhoe have been diverse, with eruption rates varying over one to two orders of magnitude (Figure 2.4), and any one eruption potentially displaying more than one eruption style (Bebbington & Lai, 1996; Hobden *et al.*, 2002). For example, the 1948-49 eruption was dominantly strombolian but some vulcanian activity was also observed (Hobden *et al.*, 2002).

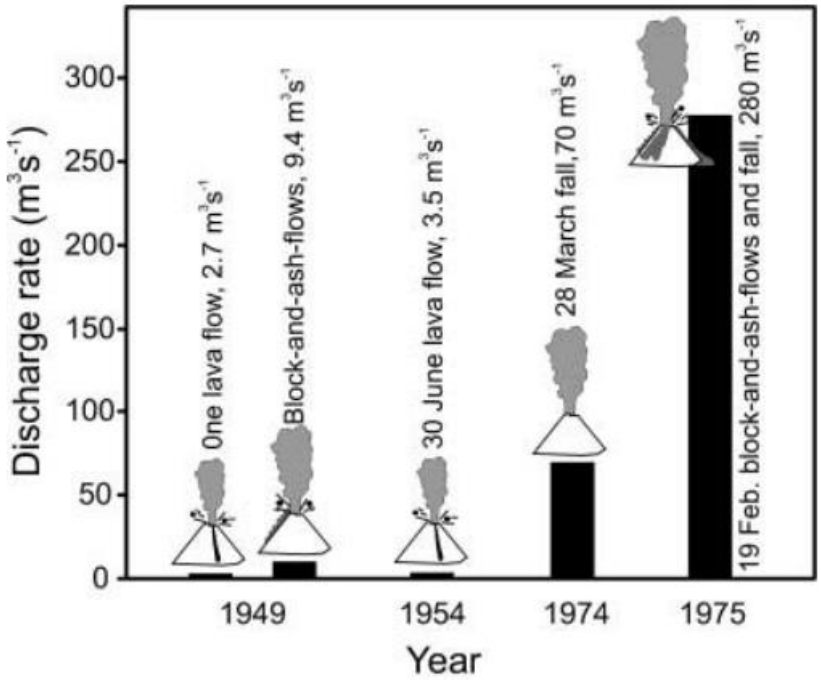

Figure 2.4 Variation in discharge rate (solid bars) for some of the significant historical eruptions from Ngauruhoe. The duration of activity is known for these eruptions, and the discharge rates are averaged over individual eruptive pulses of relatively unvarying intensity and eruption style (Hobden *et al.*, 2002).

Between 1870 and 1975, volcanism has ranged from strombolian (1954-55) to more explosive vulcanian and possibly subplinian activity (1974-75) (Hobden *et al.*, 2002). More effusive activity and a'a lava flows also occurred during the 1870, 1949 and 1954 events (Hobden *et al.*, 2002). Ngauruhoe has not had any further significant eruptions since 1975, and it is currently experiencing its longest period of quiescence since observations first began in 1839 (Hobden *et al.*, 2002). Only minor activity was recorded during 1977 and this predominantly involved steam emissions (Scott, 1977).

The first description of activity was by Bidwill (1841) who recounted a loud eruption in March 1839, involving voluminous and continuous steam emission and a black mushroom-shaped cloud. Many historical eruptions have been confined to emissions of ash and/or incandescent blocks (Hobden *et al.*, 2002), however the following section provides a brief summary of the more significant eruptions at Ngauruhoe since the initial observations of 1839.

1870

Significant activity (involving explosive eruptions, loud detonations, short-lived ash plumes, and ejection of incandescent scoria) commenced following 30 years of intermittent ash eruptions. Two lava flows were emplaced on the northern flank on the 7th of July, 1870 (Gregg, 1960; Cole & Nairn, 1975; Hobden *et al.*, 2002).

Lead up to 1948 activity

Several explosive eruptions occurred over the years between 1870 and 1948. However, Ngauruhoe experienced eight years of relative quiescence immediately prior to the commencement of major explosive activity in April-May 1948 (Allen, 1948; Cole & Nairn, 1975; Hobden *et al.*, 2002).

1948-1949

Strombolian eruptions were accompanied by loud detonations on the 30th of April 1948, and ash and incandescent blocks and bombs continued to be ejected over the following days. Low quantities of ash and steam were emitted following May 1948 until a major three-week eruptive episode began in February 1949 (Allen, 1948; Hobden *et al.*, 2002).

A violent vulcanian, vent-clearing explosion on the 9th of February produced a series of block-and-ash flows down the northwestern flank. During the night, lava overtopped the NW crater rim and resulted in a lava flow which did not cease until the morning of the 12th of February (Allen, 1949; Battey, 1949; Cloud, 1951; Gregg, 1960; Cole & Nairn, 1975). A period of vulcanian explosions and volcanic tremor at the end of February concluded the 1948-1949 eruptions (Allen, 1949; Hobden *et al.*, 2002).

Lead up to 1954-1955 activity

Ash eruptions occurred during November 1952 to July 1953. Ngauruhoe was relatively inactive following July 1953, although glowing red lava was observed in the crater during December 1953 (Gregg, 1956; Hobden *et al.*, 2002).

1954 -1955

Strombolian eruptions commenced on the 13th of May 1954. Similar intermittent ash eruptions (producing light ash clouds and intermittent fire fountaining) were a fairly constant feature during the remainder of May and the following nine months (Gregg, 1956; Cole & Nairn, 1975). Multiple lava flows were produced during this period, with approximately 10 million m^3 of lava extruded from Ngauruhoe between June and September of 1954 (Gregg, 1960; Briggs, 1981).

The level of volcanic activity varied over the 1954-55 period. Explosive activity and ash emission increased in September 1954, declined during October and November 1954, and increased again during December 1954 and January 1955. A pyroclastic flow and three lava flows were produced during the heightened September activity. Ash explosions continued into February but decreased towards the end of the month. The last explosion of 1955 was reported on the 10th of March, although incandescent lava remained in the crater until the 25th of June (Gregg, 1956; Cole & Nairn, 1975; Briggs, 1981; Hobden *et al.*, 2002).

Lead up to 1974/1975 activity

Semi-continuous steaming was the predominant activity at Ngauruhoe following the 1954-55 eruptions, however, intermittent small eruptions (largely involving recycled ash) also occurred during the late 1960's (Nairn *et al.*, 1976). Eruptive activity properly commenced in December 1972, and ash emission continued on several occasions during 1973. Despite only minor activity during July-October 1973, this period had heightened seismic activity. Petrographic analysis of ash samples showed no evidence of any fresh magmatic component (Nairn *et al.*, 1976). Another minor eruptive period took place from the 7-15th of December 1973; ash from this eruption contained a fresh glassy magmatic component, suggesting new andesitic magma was involved. The same was also found to be the case for the 1974-75 eruptions (Cole & Nairn, 1975; Nairn & Self, 1978).

1974-1975

The 1974-75 eruptions were predominantly vulcanian. Vulcanian activity occurred from the 22nd – 28th of January 1974, then recommenced on the 27th of March (Nairn *et al.*, 1976). The earlier January eruptions were vent-clearing and accompanied by large volcanic earthquakes, while eruptions that occurred in later January and March were not associated with any major volcanic earthquakes (indicating that open-vent conditions were responsible for the voluminous but non-explosive degassing) (Nairn *et al.*, 1976). Pyroclastic flows were also produced during January and March.

Following the March sequence there was an 11-month lull in activity until major ash emission commenced on the 12th of February 1975. The largest explosions of the 1974-75 episode were subplinian on the 19th of February 1975. Block-and-ash flows were associated with this eruption in addition to a large continuous eruption column that reached c. 10,000 m above the summit (Nairn & Self, 1978). Semi-plastic molten spatter was erupted, which can be seen draping the pre-existing crater rim and has added about 5 m to the eastern side of the inner cone (Nairn & Self, 1978). Nairn and Self (1978) suggest that phreatomagmatic processes are likely to have been involved during the 1975 eruptions, with explosions largely driven by phreatic steam rather than magmatic gases.

2.7 Summit Crater Evolution

At present, the summit of Ngauruhoe consists of two craters (Figure 2.5 F); an outer crater with a diameter of c. 400 m, and an inner crater (c. 150 m wide) which was constructed in the northwest sector of the original crater during the eruptions of 1954 to 1975 (Gregg, 1960; Hobden *et al.*, 2002). Prior to the 1850s, one large deep crater existed and any eruptions (since first recorded in 1839) were produced from this vent (Figure 2.5 A) (Gregg, 1960; Hobden *et al.*, 2002). According to Hobden *et al.* (2002), volcanic activity has likely been confined to the summit cone throughout history as there is no evidence that craters or parasitic cones have ever existed on the flanks of Ngauruhoe. During the 1870's, ash and lava were erupted from the scoria cone (Figure 2.5 B) which had grown in the northwest section of the main crater around the mid-1850's. An additional sub-crater was formed in the southern section of the main crater around 1881; this continued to grow at the expense of the northwest scoria cone and subsequent eruptions were focused from several vents within this sub-crater (Hobden *et al.*, 2002). The eruptions of 1948 to 1949 blanketed the summit in ash and lapilli which infilled the sub-craters (Figure 2.5 D), however the southern sub-crater was re-established during the 1954-55 eruptions (Figure 2.5 E). The northwest sub-crater was completely buried by the scoria cone which grew during this eruptive period (Figure 2.5 F) (Hobden *et al.*, 2002).

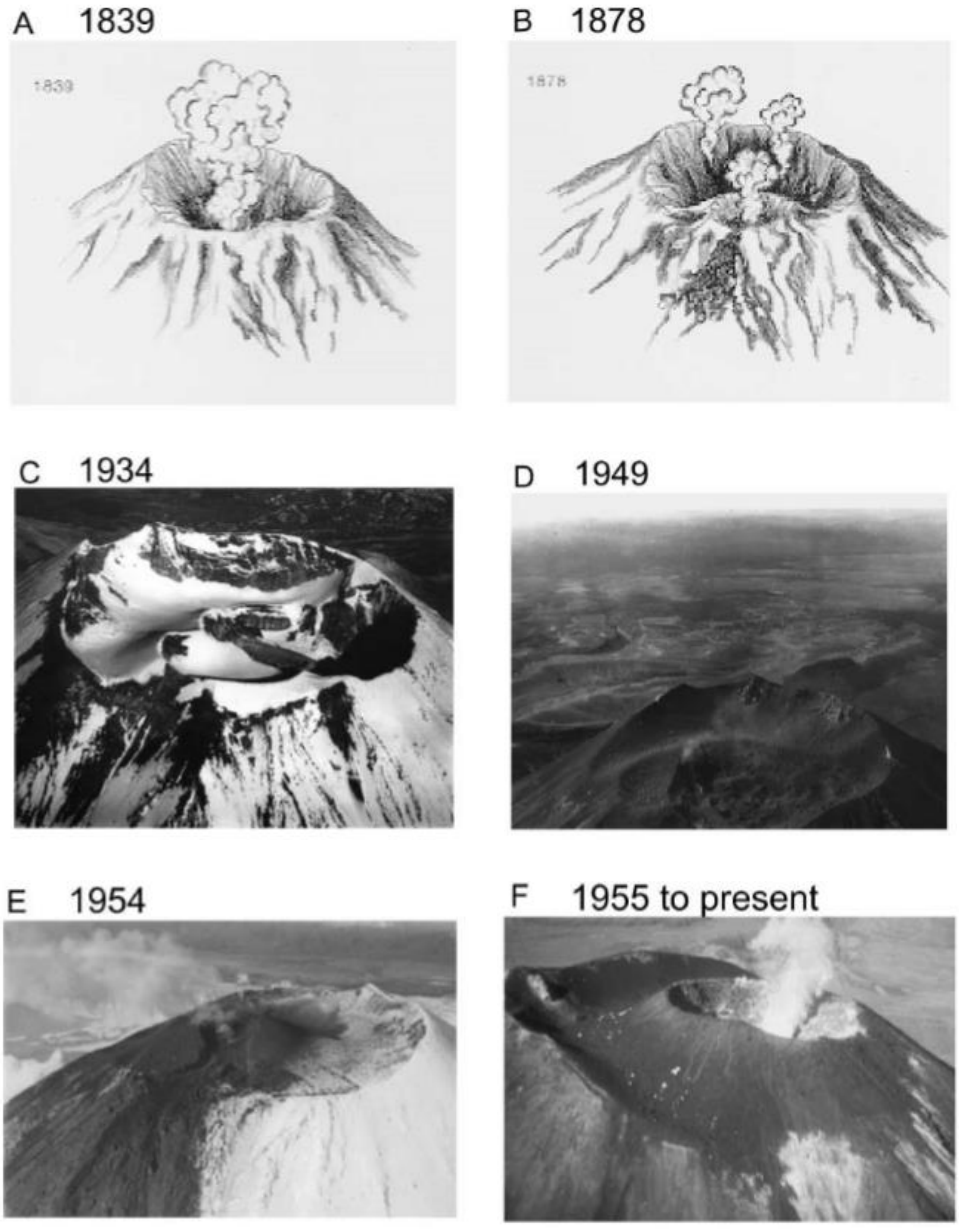

Figure 2.5 Morphological summit evolution of Ngauruhoe over time from 1839 (A) to 1955-present (F). All photos and sketches are viewed towards the southeast. Photos from GNS Science Wairakei, and sketches by Lloyd Homer in Williams (1989) are compiled here by Hobden *et al.,* (2002).

2.7.1 Patterns of Cone Growth

The distinctly symmetrical cone of Ngauruhoe has evolved in response to the pattern of lava flows and pyroclastic deposits over time. Lava emplacement is influenced by changes in crater geometry and morphology which is continually modified by the diverse eruption styles at Ngauruhoe (Figure 2.5). Chronologically distinct lava groups have generally been directed through the lowest points on the crater rim, and subsequently cone growth has followed a sectoral growth pattern

(Hobden *et al.*, 2002). According to Hobden *et al.* (2002), lava flows can be subdivided into five main groups which reflect flow chronology and their distinctive compositions (Figure 2.6).

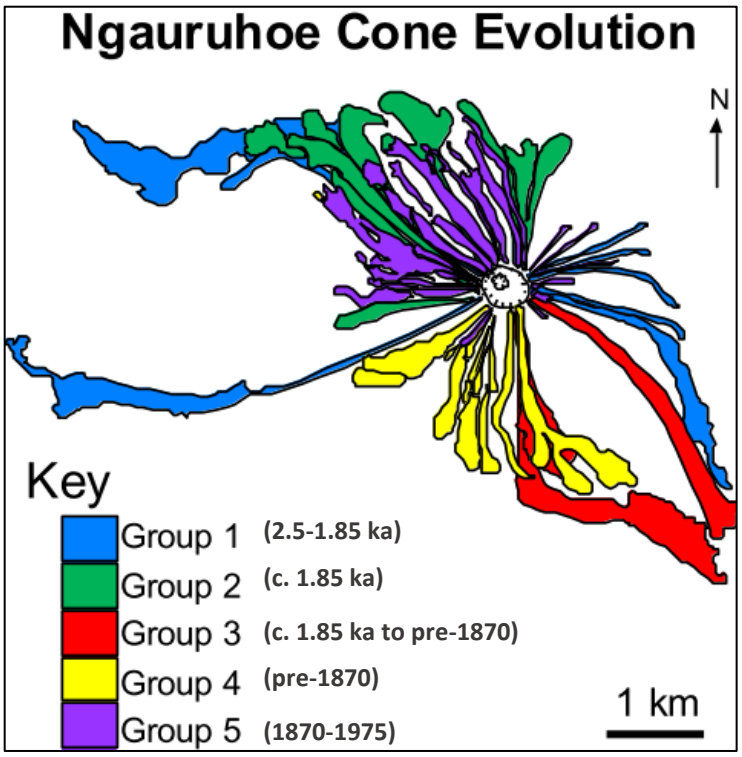

Figure 2.6 Sectoral cone growth of Ngauruhoe involving 5 key groups of lava which vary in flow chronology and composition (with permission from Krippner, 2009, originally adapted from Hobden *et al.,* 2002).

The five groups are each comprised of multiple lava flows, and correspond to five significant time intervals in Ngauruhoe's history (with group 1 being the oldest flows to group 5 being the youngest) (Hobden *et al.*, 2002). Group 1 includes nine recognisable lava flows which were emplaced on the northwest and eastern flanks of Ngauruhoe between 2.5-1.85 ka (all underlying the 1.85 ka Taupo pyroclastic deposit). One of these flows on the western slope remains the longest lava flow on Ngauruhoe with a length of 5.2 km. Group 2 is comprised of 14 flows on the northwest sector of the cone with some flows overlapping the earlier group 1 lavas. A few of these lavas predate the 232 AD Taupo deposit, but most of them overly it. The three flows which make up Group 3 represent a shift in cone growth to the southeast flanks of Ngauruhoe. These flows post-date and overly the Taupo deposit, and two of the three flows extend c. 3.4 km onto the Waihohonu Valley floor. The southern sector of the cone was progressively built up by the 13 lava flows of Group 4, some of which overly the group 3 lavas. Between 1870 and 1975, most of the 20 Group 5 lava flows were emplaced on the northwestern quadrant

of the cone, with several smaller flows also erupted onto the upper eastern slopes of the cone (Figure 2.6) (Hobden *et al.*, 2002).

2.7.2 Lava Flows and Implications on Underlying Magma System

Hobden (1997) explains that there is not a straightforward relationship between composition and timing of the five groups of lava flows (based on whole-rock analysis). There are some cases when two different compositional groups have been identified within a group or a particular time period (Hobden, 1997). The fact that the five groups display rapid and non-systematic changes in magma chemistry and radiogenic isotopes provides insight into the character of the magmatic system operating beneath the volcano (Hobden *et al.*, 2002). It is likely that multiple subsurface magma reservoirs feed into Ngauruhoe at any one time (Hobden, 1997; Price *et al.*, 2005), and that the volcano is characterised by a complex and open system (Hobden *et al.*, 2002; Price *et al.*, 2010). Within this complex system there has been mixing of several small and short-lived magma batches in addition to mixing with other crustal contaminants (Hobden *et al.*, 1999). Findings by Rowlands *et al.* (2005) which suggest why there is a low-velocity volume beneath Ngauruhoe are consistent with this explanation. A recent study conducted by Arpa *et al.* (2017) also agrees with the relatively shallow magma reservoir depths below Ngauruhoe.

The proposed magmatic structure beneath Ngauruhoe and its long term behaviour has been improved by a recent investigation of crystal histories by Coote and Shane (2016). Textural features and geochemical zonation of plagioclase phenocrysts from pre-historic and historic lava flows, indicate a magmatic system that is vertically extensive and involves various multi-level storage locations and durations (Figure 2.7). Despite the complex magmatic system, Coote and Shane (2016) argue that, scoria erupted over the past 7,000 years are petrographically similar due to a steady-state balance of intrusion and crystallization in the deep crust. There is also evidence for magma recycling, remobilization, and entrainment of co-magmatic crystals in ascending magmas, and higher levels of crustal assimilation at shallower levels.

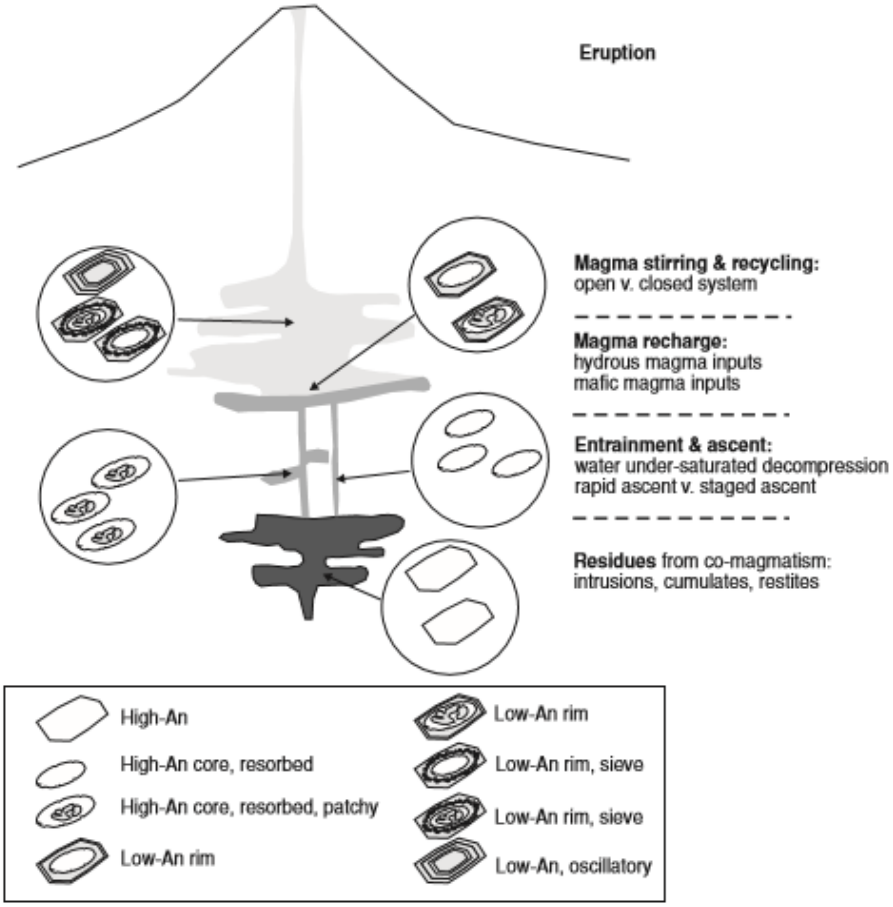

Figure 2.7 Conceptual model (not to scale) of the complex multi-level magmatic system underlying Ngauruhoe, including the spatial relationships, textures, and origins of crystals (Coote & Shane, 2016).

Understanding the underlying magmatic system of Ngauruhoe is important in the assessment of volcanic hazards and identifying likely precursor signals to future eruptions (Coote & Shane, 2016).

2.7.3 Ngauruhoe Petrography

Eruption deposits from Ngauruhoe are typically calc-alkaline, medium-K, basaltic andesite to andesite (Graham & Hackett, 1987; Hobden, 1997). These tend to be porphyritic-glomeroporphyritic in texture, with a typical phenocryst assemblage including highly abundant plagioclase followed by two less abundant pyroxenes (orthopyroxene ≥ clinopyroxene) (Hobden, 1997; Hobden *et al.*, 2002). About 40% of Ngauruhoe lavas are olivine-bearing, while others have little or no olivine (Steiner, 1958; Hobden, 1997). A small amount of iron-titanium (Fe-Ti) oxide phenocrysts such as magnetite and ilmenite are also present in some, but not all, deposits (Cole, 1978; Hobden, 1997). Ngauruhoe lavas are generally hypocrystalline (rich in glass), with phenocrysts typically set within a hyalopilitic or microlite-rich glassy groundmass (Cole & Nairn, 1975; Hobden, 1997).

Hobden (1997) studied the petrography and mineralogy of many Tongariro lavas, including those from Ngauruhoe. Many of these lavas exhibit disequilibrium mineral assemblages, with minerals commonly displaying sieve textures and strong reverse and patchy zoning. These petrographic properties indicate that magma mixing was involved during the petrogenesis of many lavas (Hobden, 1997). The petrography, presence of xenoliths (including metaquartzites and buchitic metagreywackes derived from Mesozoic Torlesse metasedimentary basement), and geochemical and isotopic compositions of many andesitic rocks from Ngauruhoe also provide evidence for crustal assimilation/contamination, fractional crystallization, and source heterogeneity (Briggs, 1981; Graham & Hackett, 1987; Graham *et al.*, 1988; Rogan & Blake, 1994; Hobden *et al.*, 1999; Price *et al.*, 2010).

2.7.4 Recent Work on Ngauruhoe

Barton (2011) studied the historic lava flows on Ngauruhoe to gain insight into the magma system and pre-eruptive processes. Petrographic analyses and mineral/glass chemistry data were used to study magma evolution over a series of eruptions (mainly 1870-1975, with a majority of samples from the 1954 lavas). Barton (2011) collected one sample of 1975 juvenile material from the block and ash flow deposit on the lower slopes and did not sample any of the crater rim deposit. Dense clasts associated with the 1975 eruption were not analysed in Barton's thesis, and there does not appear to be any record of microprobe analyses for groundmass glass in the 1975 juvenile sample.

Krippner (2009) divided the overall inner crater of Ngauruhoe into seven stratigraphic units, and presented analyses of componentry, petrography, and geochemistry (with a main focus on the 1954-55 material). Pittari *et al.* (2010) has since revised the stratigraphy of Krippner (2009). Morphological, petrographic and geochemical data have also been collected by Sanders (2010) for the 1954 Ngauruhoe lavas. This data was subsequently entered into existing numerical models to allow quantification of rheological properties and flow dynamics (Sanders, 2010).

The past eruptions of Ngauruhoe have been well-documented by various people (refer to section 1.1.3 for a summary); however, many papers lack detailed observations and analyses of the 1975 eruption deposits. Therefore, this research will focus specifically on the pre-eruptive conditions and processes that led to the eruption and emplacement of the 1975 crater rim deposit (refer to the research questions presented in Chapter 1, based on gaps in the literature).

Chapter Three

Proximal 1975 Crater-Rim Deposit Stratigraphy and Distal 1968-1975 Ash

3.1 Morphology of the 1975 Eruption Deposit

The 1975 fall deposit was emplaced during the most recent significant eruption from Ngauruhoe and is therefore the uppermost stratigraphic unit. The proximal-to-vent deposit has partially and irregularly draped down the outer volcanic slopes giving rise to an 'icing on the cake' appearance around the summit (Figure 3.1). The 1975 deposit also drapes down over the inner walls on the northern, southern and western sides of the inner crater, covering some of the lower stratigraphic units from previous eruptions (Figure 3.2). Around the northern and northeastern rim of the inner cone the deposit forms a vertical bluff approximately 9 m thick (Figure 3.3), and which varies both vertically and laterally in terms of thickness and stratigraphic characteristics. Fieldwork was predominantly focused on the northeastern side of the crater rim deposit due to accessibility constraints and the need to obtain information on vertical stratigraphic variations. This would not have been possible on the draping deposits or slump/collapse deposits (Figures 3.2, 3.3, and 3.4).

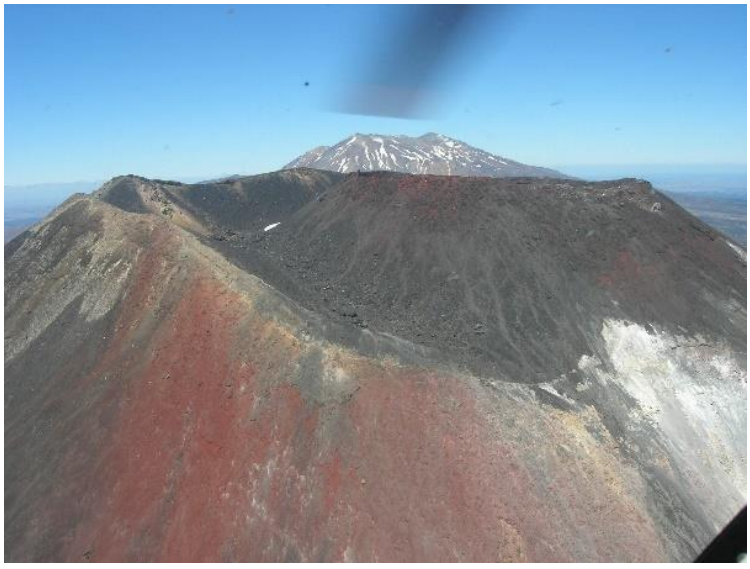

Figure 3.1 The 1975 strombolian fall deposit drapes partially down the outer crater rim of Ngauruhoe. Note the reddish pyroclastic material which was produced from this eruption (photo by Adrian Pittari, 2010).

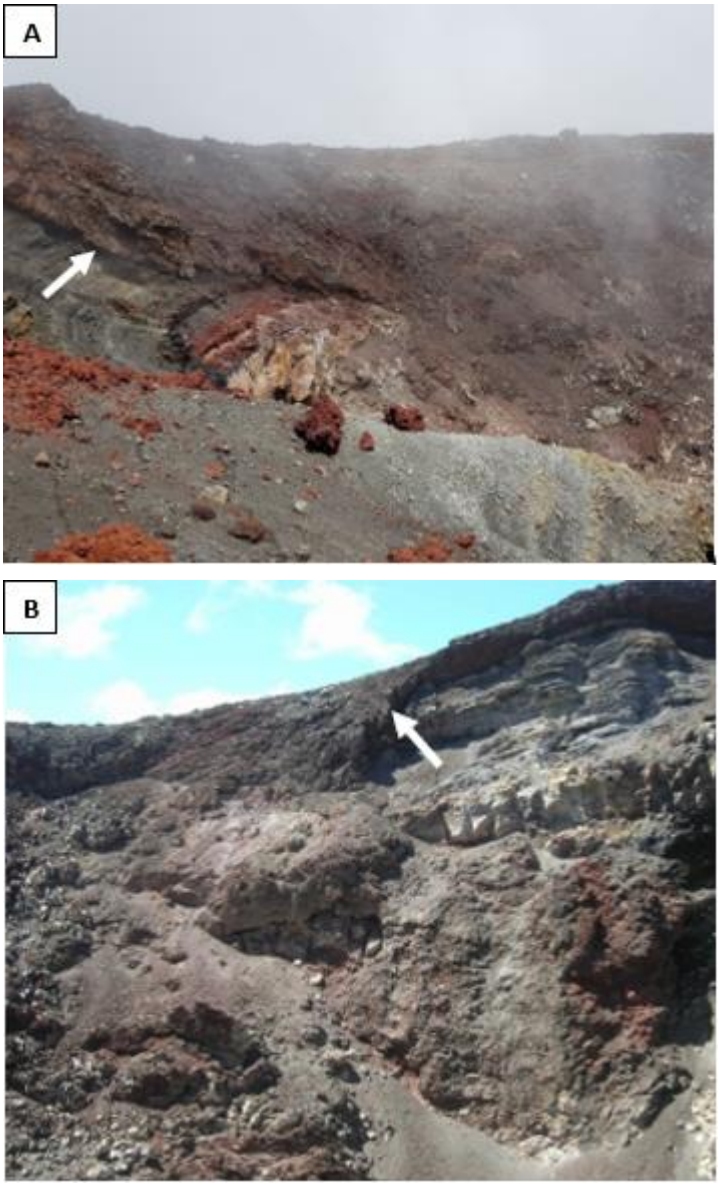

Figure 3.2 The 1975 reddish-black coloured deposit draping down the A) southeastern and B) northern side of the inner crater (depicted by white arrows). Note large slump blocks and loose material where sections of the inner crater rim deposit have collapsed and fallen into the crater (photos by Geoff Kilgour, 2018).

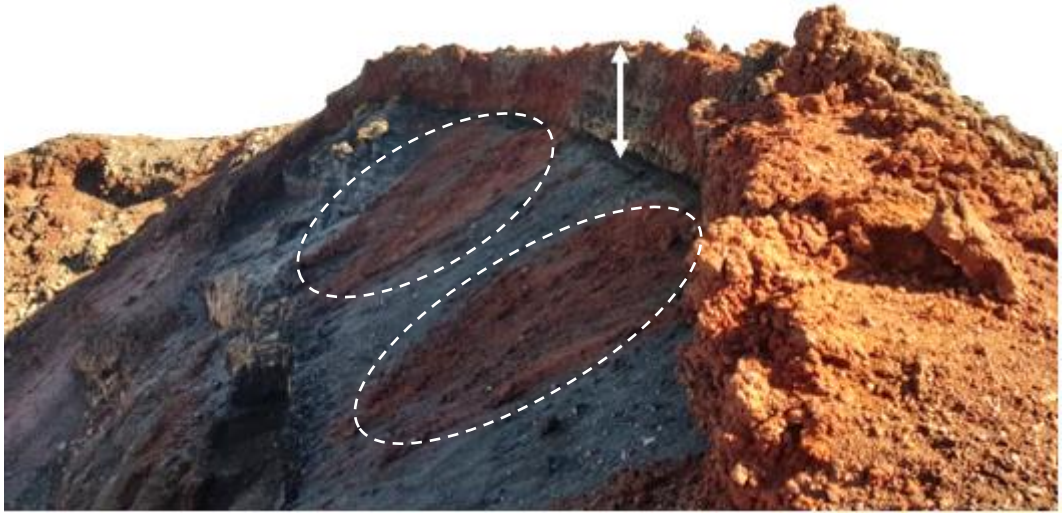

Figure 3.3 The 1975 eruption deposit forms a vertical bluff, on average ~9 m thick, on the northern side of the inner crater rim (depicted by white arrow). Sections of partial crater collapse from the 1975 deposit are also present as illustrated within the white dashed lines (photo by Geoff Kilgour, 2018).

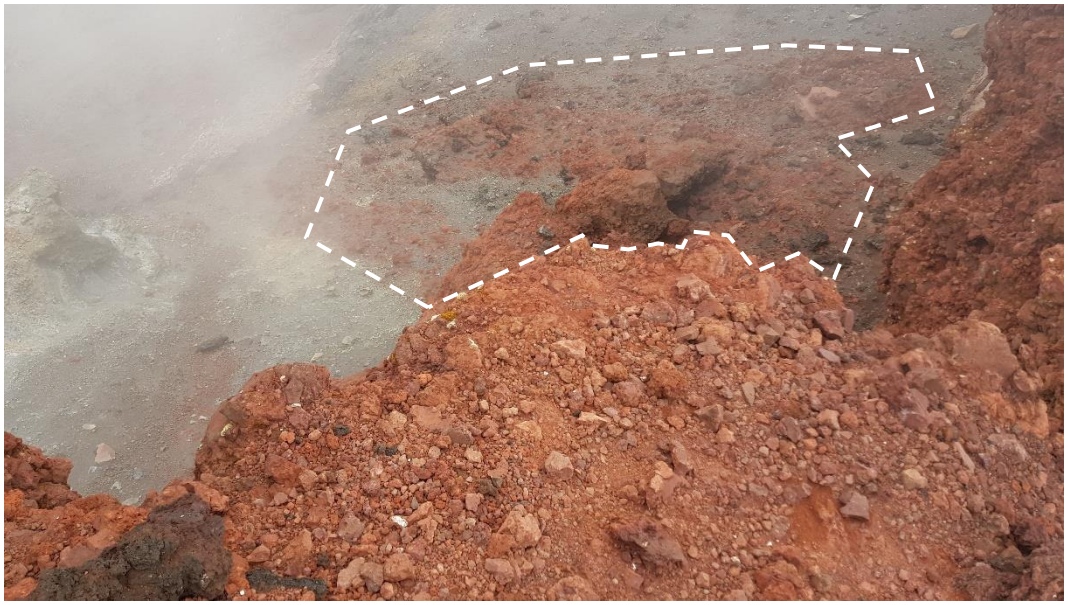

Figure 3.4 Looking down into the crater from the top of the inner crater rim. Partial collapse of the crater rim has resulted in large fragments of the 1975 deposit falling down onto lower stratigraphic units within the crater (white dashed line).

3.2 Brief Overview of Clast Types and Terminology

There are three main clast types that comprise the 1975 inner crater rim deposit (Figure 3.5): (1) moderately vesicular (scoriaceous) juvenile clasts, (2) dense, angular to sub-rounded, poorly vesicular basaltic-andesite clasts, and (3) weakly vesicular juvenile spatter clasts. Note that 'juvenile' refers to clasts which are derived from magma considered here to be involved in the 1975 eruption. Rare lithics (averaging ~30 mm) were also present in low quantities throughout the 1975 deposit, however these were not analysed in detail as part of this study.

The clast types described above occur in various sizes, and it is therefore important to understand the size terminology used in this study. Lapilli is the term used for pyroclasts which range from 2 to 64 mm in diameter, while clasts greater than 64 mm are termed blocks or bombs. Bombs are sub-rounded to rounded clasts (often erupted in a fluidal state), whereas blocks are usually ejected as solid fragments and therefore have more angular morphologies. Spatter is the term applied to fluidal bombs that are deformed and agglutinated (welded) upon landing.

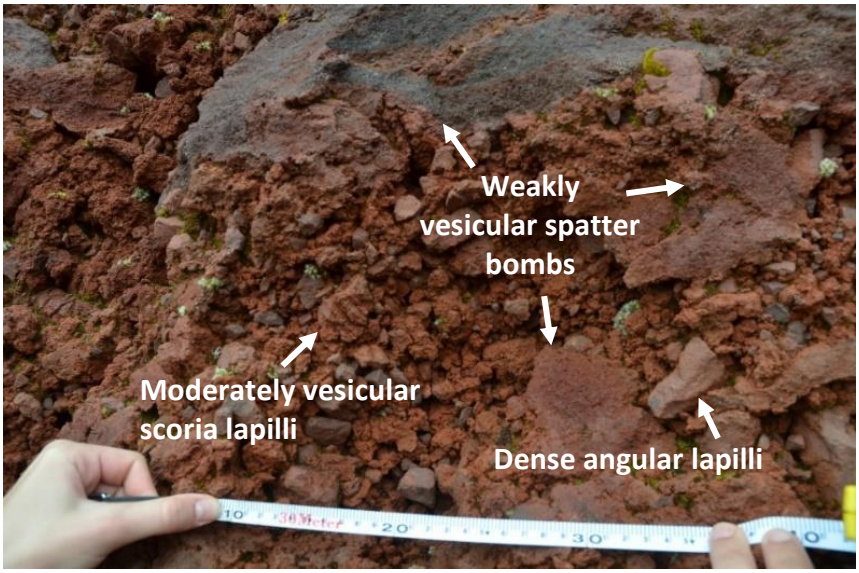

Figure 3.5 The range of clast types in the 1975 deposit including dense angular to sub-rounded clasts, moderately vesicular juvenile scoria clasts, and weakly vesicular juvenile spatter (photo by Geoff Kilgour, 2018).

3.3 Fieldwork Methodology

Stratigraphic variations were logged in the field and notes on the various types of clasts, clast sizes, and component proportions were recorded. Visual field estimates of the component proportions were made using a comparator, and a ruler was used to measure average clast sizes (as well as some of the larger clasts) in each facies. Around 20-30 representative individual clasts were collected at various heights throughout the crater rim deposit (Figures 3.6 and 3.7; Appendix 1). A digitalised stratigraphic log was subsequently produced using Inkscape software (Figure 3.7).

3.4 Stratigraphy of the 1975 Vertical Inner Crater Rim Deposit

An in situ stratigraphic succession produced from the 1975 eruption is exposed on the northern and northeastern sides of the inner crater rim. The deposit varies laterally in thickness but has an average height of approximately 9 m. It is clast-supported (consisting of lapilli to block/bomb-sized pyroclasts) and overlies alternating ash-lapilli beds which were emplaced sometime between 1955 and 1975 (Figure 3.6). The deposit has been divided into four facies, A to D (Figures 3.6 and 3.7). This division of facies is based on noticeable vertical variations in colour and other physical characteristics (including the proportion of different clast types, and changes in the proportion of discrete individual components and the degree

of coalescence). An overview of the inner crater outcrop is portrayed in a stratigraphic log in Figure 3.7, and each facies is described in detail in section 3.4.1.

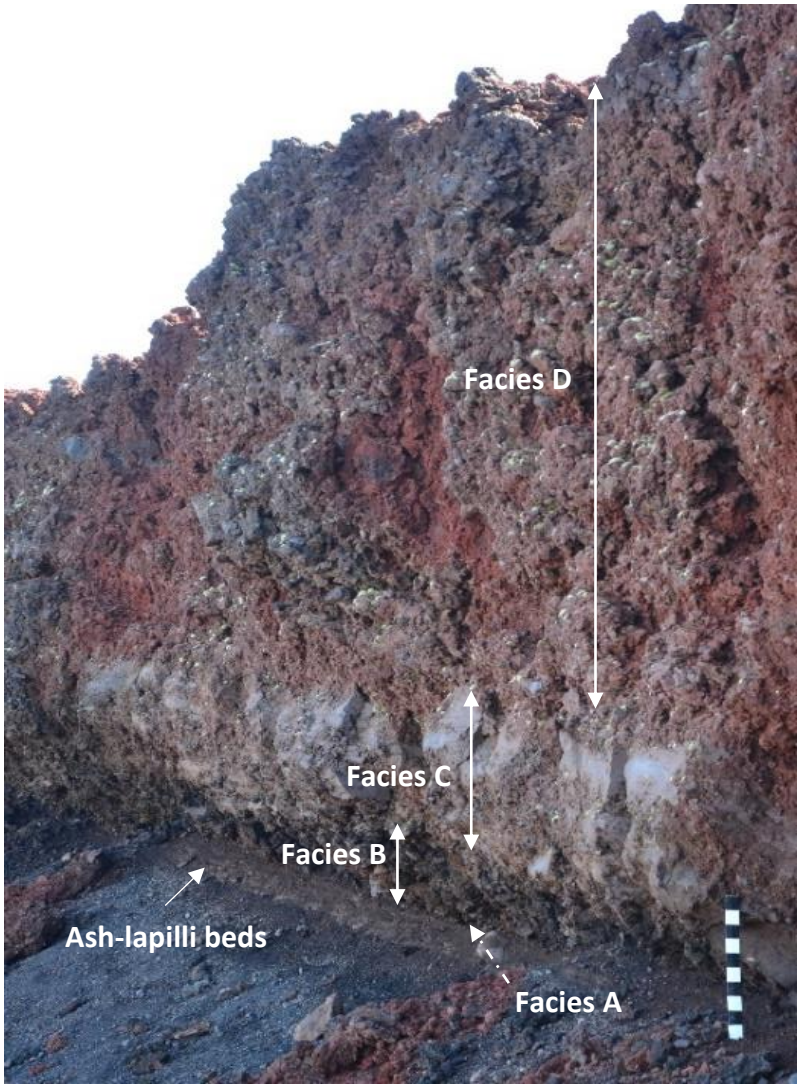

Figure 3.6 The crater rim deposit produced during the 1975 eruption of Ngauruhoe, including division of the deposit into four discernable facies (A, B, C, and D). Several ash-lapilli beds can also be seen underlying the 1975 deposit (photo by Geoff Kilgour, 2018).

3.4.1 Facies Descriptions

3.4.1.1 Facies A (dense sub-angular lapilli and scoria lapilli deposit)

Facies A lies directly above the underlying ash and lapilli layers (Figures 3.7 and 3.8), with an average thickness of only 12 cm (although there are some lateral variations). The facies is black, moderately to well sorted, and predominantly consists of fine, dense, sub-angular to angular lapilli (90-95%) with an average size of approximately 4 cm. Fine black scoria lapilli clasts of similar size appear to be in low abundance (5-10%) within facies A. There is a gradational contact into facies

B above, which has similarities to facies A in terms of colour and grainsize but differs in the relative proportion of dense versus vesicular clast types.

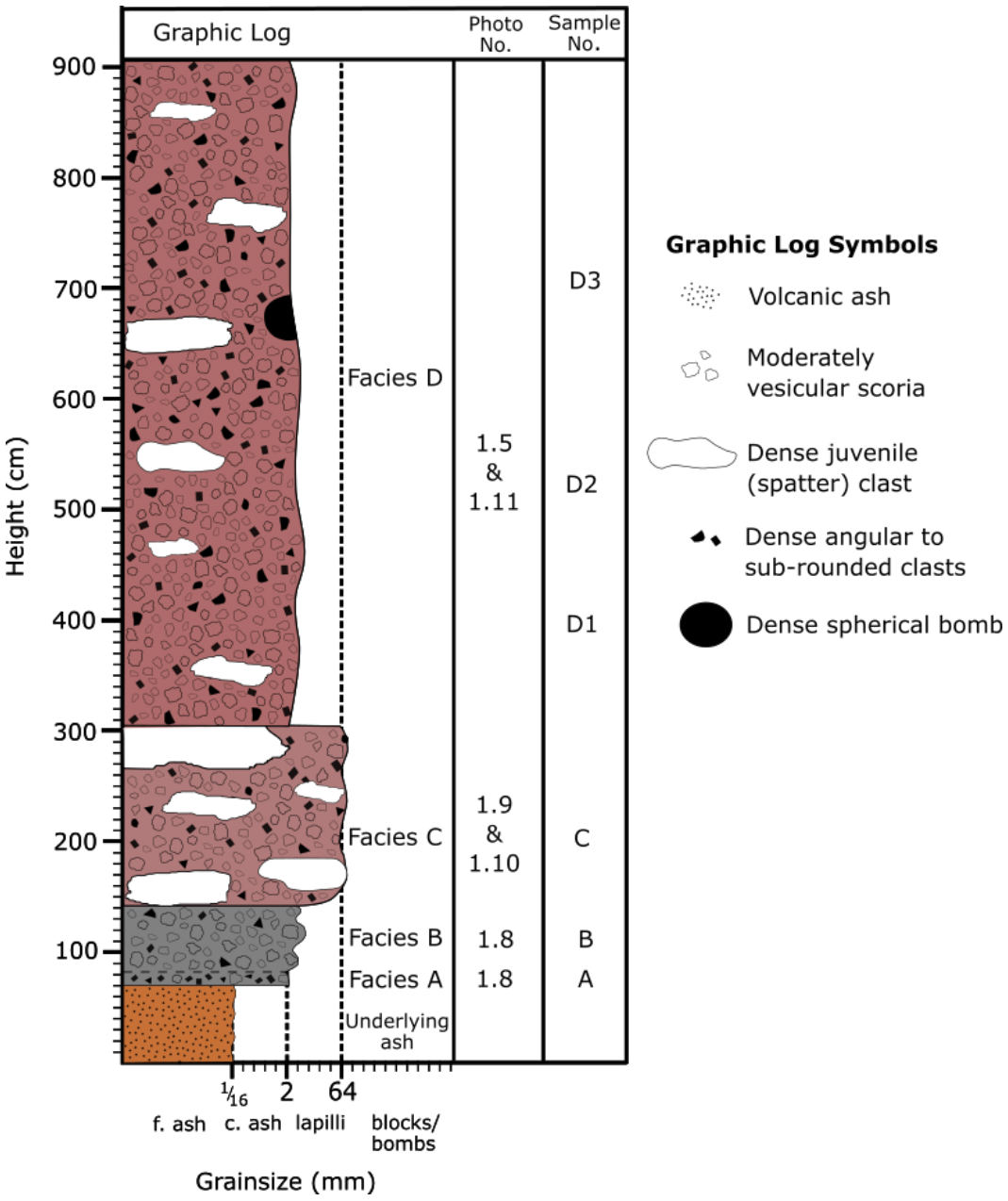

Figure 3.7 Stratigraphic log of the 1975 inner crater rim deposit depicting the various facies and vertical changes in colour and componentry (note that the differences in colour between facies C and D represent variations in the degree of welding). Refer to Figure 3.6 to see this outcrop and facies labelled in photograph.

3.4.1.2 Facies B (black scoria lapilli/bombs and dense lapilli deposit)

Facies B is a dark, less oxidised (compared to overlying facies), massive deposit with a thickness of approximately 50-60 cm (Figure 3.8). It is predominantly composed of orange-brown and brownish-black moderately vesicular scoria lapilli (~90%), and a smaller proportion of dense sub-angular to sub-rounded lapilli (~10%). There is a mixture of both fine (~8 mm) to coarse (~16-32 mm) lapilli, but

a higher proportion of coarse lapilli on average. The clasts are mostly isolated components (i.e. not coalesced or welded together).

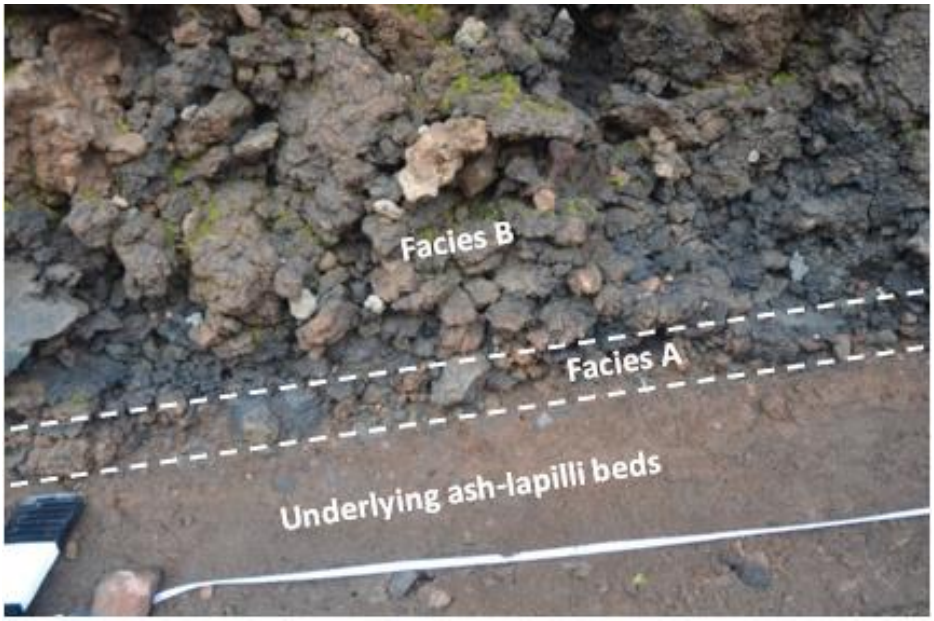

Figure 3.8 Facies A and B at the base of the 1975 crater rim deposit, overlying the ash-lapilli beds below. Note that the measuring tape in this photo represents 0.5 m (photo by Geoff Kilgour, 2018).

3.4.1.3 Facies C (loose scoria, dense lapilli, and large irregular domains of densely coalesced/agglutinated pyroclasts)

There is a relatively sharp contact between facies B and C, with rapid changes in both grain size and colour (although some contact boundary areas are more gradational than others) (Figures 3.6 and 3.7). Facies C is a reddish-brown/grey, oxidised unit that is laterally variable in thickness, ranging from approximately 1.1 to 1.6 m. This facies is poorly sorted (containing a mixture of coarse to very coarse lapilli and bombs) and includes a mixture of non- to weakly agglutinated clasts, as well as some dense, strongly agglutinated domains (Figure 3.9). Facies C also varies laterally in terms of the proportion of individual clasts and coalesced material, with some areas more coherent than others. Overall, facies C is comprised of approximately 50% dense coalesced material, approximately 35-40% moderately vesicular juvenile scoria lapilli, and approximately 10-15% coarse, sub-angular to sub-rounded, dense lapilli (Figure 3.9). Within some of the dense coalesced units, some flattened grey/black-coloured scoria was observed (Figure 3.10).

Figure 3.9 Facies C of the 1975 crater rim deposit, including moderately vesicular scoria lapilli, dense coarse lapilli, and densely agglutinated areas. Note 1-metre bar for scale (photo by Geoff Kilgour, 2018).

Figure 3.10 Flattened and deformed scoria (depicted by the white arrows) within the coalesced material in facies C of the 1975 crater rim deposit. Note hammer for scale (photo by Geoff Kilgour, 2018).

3.4.1.4 Facies D (dense lapilli to blocks, scoria lapilli, and bombs)

There is another sharp contact between facies C and D (Figures 3.6 and 3.7), with rapid changes in the proportion of different clasts (including the extent of welded material). This contact boundary also varies laterally and is more gradational in some areas than others. Facies D is on average ~6 m thick, and is a reddish-brown, massive, and poorly sorted (compared to facies A and B) deposit with high variability and complexity in terms of clasts. It contains a mixture of moderately vesicular juvenile scoria lapilli, dense angular to sub-rounded lapilli and blocks, dense spherical bombs, and coalesced spatter (Figures 3.5 and 3.11). Different

areas within facies D typically comprise discontinuous clast sizes (with any one area potentially having a range of fine lapilli to blocks and bombs).

Facies D contains a high proportion of moderately vesicular scoria lapilli (~60%), and a smaller proportion of dense lapilli (~20%). Spatter bombs are also abundant throughout facies D (~20%), with some larger spatter components measuring up to 50 cm in size. There are also some large dense spherical bombs that have a characteristically different morphology to the spatter bombs; the dense spherical bombs have significantly smoother exteriors and are also non-vesicular (Figure 3.11). They are similar in colour and texture to the angular to sub-rounded dense lapilli, hence are not considered juvenile. The roundness of these clasts is attributed to physical abrasion, which indicates they have probably been recycled through more than one eruption phase or spent a relatively long time being milled in the erupting vent.

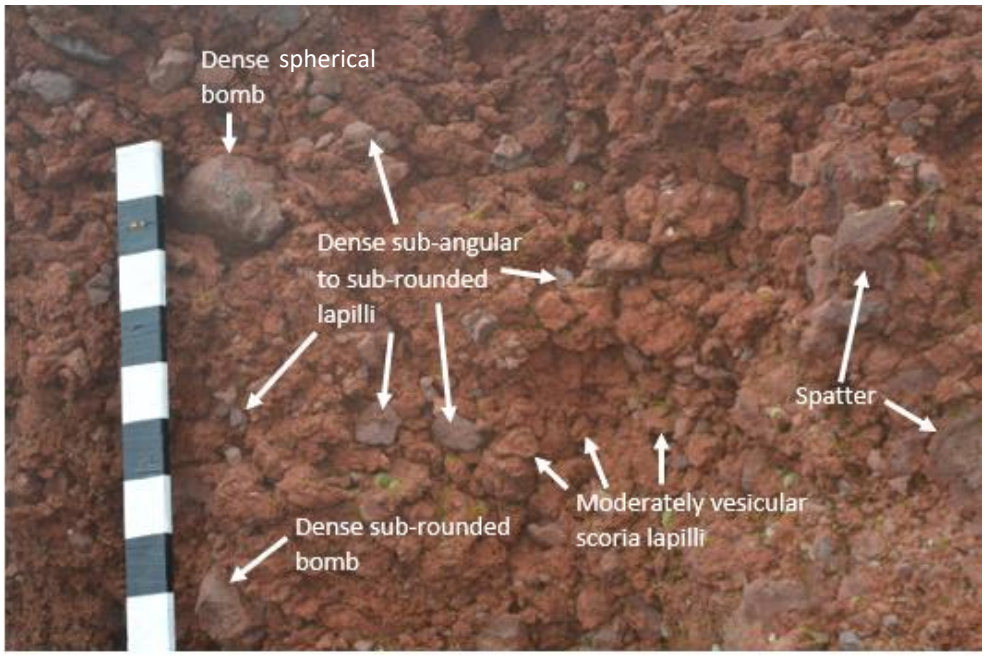

Figure 3.11 Complexity of clasts within facies D including spatter, moderately vesicular scoria, and dense lapilli and bombs. Note 90 cm of ruler shown in photograph for scale (photo by Geoff Kilgour, 2018).

Rare basement-derived lithic clasts were also present throughout facies D, constituting <5% of the entire deposit. The lithics are predominantly quartz-rich or quartzofeldspathic and are typically <3 cm in size (Figure 3.12). They are most likely derived from the Mesozoic Torlesse terrane (metamorphosed argillite greywacke basement and resulting quartz veins) that partly underlies the Taupo Volcanic Zone (Steiner, 1958; Graham *et al.*, 1988; Hobden, 1997). Xenoliths were

also observed within some dense and scoria clasts and smaller xenoliths were commonly observed in thin sections. These results are presented further in Chapter 4 (Figure 4.2 C; Figure 4.26).

Figure 3.12 Lithic (approximately 20 mm in size) from facies D of the 1975 inner crater rim deposit.

3.4.2 Quantitative Clast Type Analysis

3.4.2.1 Methodology

Point counting of the 1975 outcrop was undertaken to quantitatively analyse the componentry of this deposit. As facies B is lower down in the deposit and easily within reach, point counting of this facies was carried out in the field by measuring out an area of 1 m^2 (Figure 3.13). The type of clast at the top left corner was recorded, and this was repeated every 6.7 cm across and every 6.7 cm down. Three clast type categories were used for the purpose of point counting: dense clasts, moderately vesicular scoria, or poorly vesicular spatter (bombs produced from the agglutination of scoria clasts upon landing). Even though scoria and spatter are most likely juvenile and derived from the same origin, they were recorded separately in the initial point counting.

Due to the height of facies C and D (and poor visibility during field visits to the crater in this study), high resolution archive photographs by Pittari (2010, unpublished) were used. Pittari used a tape measure and four pieces of paper to mark out the corners of a 1 x 1 m square in both facies. A 15 x 15 cm grid was drawn over the photographs in Inkscape (Figures 3.14 and 3.15); at every grid

junction, the type of clast was recorded. Close-up photos were used to assist with determining the clast type that was present at each grid junction.

Figure 3.13 White string outlining an area of 1 m^2 in facies B (i.e. 2.0 m by 0.5 m). Note the small white piece of string (representing 6.7 cm) in the top left quadrant which was used for point counting in the field.

3.4.2.2 Quantitative componentry results

Point counting indicates noticeable differences in the proportion of components within each facies. The full point count data can be found in Appendix 2 and are summarised below (Table 3.1). Facies B is mostly comprised of moderately vesicular scoria lapilli (83%), but also has a small proportion of dense sub-angular to sub-rounded lapilli (12%). There is a minimal amount of spatter/coalesced material in facies B compared to facies C and D, with only 6% identified from the point counting exercise. In contrast, facies C is largely composed of spatter/dense coalesced juvenile material (51%), and also contains approximately 34% moderately vesicular scoria, and 15% dense sub-angular to sub-rounded lapilli. Facies D has a smaller proportion of coalesced material than facies C, but still has more spatter than facies B at approximately 13%. It is also comprised of approximately 63% scoria and 24% dense clasts. These results are all consistent with the visual estimates made with a comparator during field observations (refer to section 3.4.1).

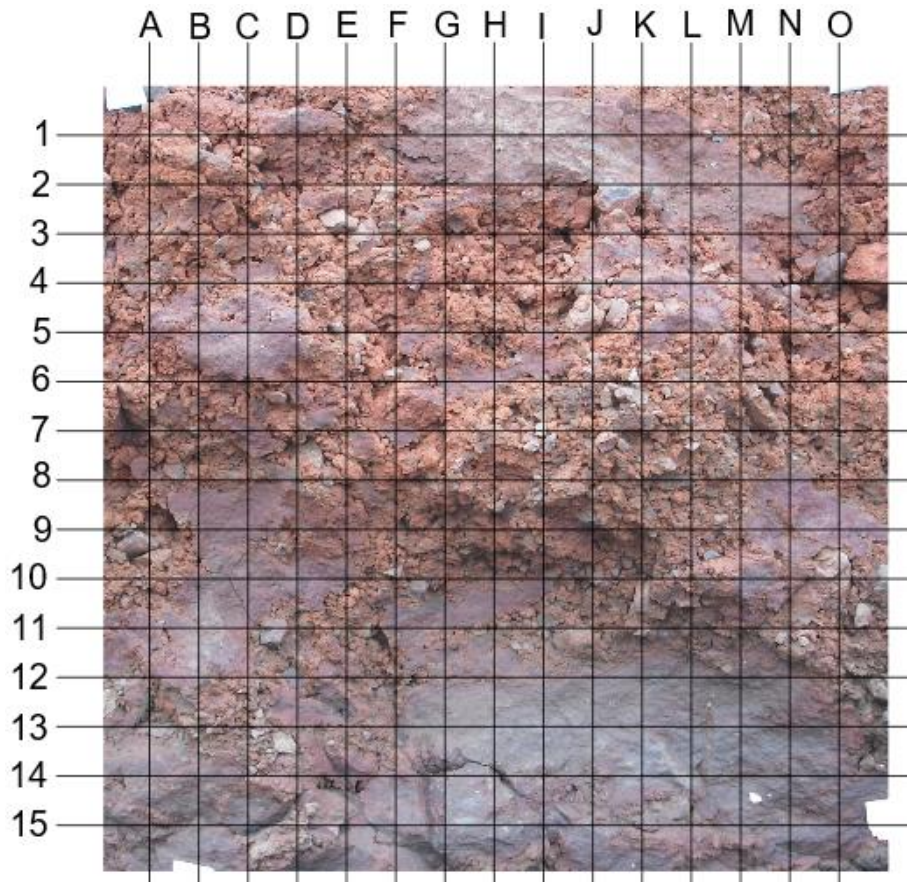

Figure 3.14 Photograph of facies C, overlain by a 15 x 15-line grid for point counting purposes (photo by Adrian Pittari, 2010 unpublished).

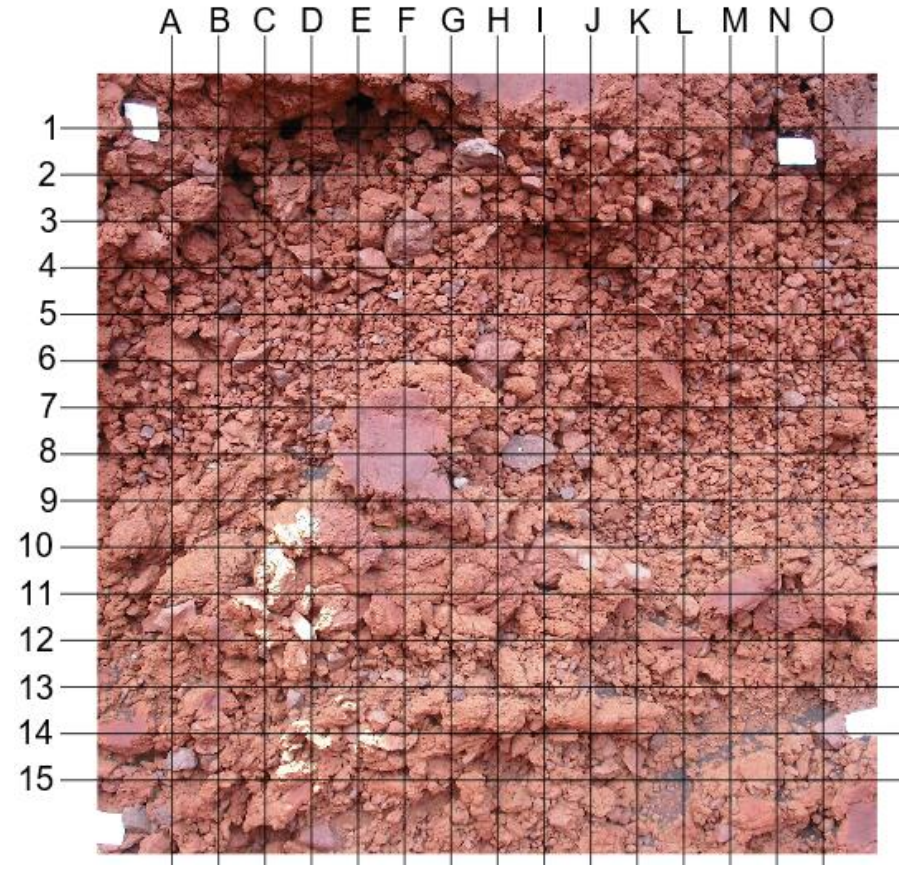

Figure 3.15 Photograph of facies D, overlain by a 15 x 15-line grid for point counting purposes (photo by Adrian Pittari, 2010 unpublished).

Table 3.1 Summary table of component percentages within each facies, as obtained from point counting. Note that point counting data was not obtained for facies A.

Facies	Scoria clasts	Dense clasts	Spatter
B	83%	12%	6%
C	34%	15%	51%
D	63%	24%	13%

3.5 1968-1975 Ash Samples

3.5.1 Methodology

Sub-samples of ash were collected from earlier Ngauruhoe eruption during 1968-1975 that were stored on archive at GNS Science (Wairakei). Observations and notes were recorded for the colour and visual grain size of the ash samples. Quantitative grain size data was obtained using the Malvern Mastersizer 3000 laser diffraction particle size analyser at the University of Waikato; with refractive index set at 1.5, absorption index set at 0.2, stirrer speed at 2300 revolutions per minute (RPM), and no ultrasound.

3.5.2 Characterisation of Ash Samples

Table 3.2 characterises the colour, grainsize class, and median grainsize of each of the 1968-1975 ash samples. The quantitative median grain size data complements the visual grain size descriptions and was particularly useful in determining which samples were suitable for sieving (refer to section 4.5.1.1). No further work was carried out with grain size data since it is also a function of distance from source which is variable and not identified for every sample.

Table 3.2 Characterisation of the 1968-1975 ash sub-samples; including sample number, collection date, visual descriptions of colour and grainsize, and median grain size data. Samples highlighted in orange are used for further shape, size and componentry analyses (see section 4.5). Refer to Appendix 1 for a summary of analyses carried out on each sample, and Appendix 3 for laser sizer analyses.

Sample no.	Collection date	Colour	Visual grainsize description	Median grainsize (µm)
P16948	1954	Very pale grey	Fine ash	9.79
P14589	1-Jan-54	Very pale grey	Fine ash	14.3
18-Aug-68	18-Aug-68	Light to medium brownish grey	Fine ash	32.6
Ng1	March, 1972	Pale brown	Fine ash	50.8
39298 (N112/B)	24-Mar-72	Light to medium brown	Fine ash, few ash clumps	34.3[1]
Ng2 39297 (N112/A)	24-Mar-72	Light to medium brown	Coarse ash	86.8
Ng3	1-Apr-72	Medium greyish brown	Coarse ash	-- [3]
Ng4	8-May-72	Light brown grey	Fine ash	37.2
Ng6	5/6-Jan-73	Light to medium greyish brown	Fine ash	43
Ng7	31-Jan-73 (15/1/73 eruption)	Light greyish brown	Fine ash, few dense lapilli	49.4
Ng8A	10-9-73 (8/9/73 eruption)	Light to medium brown	Fine ash, few ash clumps	41.6[1]
Ng8B	13-9-73 (8/9/73 eruption)	Light to medium greyish brown	Fine ash	37.9
Ng9	30-9-73 (29/9/73 eruption)	Light brownish grey	Fine ash	43.5
Ng10	17-Oct-73	Light brownish grey	Fine ash	44.6
Ng11	17-Oct-73	Medium to dark brownish black	Coarse ash	95.9[2]
Ng12A	26-Oct-73	Medium brown to grey	Coarse ash	89.6
Ng12B	26-Oct-73	Light brownish grey	Coarse ash, few dense lapilli	133
Ng13A	26-Oct-73	Light brown	Fine ash	39.6
Ng13B	26-Oct-73	Light greyish brown	Fine/coarse ash	48.8
Ng14	7-10 -Dec-73	Medium grey Some fine plant material	Coarse ash	73.2
Ng15	7-Dec-73	Light to medium brownish grey	Coarse ash	73.2
Ng16	16-Dec-73	Medium grey	Coarse ash	81.6
Ng17	16-Dec-73	Medium to dark grey to brown	Coarse ash	101
Ng18	22-Jan-74	Light greyish brown	Coarse ash	62.5
Ng20	24-Jan-74	Light to medium grey/brown	Coarse ash, few dense lapilli	113
Ng21	24-Jan-74	Medium grey	Coarse ash, few dense lapilli	116
Ng22	24-Jan-74	Medium brownish grey	Coarse ash	107
Ng23	26-Jan-74	Dark grey	Coarse ash	104[2]
Ng25	29-Jan-74	Light to medium grey	Coarse ash	132

Table 3.2 (continued)

Sample no.	Collection date	Colour	Visual grainsize description	Median grainsize (µm)
Ng26	30-Jan-74	Brownish-black Lots of plant material	Coarse ash	103
Ng27 (P39850)	Date=1974	Light grey	Fine ash	22.9
Ng29	28-Mar-74	Medium to dark greyish brown	Coarse ash	57.3
Ng30	28-Mar-74	Dark grey/black	Coarse ash	97.6[2]
Ng31	28-Mar-74	Dark grey to black	Coarse ash	--[3] (c.f.to sample Ng30)
Ng32	28-Mar-74	Light grey/brown	Coarse ash	118
Ng34	28-Mar-74	Light grey	Coarse ash	83.9
Ng35	No date, possibly 74	Medium brownish grey	Coarse ash	160
Ng40B (P39866)	31-Mar-74	Pale to light grey	Fine ash	17.3
Ng41	No other info	Dark grey to black	Coarse ash	--[3]
Ng42	11-12 Feb 1975	Grey	Coarse ash	86.4[2]
Ng43	17-Feb-75	Medium grey	Coarse ash	110
Ng44	17-Feb-75	Medium grey	Coarse ash	94.5
Ng45	19-Feb-75	Brown/grey/black	Coarse ash	610
Ng46 (40673)	19-Feb-75	Pale grey	Fine ash	8.35
Ng46	19-Feb-75	Brownish-black	Lapilli	--
Ng47	19-Feb-75	Dark brownish black	Coarse ash	71.3
Ng48	19-Feb-75	Brownish black	Coarse ash	88.6[2]

[1]Mixed with water to break down clumps.
[2]Measured but low amount of sample.
[3]Not enough sample.

3.6 Summary of Key Findings

The key findings from this chapter are outlined below.

- The 1975 inner crater rim deposit has been divided into four facies, A, B, C, and D, based on vertical variations in colour, proportions of different clast types, and the degree of coalescence. Note that the component percentages summarised in the following descriptions are based on point count data.

- Facies A is black, moderately to well sorted, and predominantly consists of fine, dense, sub-angular to angular lapilli (plus a minor proportion of fine black scoria lapilli). Point count data was not obtained for this facies, however, field observations provide estimates of 90-95% and 5-10% for dense and scoria lapilli, respectively.

- Facies B is a massive deposit, predominantly composed of orange-brown and brownish-black moderately vesicular scoria lapilli (~83%), and a smaller proportion of dense sub-angular to sub-rounded lapilli (~12%). There is a mixture of both fine to coarse lapilli, but a higher proportion of coarse lapilli. The clasts are mostly isolated, with only 6% spatter identified from point counting.

- Facies C is a reddish-brown/grey, oxidised unit that is poorly sorted (containing a mixture of coarse to very coarse lapilli and bombs). It includes non- to weakly agglutinated clasts (~34% moderately vesicular scoria, and 15% dense sub-angular to sub-rounded lapilli) as well as some dense, strongly agglutinated domains (51%). Flattened and deformed grey/black scoria was observed within some of the dense coalesced units.

- Facies D is a reddish-brown, massive deposit containing a mixture of ~63% moderately vesicular juvenile scoria lapilli, ~24% dense clasts (including both angular to sub-rounded lapilli and blocks, and dense spherical bombs), and ~13% spatter.

- Ash samples from 1968 to 1975 have been characterised based on colour and grainsize. Samples range from fine to coarse ash (with median grainsizes ranging from 8.35-160 μm).

Chapter Four

Morphology, Petrography, and Vesicle Texture of Lapilli and Ash

4.1 Introduction

This chapter describes the morphology, componentry, and texture of clasts collected from the 1975 inner crater rim deposit, as well as ash samples produced from several eruptions between (and including) 1972-1975. Morphological descriptions of scoria and dense clasts from the 1975 eruption are based on hand sample observations, while clast componentry, groundmass, and vesicle texture descriptions are provided from petrographic studies and scanning electron microscopy. Further quantitative bulk vesicularity data is provided for the 1975 clasts, in addition to pycnometer vesicularity of clasts produced from both the 1954 and 1975 eruptions (allowing for comparison between these eruptions and associated magmatic conditions). Qualitative componentry analyses from stereomicroscopic observations are also provided for the ash samples, in addition to morphological analyses of the glassy grains via SEM imagery and the use of ImageJ shape analysis software.

4.2 1975 Clast Morphology and Physical Appearance

4.2.1 Clast Descriptions

The samples collected from the 1975 inner crater rim deposit can be broadly separated into two distinct groups; moderately vesicular scoria clasts and dense clasts. The scoria clasts come in a large range of morphologies from low to high sphericity and typically quite irregular in shape with rough exteriors (Figure 4.1). Some scoria (particularity from Facies C and D) also vary in vesicularity, ranging from regions of moderate vesicularity to denser regions within the same clast (Figure 4.1 C). Another noticeable difference is the brownish-black colour of scoria clasts in Facies A and B, compared to the earthy reddish-brown colour of clasts in Facies C and D (Figure 4.1).

Figure 4.1 Moderately vesicular juvenile scoria clasts from A) Facies A, B) Facies B, C) Facies C, and D) Facies D (representative of all sampling localities within Facies D).

In contrast, the dense clasts are mostly sub-rounded to sub-angular (although a few clasts exhibit more angular morphologies). They are generally more regular in shape and have smoother exteriors (Figure 4.2) compared to the scoria clasts. The occasional breadcrust texture was also observed (Figure 4.2 E). Dense clasts come in a range of colours (Figure 4.2); those in Facies C and D appear to be quite similar in colour (mostly reddish-brown), while the dense clasts in Facies A and B are more variable (including pinkish-grey, grey, dark grey, mottled orange-black, and black coloured clasts). Some dense clasts and scoria also contain white and/or clear xenolith inclusions as depicted in Figure 4.2 C, which are quartz-rich or quartzofeldspathic in composition.

Figure 4.2 Dense (poorly vesicular) angular to sub-rounded clasts from A) Facies A, B) Facies B, C) Facies C, D) 80 cm from the base of Facies D, E) 2.2 m from the base of Facies D, and F) 2 m from the top of Facies D.

4.3 Petrography and Mineralogy of 1975 Clast Types

Petrographic analyses were carried out on 22 basaltic-andesite samples collected from the various facies within the 1975 inner crater rim deposit, including a variety of both moderately vesicular scoria and dense clasts. The clasts are all aphanitic, hypocrystalline, and porphyritic in texture, with phenocrysts sometimes clustered as glomerocrysts. The mineralogy includes plagioclase, orthopyroxene, clinopyroxene, olivine, and Fe-Ti oxides (predominantly magnetite). Phenocrysts are typically set in a hyalopilitic groundmass consisting of microlites/crystallites randomly orientated within glass (however groundmass textures vary, particularly between clast types and amongst dense clasts). Differences and similarities in phenocryst assemblages and textures in the 1975 clasts, in addition to vesicle

textures and quantitative vesicularity studies, provide insight into pre-eruption magmatic conditions and processes. In contrast, groundmass textures generally provide insight into magma ascent and degassing along with subordinate cooling.

4.3.1 Methodology

4.3.1.1 Thin section preparation

Representative samples of each clast type (dense and vesicular clasts) were selected from each of the stratigraphic facies identified in the 1975 inner crater deposit (Figure 3.7). Thin sections were made for each of the 22 representative clasts using standard petrographic techniques. Each sample was first cut into blocks approximately 4 cm by 2 cm in size. The softer scoria clasts were then impregnated with resin, and once dry, the most suitable face on each block was ground flat using #600 polish powder on a glass plate. Hillquist thin section resin and hardener was used at a ratio of 2.3:1 to mount the prepared surface of each clast onto the frosted side of a petrographic glass slide. Once dry, the mounted blocks were cut to a thickness of ~1 mm, then ground down on the Struers Discoplan-TS to ~30 µm (to the point where feldspars were mostly greyish but still had a very slight yellow tinge under the petrographic microscope). Thin sections were subsequently ground down further on grinding plates using grit-500 followed by grit-1200 silicon carbide grinding paper, polished, and left uncovered for later microprobe analysis.

4.3.1.2 Petrographic analysis

Textural characteristics and mineral components were documented in the thin sections using the petrographic microscope under transmitted light. Standard point counting was undertaken to obtain quantitative data on vesicle, groundmass and phenocryst abundances (refer to Appendix 4 for original point count data). Although vesicles were included in the original point counting, the data was subsequently normalised for zero vesicles. Component percentages stated in the text are normalised for zero vesicles (i.e. vesicle-free whole rock), with the exception of vesicle percentages which are original values. A stage interval and line spacing of 750 µm was used, and the number of counts achieved for each thin

section varied depending on the area of sample available (generally ranging from between 166 to 547 counts per sample).

The type of point counting information obtained for each sample was dependent on the overall rock texture; for porphyritic rocks with a glassy groundmass, point counting categories included plagioclase phenocrysts, plagioclase microphenocrysts, clinopyroxene phenocrysts, orthopyroxene phenocrysts, pyroxene microphenocrysts, olivine (any size), opaque minerals, groundmass, vesicles, and lithics. Microphenocrysts were classified as those crystals 125 µm or smaller in size, but still larger than crystallites and microlites in the glassy groundmass. For rocks with intergranular groundmass textures, the microphenocrysts essentially made up the groundmass and therefore any microphenocrysts were counted as groundmass.

4.3.1.3 Scanning electron microscope (SEM) analysis

Most SEM work was carried out using the Hitachi S-4700 cold field emission SEM at the University of Waikato. The Nikon JCM-6000 NeoScope bench-top SEM at GNS Science Wairakei was also used for shape analysis imaging. Prior to using the SEM, samples were vacuum-coated in platinum (University of Waikato) or gold (GNS Science). SEM operating conditions for thin sections involved an accelerating voltage of 15-20 kV, while 5.0 kV was used to image small pieces of scoria.

Backscattered images were taken at multiple magnifications (at the µm to mm scale) of crystal zonation, melt inclusions, and groundmass textures in representative thin sections. Energy dispersive spectroscopy (EDS) analyses were carried out to confirm various components present in the 1975 clasts (Appendix 5). Secondary electron imaging of thin sections and small pieces of scoria were also obtained, illustrating internal vesicle shapes/sizes and surface vesicle morphologies, respectively. Small pieces of scoria (~2 mm in size) suitable for observation under the SEM were cut off larger scoria clasts with a saw to avoid destruction of surface vesicle morphologies.

4.3.2 Mineralogy

Table 4.1 summarises component percentages calculated for samples from the 1975 inner crater rim deposit, based on point counting of thin sections.

Component percentages are normalised for zero vesicles, with the exception of vesicle percentages which are original values. The total counts analysed for each sample are also provided.

4.3.2.1 Plagioclase feldspar

Plagioclase feldspar is the most dominant phenocryst phase within both clast types of the 1975 inner crater rim deposit, with proportions ranging from 17% to 40% of the whole rock (vesicle free) (Table 4.1). Plagioclase can be separated into large phenocrysts or antecrysts (greater than 125 μm in size), and smaller microphenocrysts (125 μm or smaller). The modal abundance of large plagioclase phenocrysts ranges from 11 to 34% of the whole rock (vesicle free), while microphenocrysts range in abundance from 6 to 19% (Table 4.1). Despite the wide range in sizes, the overall size range for plagioclase is similar in both clast types. Plagioclase phenocrysts typically range from 100 μm to 1 mm, with some larger crystals up to 2.6 mm in size.

Plagioclase crystal forms are typically euhedral but range to subhedral (with subhedral morphologies more commonly observed in larger phenocrysts). Although the majority of plagioclase occurs as discrete grains, glomerocrysts are also common. Some glomerocrysts consist solely of plagioclase (Figure 4.3 A), while others have varying combinations of plagioclase, clinopyroxene, and orthopyroxene. Resorption textures such as sieve textures and embayments are another common feature of plagioclase in both clast types, particularly in larger crystals (Figure 4.4). Fine to coarse sieving is present, with crystals typically displaying sieved centres with non-sieved rims, or multiple clear and sieved concentric zones. Almost all of the sieved plagioclase crystals have a clear non-sieved rim (Figure 4.4). Zoning is also present in some crystals (Figures 4.3 C and D), in addition to mineral and melt inclusions (Figure 4.3 B).

Table 4.1 Percentages of various petrographic components (normalised for zero vesicles) within samples collected from different facies of the 1975 inner crater rim deposit. Refer to Figure 3.7 and Appendix 1 for the location of sample collection.[1]

Sample	Plag (L)	Plag (s)	Cpx (L)	Opx (L)	Ol	Pyroxene (s)	Opaque	Groundmass	Lithics	*Vesicles*[2]	Total Count[3]
Ad1	21	17	3	5	0.6	3	0.9	47	3	*13*	377
Ad2	15	17	4	3	0.0	3	N/A	57	1	*13*	399
Av1	15	13	0	4	0.0	6	0.0	62	0	*54*	114
Bd1	21	19	2	2	1.1	2	0.0	49	3	*3*	293
Bd2	34	N/A	6	2	0.2	N/A	2.9	56	0	*4*	545
Bv1	20	17	5	1	0.0	4	N/A	52	0	*49*	423
Bv2	14	16	7	2	0.6	5	N/A	55	1	*48*	317
Bv3	11	11	1	3	0.0	1	N/A	72	0	*58*	336
Cd2	22	15	3	3	0.0	3	N/A	51	3	*12*	522
Cd3	19	17	2	4	0.4	5	0.4	52	1	*12*	302
Cv1	14	13	4	2	0.0	2	N/A	65	2	*48*	382
Cv2	14	10	4	1	0.0	1	N/A	67	3	*48*	420
D1d1	17	N/A	4	1	0.2	N/A	N/A	76	2	*1*	439
D1d2	19	15	3	4	0.4	2	N/A	52	4	*4*	477
D1v1	12	7	3	1	0.0	3	N/A	71	3	*34*	351
D1v2	18	12	3	2	0.0	2	N/A	62	2	*35*	458
D2	21	10	2	1	0.0	2	N/A	60	3	*18*	535
D2d1	16	13	5	2	0.0	4	0.0	58	2	*4*	507
D2d2	14	15	3	1	0.0	2	N/A	65	1	*9*	440
D2v1	17	10	1	1	0.0	1	N/A	69	1	*36*	414
D3d1	15	13	4	2	0.5	3	N/A	61	2	*6*	585
D3v	16	6	1	1	0.0	1	N/A	73	1	*49*	408

[1]Abbreviations: plag = plagioclase, cpx = clinopyroxene, opx = orthopyroxene, ol = olivine, L= large phenocryst, and s = microphenocryst.

[2]Original vesicle percentages.

[3]Total count includes vesicle counts.

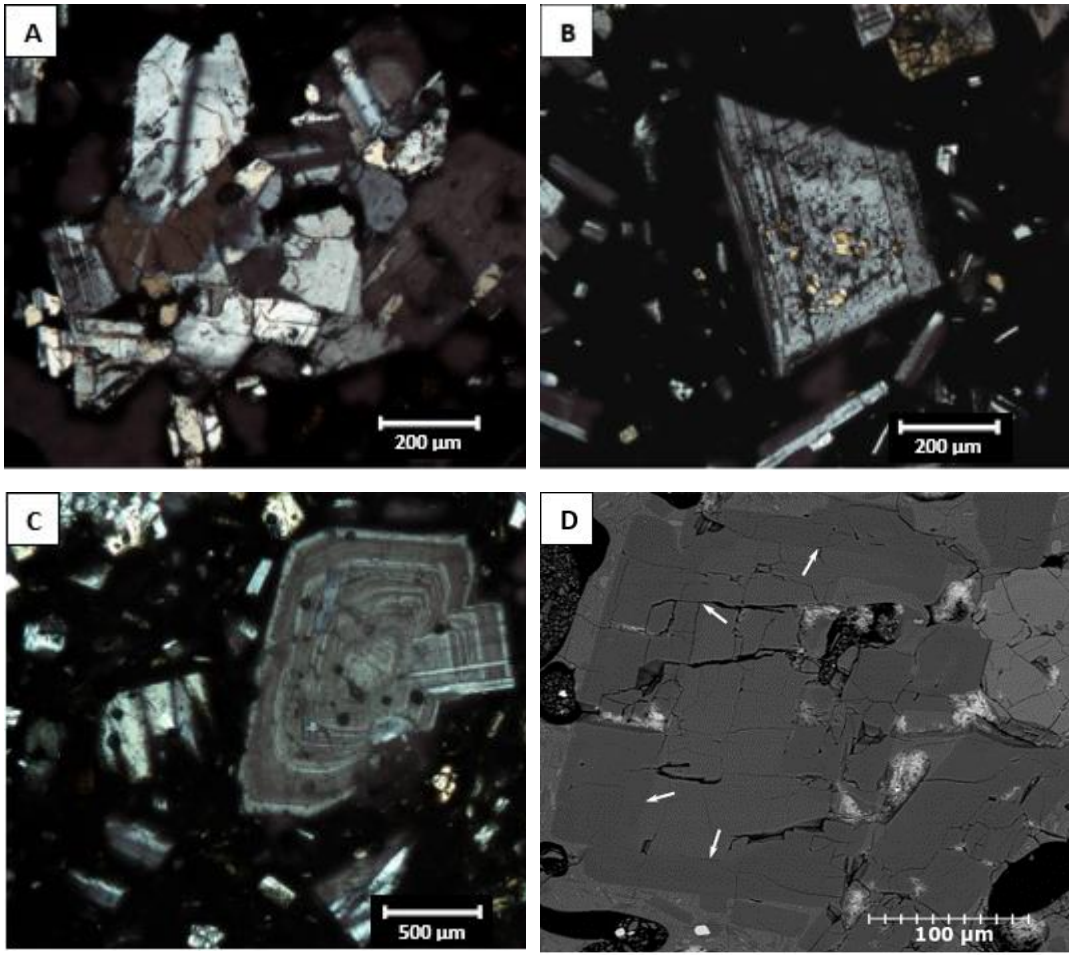

Figure 4.3 Various characteristics of plagioclase crystals within samples from the 1975 Ngauruhoe inner crater rim deposit. Photomicrographs A, B, and C, taken under cross polarised (XP) light, and image D taken using backscattered electron imaging. A) Glomerocryst of plagioclase crystals, B) mineral inclusions in a plagioclase crystal, C) multiple zones within a plagioclase phenocryst, and D) zoned plagioclase with a darker shade of grey around the rim of the crystal (depicted by white arrows).

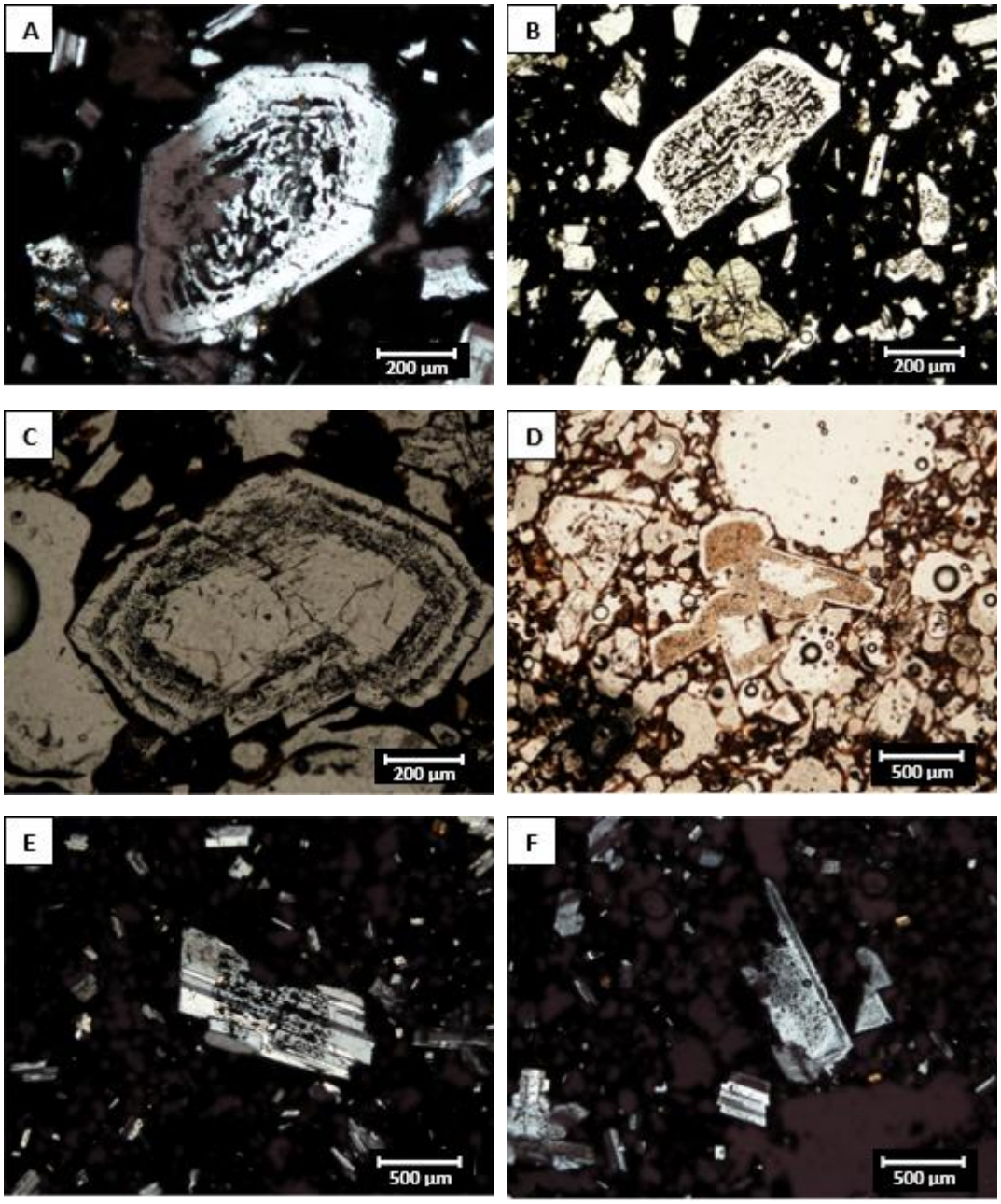

Figure 4.4 Resorption textures of plagioclase crystals. Photomicrographs A, E, and F taken under cross-polarised light, and photomicrographs B, C, and D taken under plane polarised (PP) light. A) Coarse sieve texture of plagioclase core, B) plagioclase with a coarsely sieved core and a pristine rim, C) multiple concentric sieved and non-sieved zones, D) fine sieve texture of plagioclase phenocrysts with clear core and rim, E) plagioclase with sieved core, pristine rim and embayment, and F) highly resorbed and sieved subhedral plagioclase.

4.3.2.2 Pyroxenes

Orthopyroxene and clinopyroxene are the two pyroxene phases present in the 1975 inner crater rim deposit. They appear to be approximately equal in abundance, with orthopyroxene having a modal abundance ranging from <1 to 5%, and clinopyroxene having a modal abundance ranging from <1-7% of the whole rock (vesicle free) (Table 4.1). Both pyroxenes occur predominantly as discrete crystals, however they also occur as glomerocrysts in both clast types (with varying combinations of clinopyroxene, orthopyroxene, and plagioclase) (Figure 4.5).

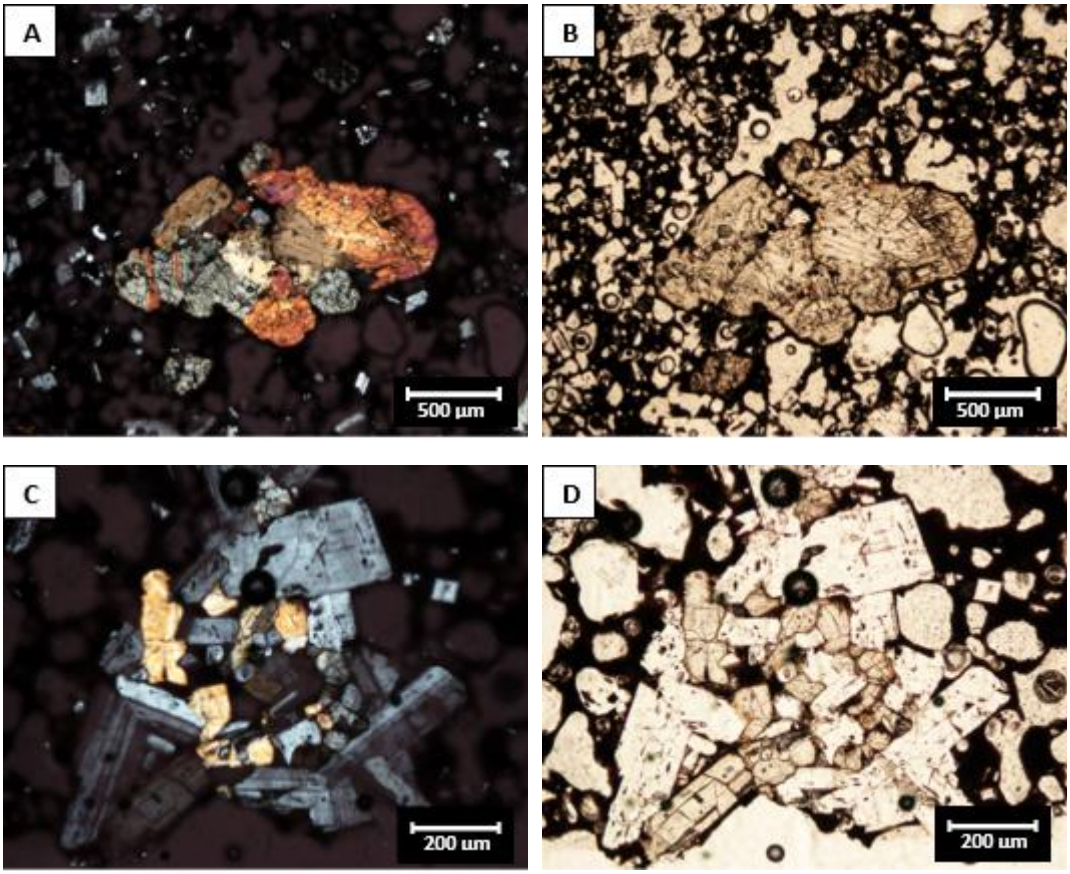

Figure 4.5 Photomicrographs of glomerocrysts under XP light (images on the left), and the same photomicrographs under PP light (images on the right). A) and B) depict a glomerocryst containing mostly clinopyroxene crystals, while C) and D) depict a glomerocryst containing a mixture of orthopyroxene, clinopyroxene, and plagioclase.

Orthopyroxene mostly occurs as euhedral crystals (although some subhedral forms were also observed), often with more elongate shapes compared to clinopyroxene crystals (Figure 4.6 A). Orthopyroxene phenocrysts have an average size of 300-500 µm and a maximum size of 2.2 mm, with no obvious differences between dense and scoria clasts. Although resorption textures are not common, cavities and embayments were observed in a few larger crystals (Figure 4.6 B).

Orthopyroxene also commonly contains melt inclusions and mineral inclusions of plagioclase and clinopyroxene. Orthopyroxene is sometimes zoned (Figure 4.7) and is occasionally rimmed by clinopyroxene, however, this is not a common occurrence in the 1975 Ngauruhoe crater rim clasts.

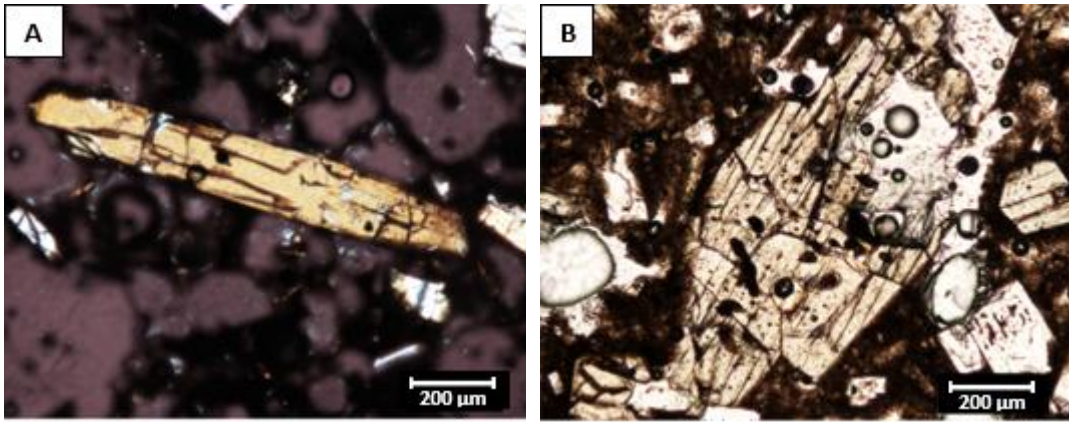

Figure 4.6 Photomicrographs showing A) an elongate euhedral orthopyroxene (opx) crystal under XP light, and B) a subhedral, embayed opx crystal from a dense clast observed under PP light.

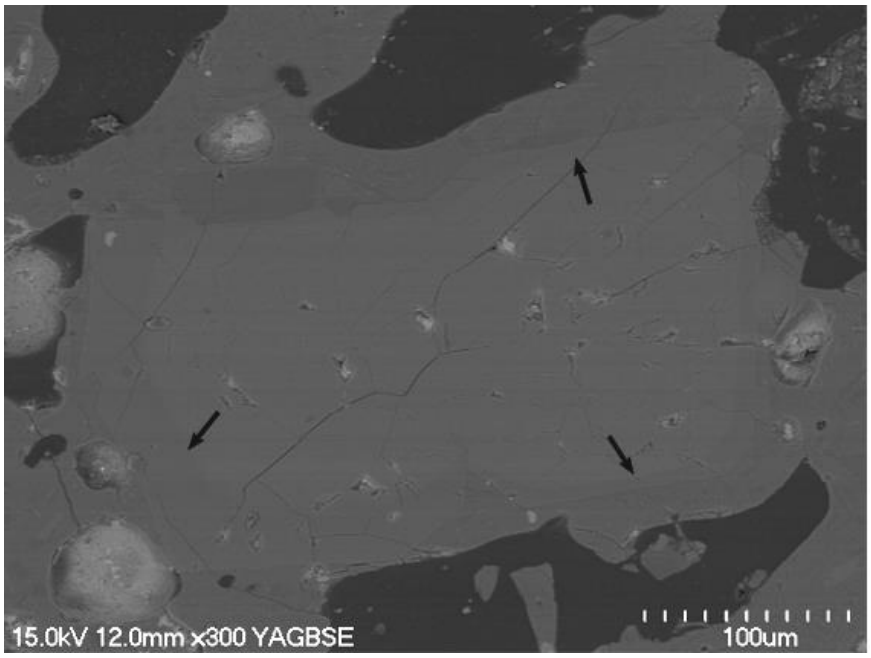

Figure 4.7 Backscattered electron SEM image depicting zoning of an orthopyroxene phenocryst. Black arrows pointing to outer rim with a different composition represented by the slightly darker shade of grey.

Clinopyroxene occurs as euhedral to subhedral crystals which are typically pale brown under plane polarised (PP) light, with moderate relief. They commonly display simple twins (Figures 4.8 A and B). Clinopyroxene phenocrysts have a similar size range in both clast types, with an average size of approximately 400 µm and a maximum size of around 2 mm. Some crystals display resorption textures including cavities and embayments (Figure 4.8 C), and a few clinopyroxene

phenocrysts also contain mineral (both plagioclase and pyroxene) and/or melt inclusions (Figures 4.8 D and 4.9). Refer to Appendix 5 for EDS analyses of mineral and melt inclusions within the clinopyroxene crystal shown in Figure 4.9. Zoning of clinopyroxene was not observed under the petrographic microscope, however backscatter imagery on the SEM depicted zoning in numerous crystals (Figure 4.10).

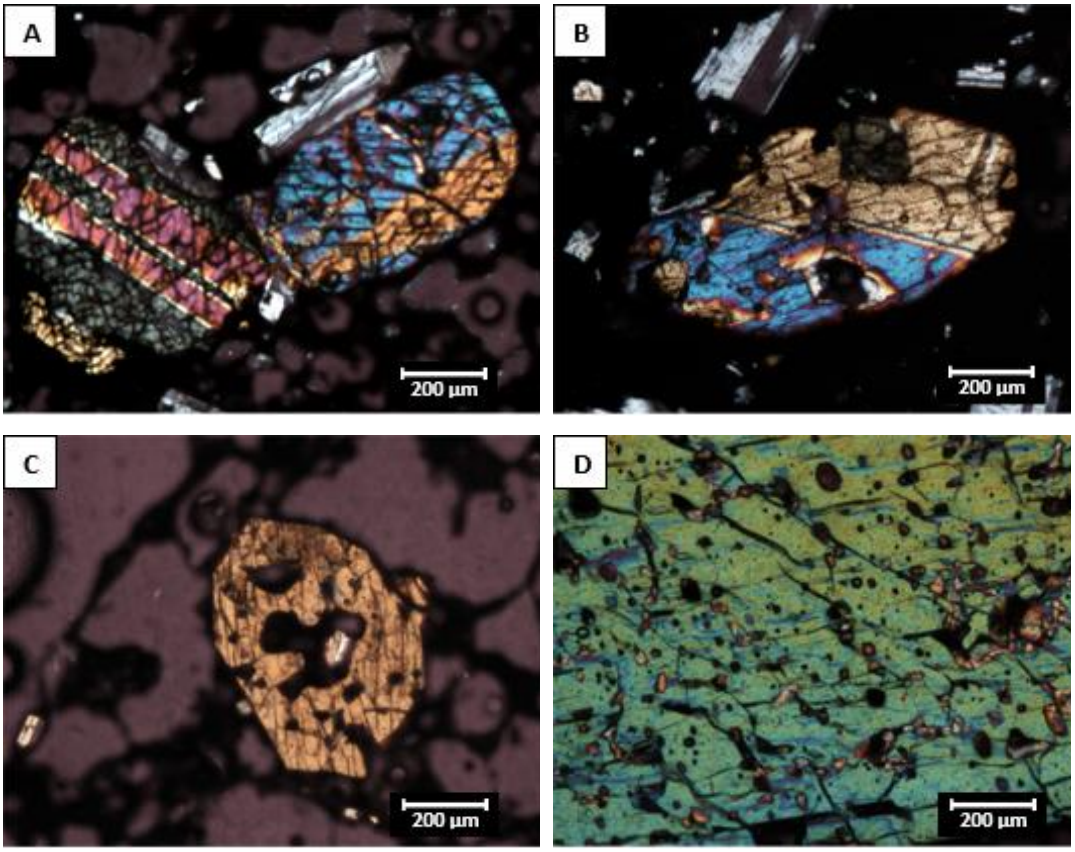

Figure 4.8 Photomicrographs of clinopyroxene (cpx) crystals observed under XP light. A) Euhedral cpx phenocrysts displaying simple twins, B) subhedral cpx with embayments and simple twins, C) resorbed cpx with cavities, and D) mineral inclusions (coloured inclusions) within a cpx phenocryst.

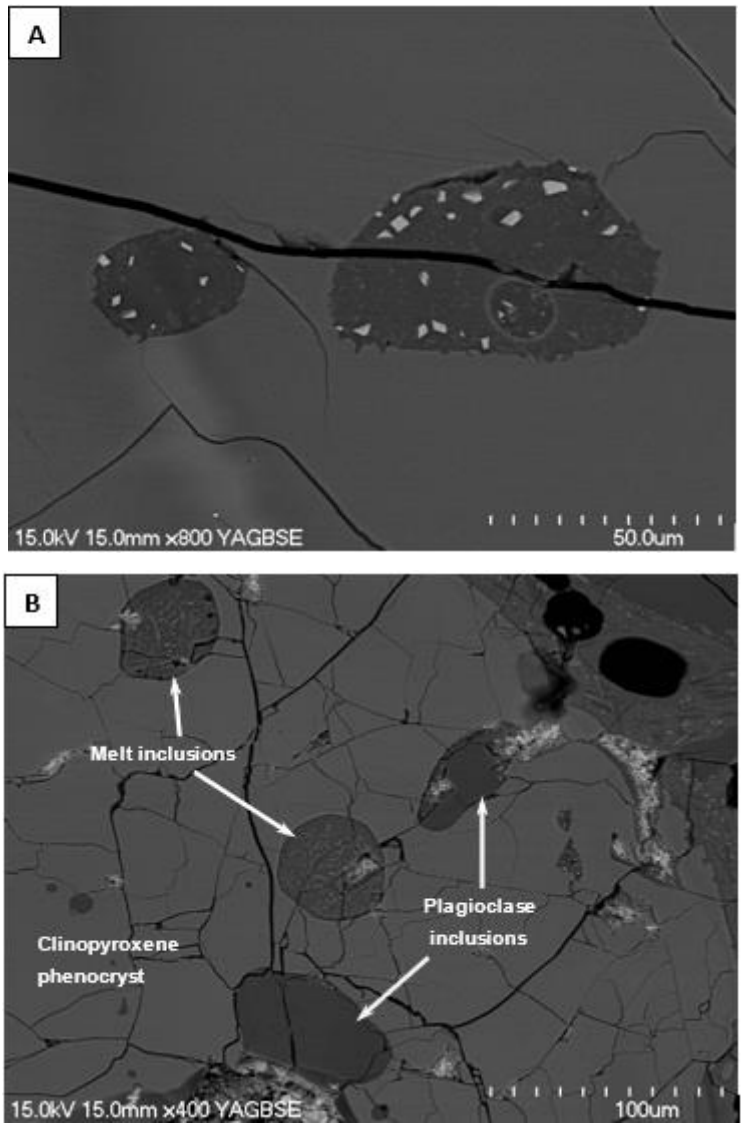

Figure 4.9 Backscattered electron SEM images showing A) melt inclusions with varying crystallite concentrations, and B) plagioclase and melt inclusions within a clinopyroxene phenocryst from a juvenile scoria clast.

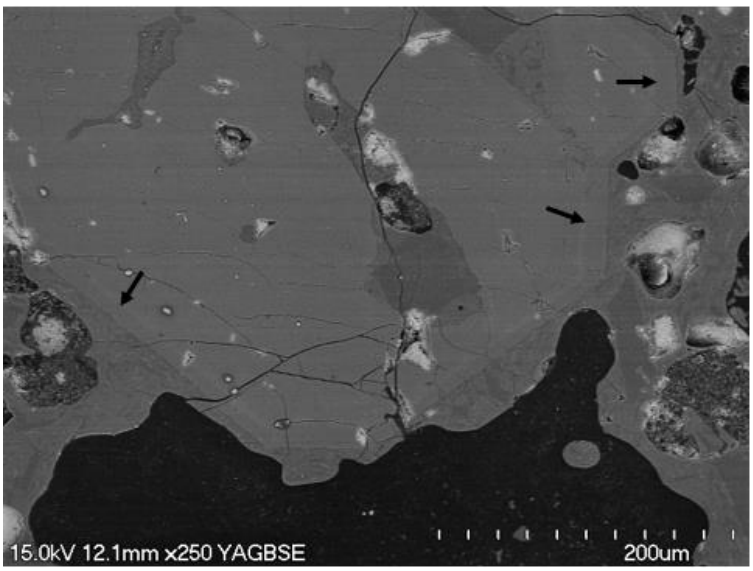

Figure 4.10 Backscattered electron SEM image depicting zoning of a clinopyroxene phenocryst in a scoria clast from the 1975 Ngauruhoe eruption. Black arrows pointing to outer rim with different composition represented by the slightly darker shade of grey.

4.3.2.3 Olivine

Olivine is the least common phenocryst in the dense and vesicular samples from the 1975 Ngauruhoe eruption deposit, with an abundance of up to approximately 1% of the whole rock (vesicle free) and not present in every thin section (Table 4.1). Olivine crystals (averaging 100 µm in length) are generally smaller relative to the average size of plagioclase and pyroxene phenocrysts. The typical olivine in both dense and vesicular samples is sub-rounded/subhedral (Figure 4.11).

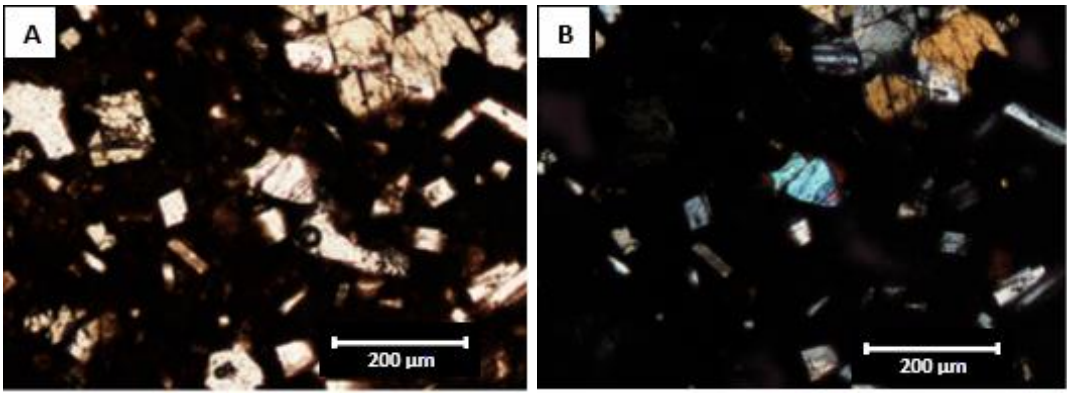

Figure 4.11 Photomicrographs of a small, subhedral to anhedral, olivine phenocryst under PP light (A) and XP light (B).

Some, but not all, olivine phenocrysts are rimmed by pyroxene (Figures 4.12 and 4.13), and this was also observed by Krippner (2009) in the 1954-55 Ngauruhoe inner crater samples, Sanders (2010) in the 1954 lava flows, and Griffin (2007) in the Tongariro North Crater deposits. An SEM-EDS line-scan showing changes in elemental counts from the groundmass towards the middle of the crystal (Figure 4.14) was conducted on an olivine phenocryst with an orthopyroxene rim (Figure 4.13).

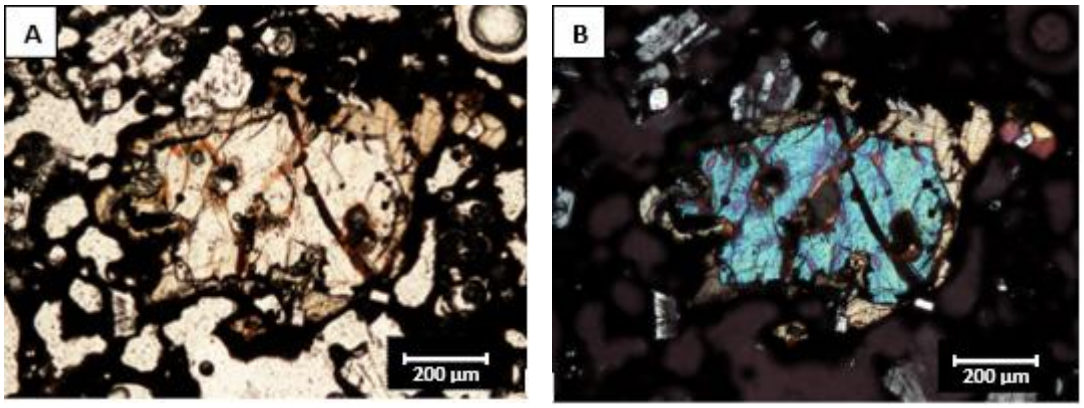

Figure 4.12 Photomicrographs of an olivine phenocryst with a pyroxene rim observed under A) PP light, and B) XP light.

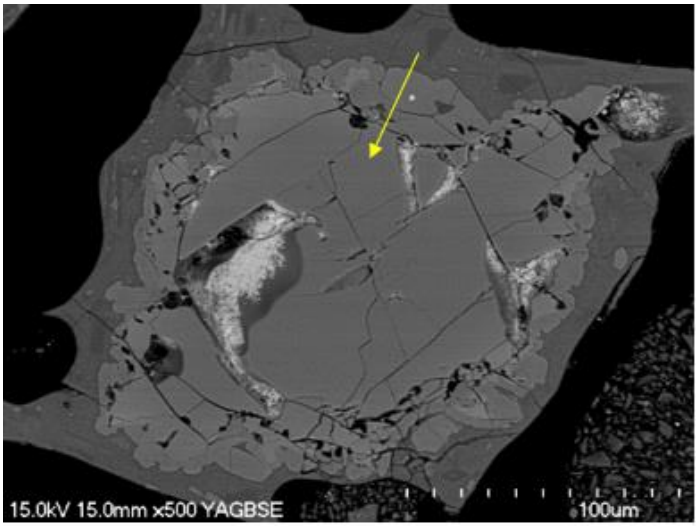

Figure 4.13 Backscattered electron SEM image of an olivine phenocryst within a juvenile scoria clast from the 1975 inner crater rim deposit. The slightly darker shade of grey around the edge of the crystal represents a pyroxene rim. Also note the arrow representing the location of the elemental line-scan displayed in Figure 4.14.

Silica was found to have the highest count in the surrounding groundmass, with a noticeably lower count in the crystal rim, and a further decrease towards the middle of the crystal (Figure 4.14). Magnesium showed the opposite trend to silica with a significant increase towards the middle of the crystal, and a substantial difference between the core and rim (Figure 4.14). There was also a slight increase in iron from the surrounding groundmass towards the middle of the crystal.

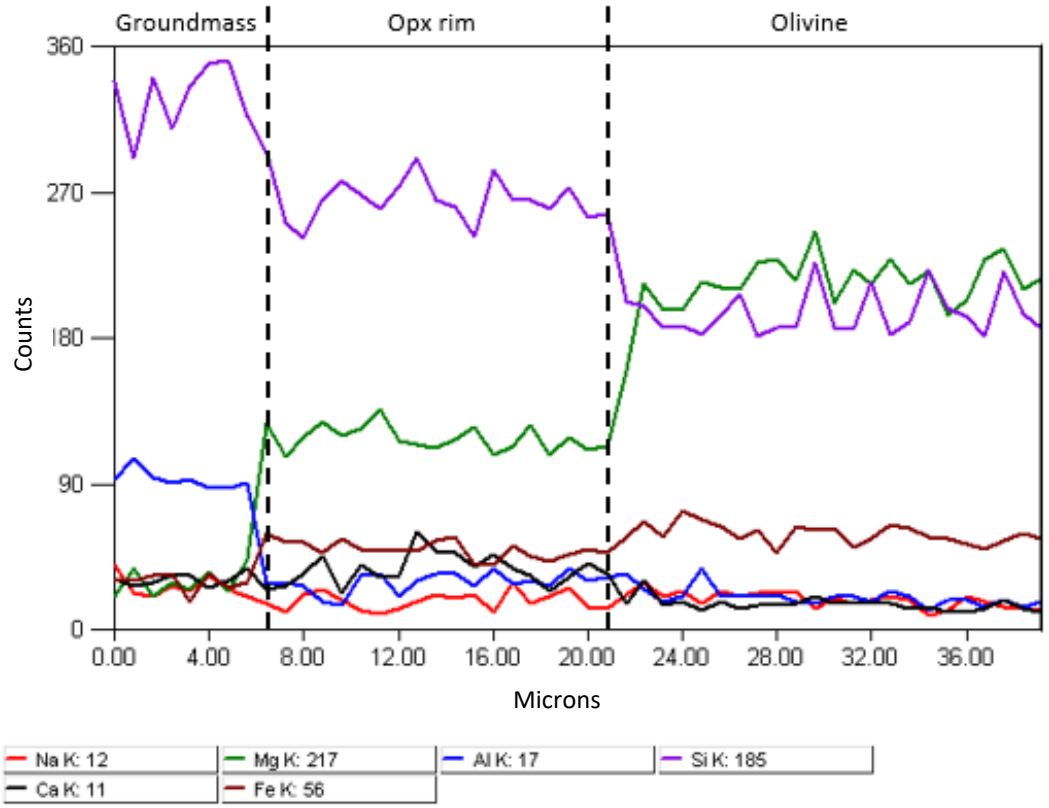

Figure 4.14 Line-scan graph illustrating element counts for various points along the line depicted in Figure 4.13 (from the surrounding groundmass glass towards the middle of the olivine crystal).

4.3.2.4 Opaque minerals

Small, euhedral, Fe-Ti oxide microphenocrysts (up to ~100 µm in size) are present in most of the samples from the 1975 inner crater rim deposit (Figures 4.15 – 4.17). Point counting abundance data was not obtained for opaque phenocrysts since most samples typically have a black groundmass, making them difficult to observe petrographically. However, backscattered electron imagery on the SEM clearly depicted opaque microphenocrysts scattered throughout both dense and vesicular clasts (Figure 4.17). Opaque microphenocrysts typically have a characteristic triangular to cubic shape (Figures 4.15 and 4.17 A-C), although a few rectangular and irregular crystal shapes were also observed (Figure 4.17 D). It is important to note that plagioclase is often overgrown by magnetite.

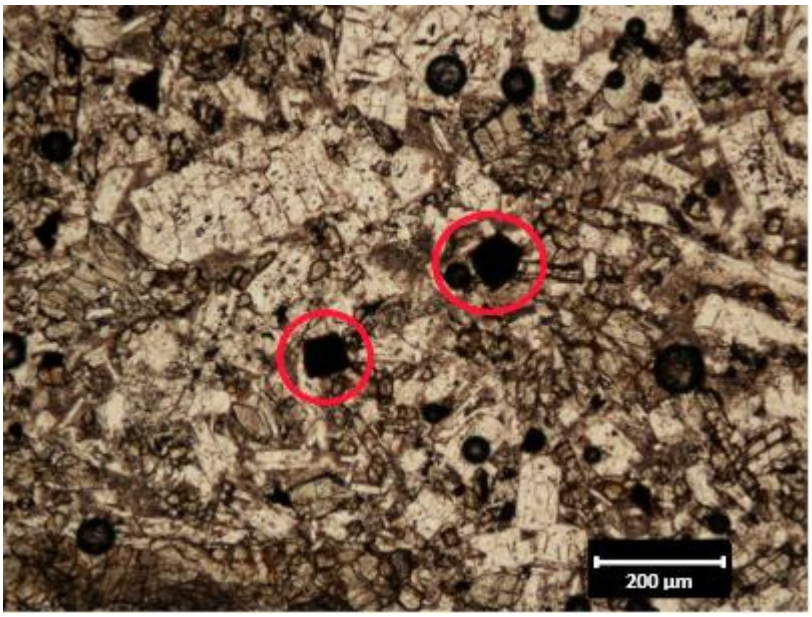

Figure 4.15 Photomicrograph taken under PP light, depicting opaque microphenocrysts within a dense clast. Note the characteristic cubic shape and jet-black colour of opaque minerals shown within the red circles.

Figure 4.16 A shows a typical EDS analysis of most of the opaques analysed. Based on this semi-quantitative data from the SEM it is likely that opaque minerals are predominantly magnetite (since iron is significantly higher than titanium) (Appendix 5). The cubic shape of opaques is another indicative feature of magnetite. Ilmenite is present in minor quantities as indicated by approximately equal proportions of iron and titanium in a few EDS analyses (Figure 4.16 B; Appendix 5).

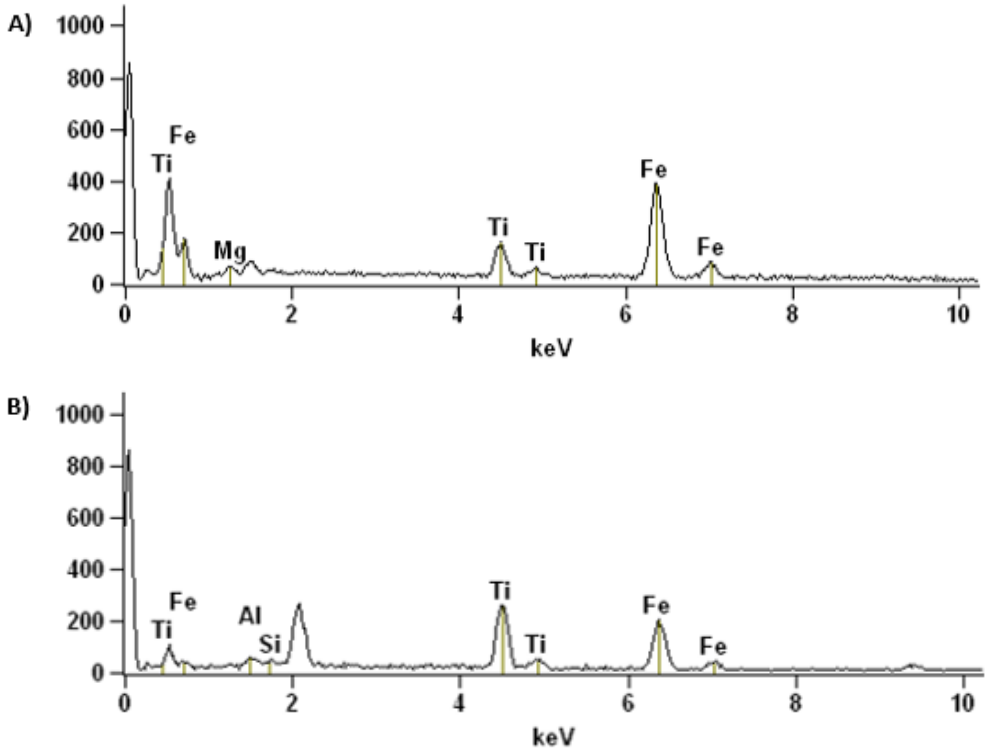

Figure 4.16 Two different EDS analyses of opaque crystals (where the y-axis represents elemental counts). A) EDS results indicative of magnetite and typical of most opaques analysed with the SEM, and B) EDS results indicative of ilmenite with approximately equal amounts of iron (Fe) and titanium (Ti). Refer to Appendix 5 for the full analysis of each crystal.

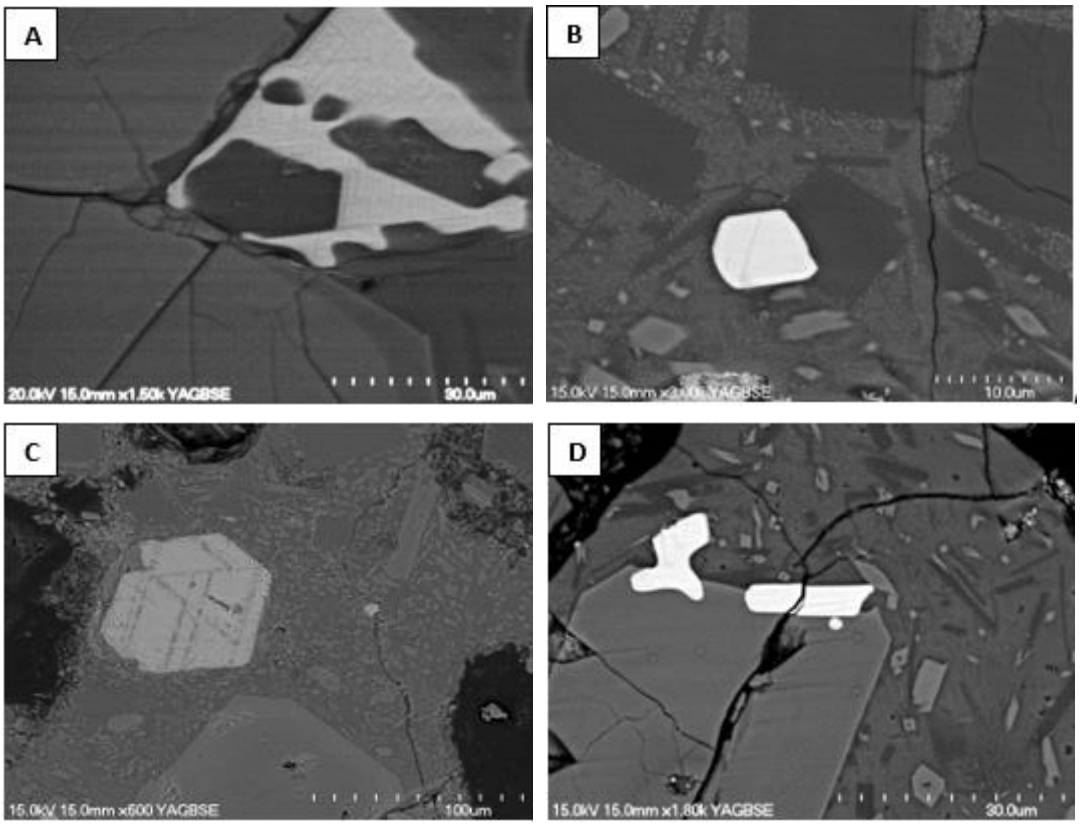

Figure 4.17 Backscattered electron SEM images of opaque microphenocrysts in clasts from the 1975 inner crater rim deposit of Ngauruhoe. The opaques are the brightest grains in each image. A) Opaque microphenocryst adjacent to a zoned pyroxene phenocryst in a scoria clast (note thatched texture on opaque mineral), B) cubic opaque microphenocryst within a scoria clast, C) cubic opaque microphenocryst in a dense clast, and D) rectangular and irregularly shaped opaques within a scoria clast.

4.3.3 Groundmass Textures

4.3.3.1 Moderately vesicular scoria clasts

Most scoria clasts from Facies A and B are black in hand specimen, while scoria clasts from Facies C and D are reddish-brown due to a higher degree of oxidation. Subsequently, differences in groundmass colour and crystallite content were observed in thin section. The glassy groundmass in scoria clasts from Facies C and D typically displays a black/opaque tachylyte appearance, with some reddish-brown tinges (Figure 4.18 A). In contrast, the glassy groundmass in scoria clasts from Facies A and B is typically brown with fewer dark/opaque areas due to a lesser degree of oxidation (Figure 4.18 B).

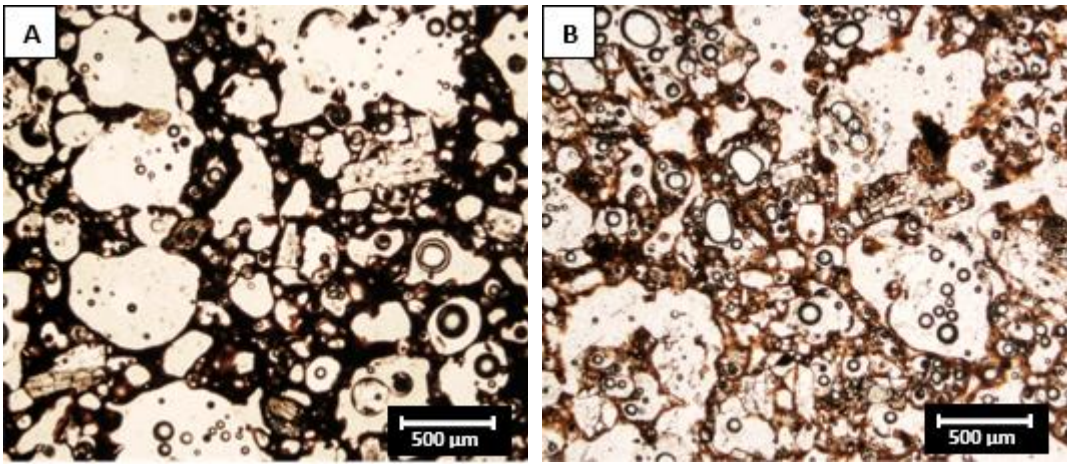

Figure 4.18 Photomicrographs taken under PP light showing groundmass colour variations between some of the scoria clasts from the 1975 Ngauruhoe inner crater rim deposit. A) Black/opaque glassy groundmass in a scoria clast from Facies C, and B) brown glassy groundmass in a scoria clast from Facies A.

The black scoria clasts from Facies A and B displayed some visible crystallites (too small to identify under the petrographic microscope) randomly orientated within the glass, giving it a hyalopilitic texture (Figures 4.19 A and B). Crystallites include tiny needle and lath-like plagioclase and pyroxene crystals as revealed by EDS analyses (Appendix 5), with an average size of ~20 µm. It was difficult to observe crystallites in the red scoria clasts from Facies C and D due to the opaque groundmass under PP light. However, SEM imagery confirmed that crystallites were more abundant compared to the black scoria clasts which had a greater proportion of crystal-free glass (Figures 4.19 B and 4.20). The glassy groundmass in all scoria clasts is crowded by tiny iron oxide granules which appear slightly larger in the red scoria (Figures 4.19 C and 4.20).

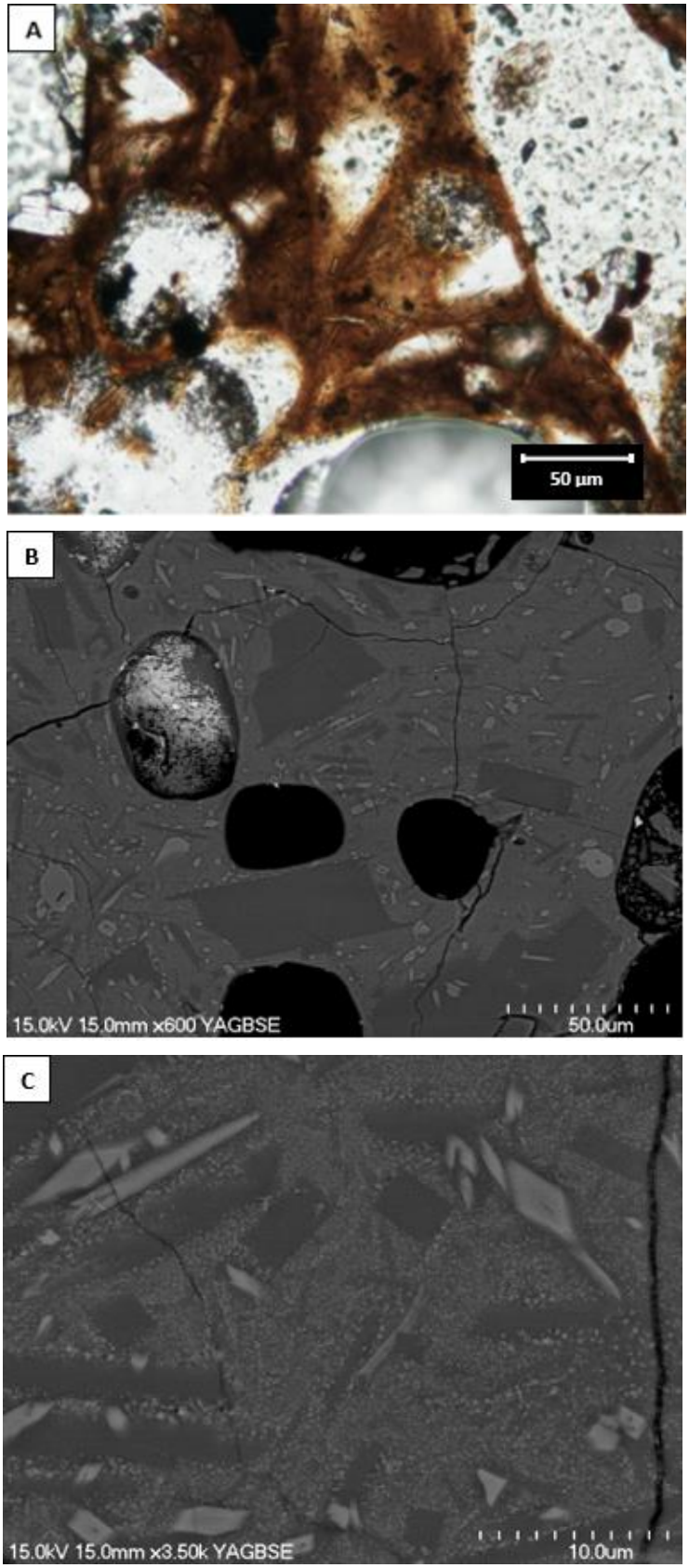

Figure 4.19 Images depicting the groundmass of a black scoria clast. A) Photomicrograph taken under PP light showing tiny transparent crystallites within the brown glassy groundmass, B) backscattered electron SEM image showing tiny pyroxene and plagioclase crystallites and microlites within the groundmass, and C) backscattered electron SEM image showing tiny specks of Fe-Ti oxides disseminated throughout the glassy groundmass. Notice how there are glass patches in the black scoria clasts which are free of microlites and crystallites (with the exception of the tiny Fe-Ti oxides).

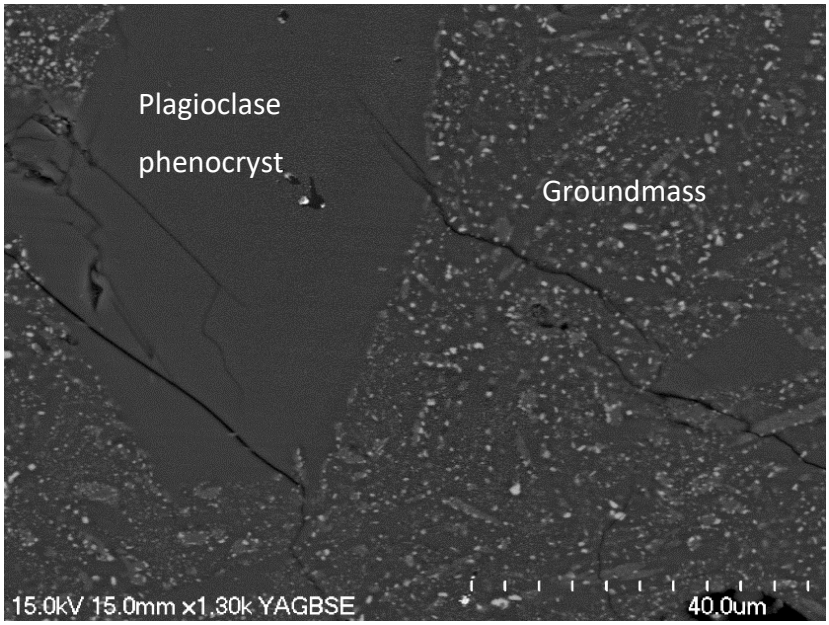

Figure 4.20 Backscattered electron SEM image depicting a large plagioclase phenocryst surrounded by the groundmass of a red scoria clast. Notice the more crystalline nature of the groundmass compared to the black scoria clasts (Figure 4.19). There are bright white specks of Fe-Ti oxides disseminated throughout the groundmass, responsible for the black tachylyte appearance observed petrographically.

4.3.3.2 Dense (poorly vesicular) clasts

Dense clasts throughout the 1975 inner crater rim deposit display varying textures as observed under the petrographic microscope and SEM. Many of the dense clasts have a glassy groundmass with a tachylyte appearance (i.e. the groundmass is dark black in colour and sometimes mottled due to very fine iron-oxides produced from the devitrification of glass) (Figures 4.21 A and B). High magnification SEM imagery depicts these opaques as tiny white specks in the groundmass (Figures 4.22 and 4.23 B). Some areas of groundmass also display a reddish-brown tinge due to the presence of hematite which is oxidised to a greater extent than magnetite.

Most of the dense clasts contain abundant crystallites (too small to identify petrographically) and microlites in the groundmass, which are randomly orientated in a hyalopilitic texture (Figures 4.21 C and D). The microlites are predominantly euhedral and lath-shaped with an average length of ~30 μm, while crystallites are typically <10 μm. EDS analyses confirm that crystallites and microlites include both pyroxenes and plagioclase, although microlites are predominately plagioclase (Figure 4.22; Appendix 5).

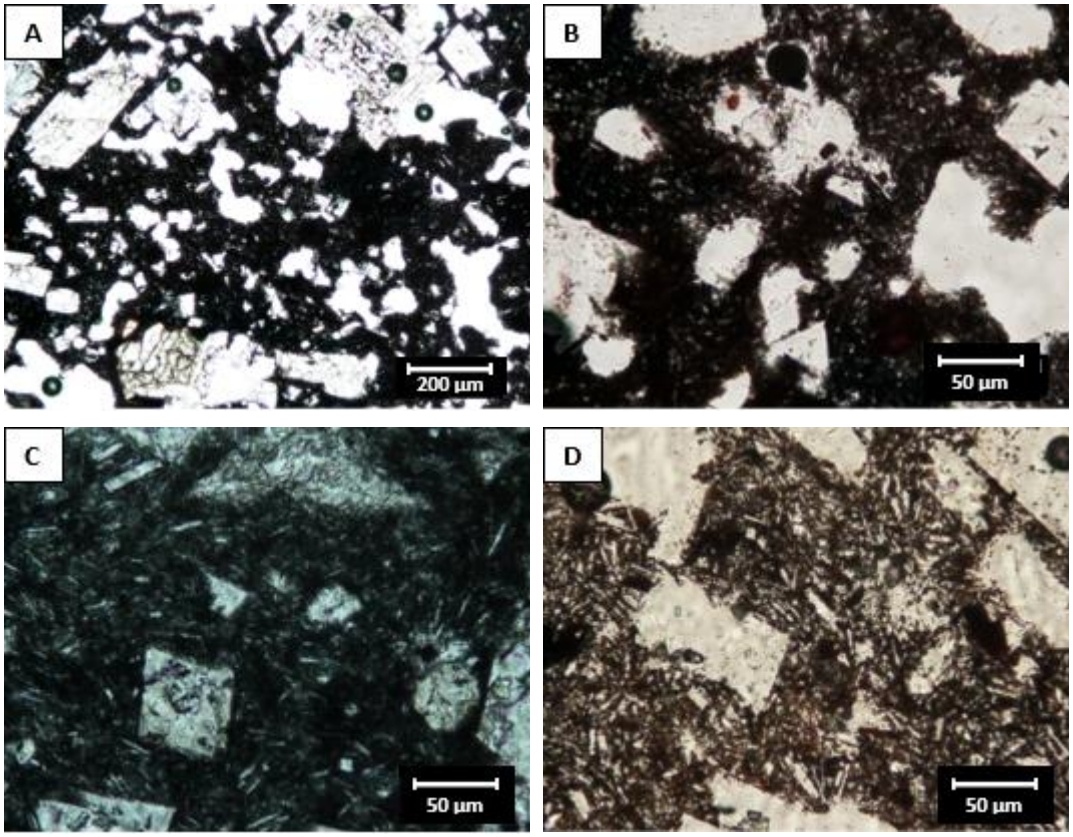

Figure 4.21 Photomicrographs under PP light depicting the tachylyte groundmass in dense clasts from the 1975 inner crater rim deposit. The groundmass appears black in colour under PP light (A) and sometimes mottled (B) due to a high abundance of opaque Fe-Ti oxides. Photomicrographs B, C and D illustrate how dense clasts have varying proportions and sizes of opaques and microlites/crystallites in the groundmass.

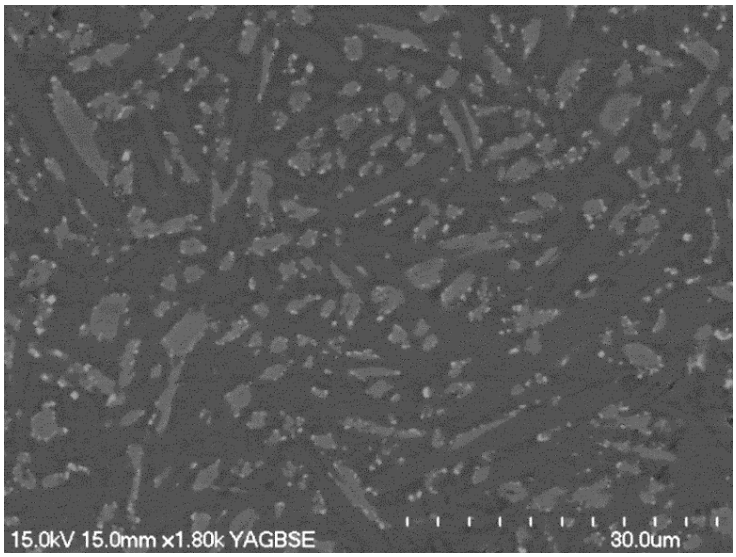

Figure 4.22 Backscattered electron SEM image of a dense clast with tachylyte groundmass that is slightly more crystalline than most of the dense clasts observed. Light grey crystals are pyroxenes, dark grey crystals are plagioclase, and white specks are Fe-Ti oxides. Refer to Appendix 5 for EDS analyses of the various components.

A few dense clasts in Facies C and D have a coarser-grained groundmass compared to other dense clasts (Figure 4.23). These clasts appear to contain less glass due to the high abundance of groundmass crystallites/microlites, and the iron-oxide granules are coarser and more disseminated throughout the groundmass (Figure 4.23).

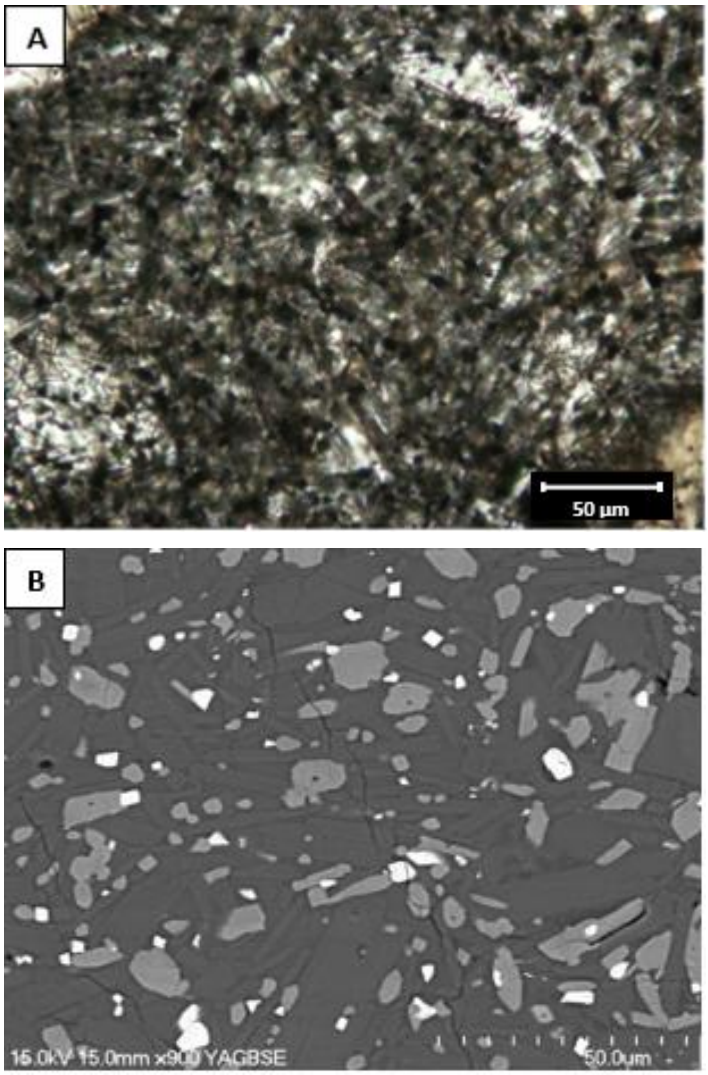

Figure 4.23 Images depicting the crystal-rich groundmass of a dense clast from facies C. A) Photomicrograph taken under PP light; notice the abundant transparent crystallites within the groundmass and the black opaque granules scattered throughout. B) Backscattered electron SEM image illustrating pyroxene (light grey) and plagioclase (dark grey) crystallites, in addition to Fe-Ti oxides (bright white granules) disseminated throughout the groundmass. Refer to Appendix 5 for EDS analyses of the various components.

Some dense clasts from facies A and B contain a fresh, light brown to brown, glassy groundmass. These clasts also have abundant crystallites and microlites (approximately the same size as those in the other dense clasts) randomly oriented within the groundmass glass (Figure 4.24). One of the clasts from facies A exhibits irregular and whispy bands of fresh, transparent, light brown glass that contains fewer microlites compared to the areas of brown translucent

groundmass (Figure 4.24 A). The transparent groundmass is also coarser-grained than the translucent parts (microlites in transparent bands average 40 µm in length, compared to ~20 µm in the translucent groundmass), with more patches of microlite-free glass due to a lower concentration of crystals (Figure 4.24 A).

In those clasts with brown glass it was also possible to see a low abundance of cubic opaque microphenocrysts disseminated throughout the groundmass. These Fe-Ti oxides are ~20 µm in size and have a definitive euhedral crystal shape (Figure 4.24 A).

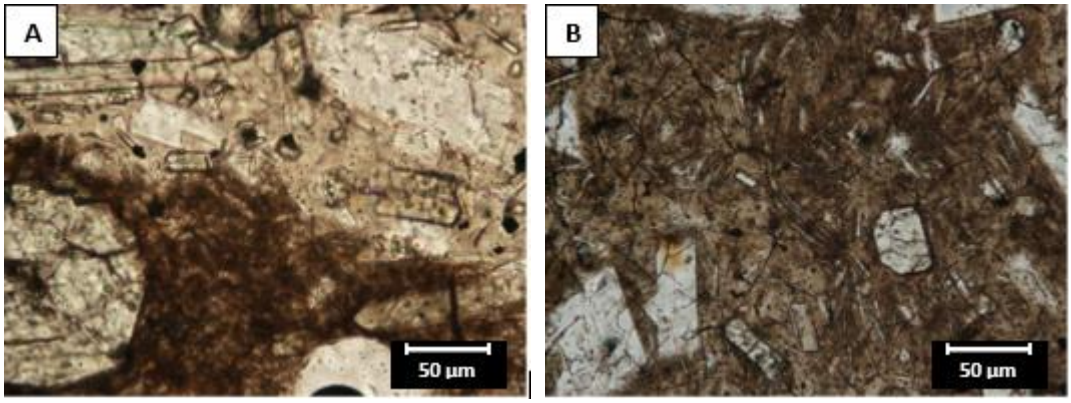

Figure 4.24 Photomicrographs taken under PP light showing brown glassy groundmass in a couple of dense clasts from facies A and B. A) Groundmass includes bands of transparent light brown glass with fewer microlites and crystallites compared to the brown translucent groundmass, and B) brown glassy groundmass containing abundant crystallites and microlites, with some patches of fresh microlite-free glass also visible.

One of the dense clasts observed from facies B displays a very different intergranular crystalline groundmass involving a random network of plagioclase laths, with interstices filled by small grains of pyroxenes (and possibly olivine) (Figures 4.25 and 4.26). The groundmass minerals have an average size of ~150 µm, and there are also rare isolated patches of glass within the groundmass. Opaque Fe-Ti oxide microphenocrysts scattered throughout this clast have an average size of ~80 µm (Figures 4.25 and 4.26).

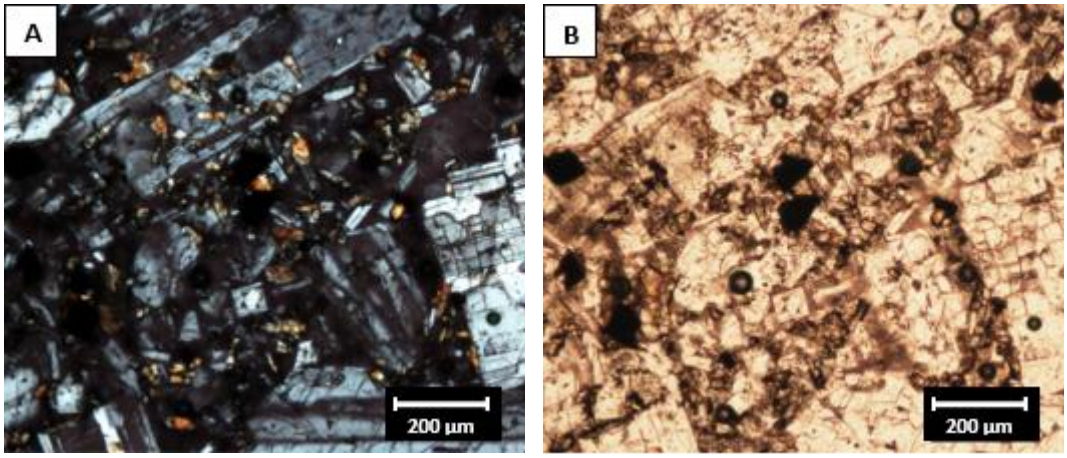

Figure 4.25 Photomicrographs depicting intergranular groundmass texture in a dense clast from the 1975 inner crater rim deposit under A) XP light, and B) PP light. Note the euhedral opaque Fe-Ti oxide crystals.

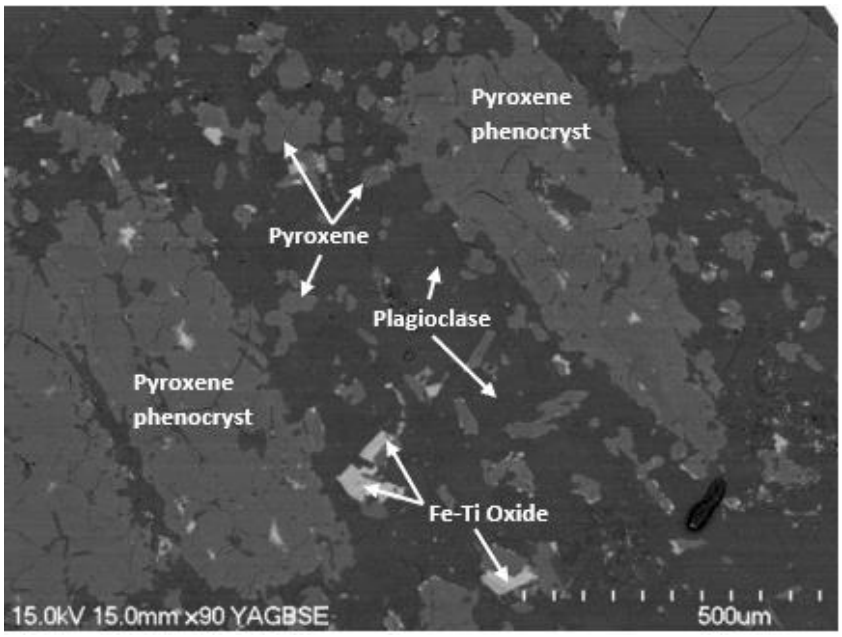

Figure 4.26 Backscattered electron SEM image of a 1975 dense clast, illustrating pyroxene phenocrysts within an intergranular groundmass consisting of a network of plagioclase, pyroxene and opaque Fe-Ti oxide crystals.

4.3.4 Lithics/Xenoliths

Lithic clasts were not overly abundant in the 1975 inner crater rim exposure, however smaller-scale xenoliths were commonly observed in thin section (Figure 4.27). Point counting results indicate a modal abundance ranging from 0-4% of the whole rock (Table 4.1). Xenoliths are predominantly quartzofeldspathic (feldspar-rich but also containing varying amounts of quartz and Fe-Ti oxides), with equigranular grains arranged in a mosaic texture (Figures 4.27 A and B). Feldspathic (Figures 4.27 E and F) and quartzite xenoliths were also observed, although the quartzite xenoliths are less common and typically have larger anhedral quartz grains (averaging 500 µm) arranged in a

granoblastic/mosaic-like texture (Figures 4.27 C and D). Rare porphyritic xenoliths averaging ~2 mm in size were also observed (Figure 4.28), containing larger crystals (~150 µm) in a fine-grained groundmass (average grain size ~50 µm).

The average size of quartzofeldspathic and feldspathic xenoliths ranges from approximately 400 µm to 1 mm throughout the inner crater rim samples (while a maximum xenolith size of 5.25 mm was recorded). Average sizes of individual grains range from approximately 25 µm in the finer-grained xenoliths, to 80 µm in the coarser-grained xenoliths.

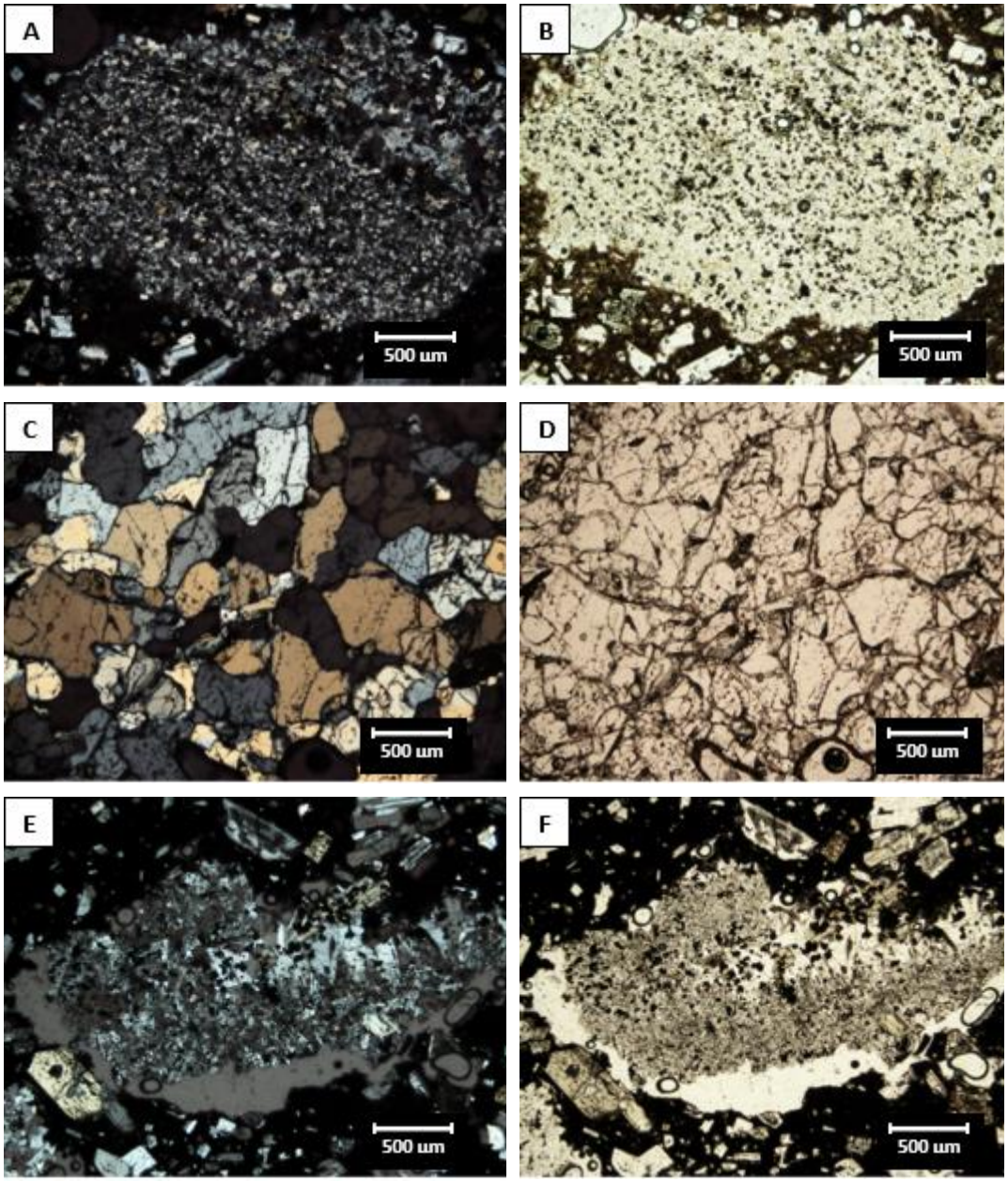

Figure 4.27 Photomicrographs of xenoliths observed within clasts from the 1975 inner crater rim deposit (images on the left taken under XP light, images on the right taken under PP light); including a fine-grained quartzofeldspathic xenolith (A and B), a coarse-grained granoblastic quartzite xenolith (C and D), and a fine-grained feldspathic xenolith containing plagioclase and tiny opaque minerals (E and F).

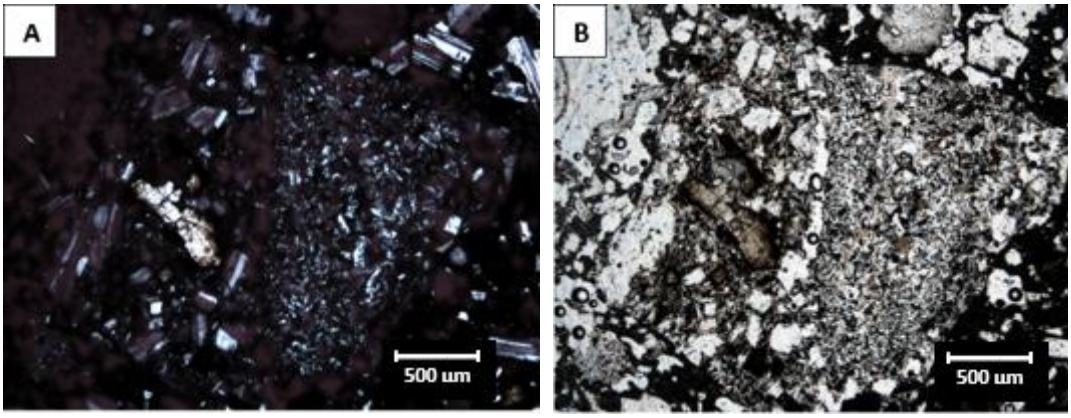

Figure 4.28 Photomicrographs under A) XP light and B) PP light, depicting a xenolith from Facies A with two different halves. The half on the left of each image is porphyritic with large plagioclase and orthopyroxene phenocrysts within a fine-grained groundmass, while the right half is feldspathic and equigranular.

4.3.5 Vesicles and Vesicle Texture

Petrographic observations depict two end members in terms of clast vesicle proportions; one group of dense, poorly vesicular clasts with modal vesicle abundances of less than 18%, and another group of moderately vesicular scoria clasts with modal vesicle abundances ranging from 34-58% (Table 4.1). Vesicles occur in a range of sizes in the 1975 clasts (Figure 4.29), from ~25 µm up to ~3 mm. The size range and average size (~250-500 µm) of vesicles is relatively consistent in both clast types throughout the inner crater rim deposit. Cross sections of the internal vesicles illustrate predominant irregular morphologies, less common sub-rounded morphologies, and some elongate morphologies resulting from vesicle coalescence (Figure 4.29).

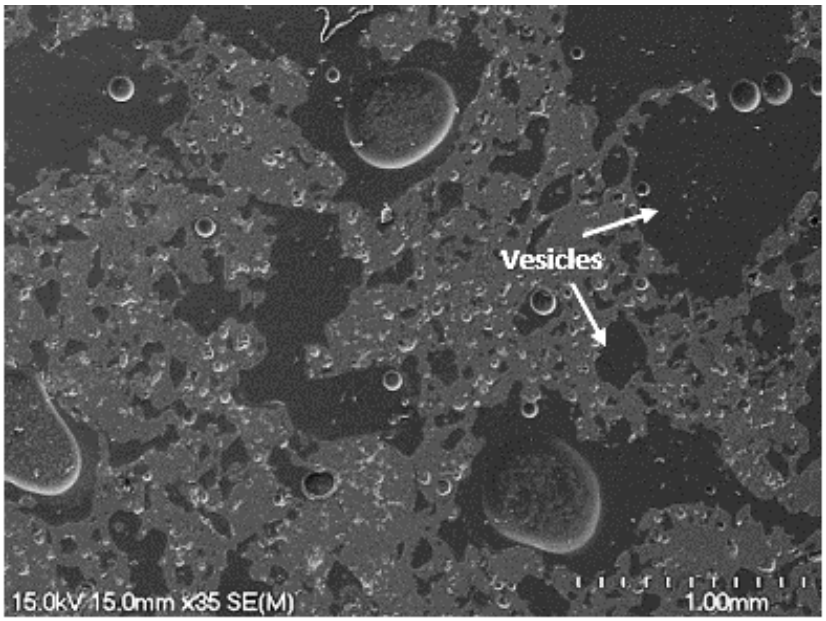

Figure 4.29 Secondary electron SEM image of a typical scoria thin section from the 1975 inner crater rim deposit. Vesicles are the dark grey areas indicated by the white arrows.

Some differences in surface vesicle morphologies were observed under the SEM between a highly vesicular scoria clast from Facies A (which floated in water) and a moderately vesicular scoria clast from Facies D (which did not float) (Figure 4.30). The clast from Facies A has a high abundance of well-preserved, sub-rounded to irregular shaped vesicles covering the surface (Figure 4.30 A). The surface of this clast is very rough and irregular compared to the moderately vesicular clast as it exhibits tightly packed/polygonal vesicles with thin vesicle walls (Figure 4.30 C), and also a high abundance of spherically intact bubble walls (Figures 4.30 E and G). The surface vesicles on this clast are mostly empty pore spaces (not infilled).

In contrast, the moderately vesicular scoria clast from Facies D contains a heterogenous vesicle distribution (Figures 4.30 B and D). The surface texture of this clast appears less irregular than the highly vesicular scoria clast, and vesicles have noticeably thicker walls (Figure 4.30 B). Surface vesicles are mostly irregular in shape, although sub-rounded (Figure 4.30 B) and slightly elongated (Figure 4.30 F) vesicle morphologies are also present. Unlike the clast from Facies A, this clast has a variety of both empty pore spaces and spaces that have been infilled by other material (Figure 4.30 H). Further EDS analyses are required to determine the composition of this material.

It is important to note that a majority of the juvenile scoria clasts collected from the 1975 inner crater rim are similar to the moderately vesicular clast analysed from Facies D, with only a few clasts from Facies A and B exhibiting very high vesicularities (>70%). Vesicle walls of both clasts are typically smooth and do not contain any cryptocrystalline growth.

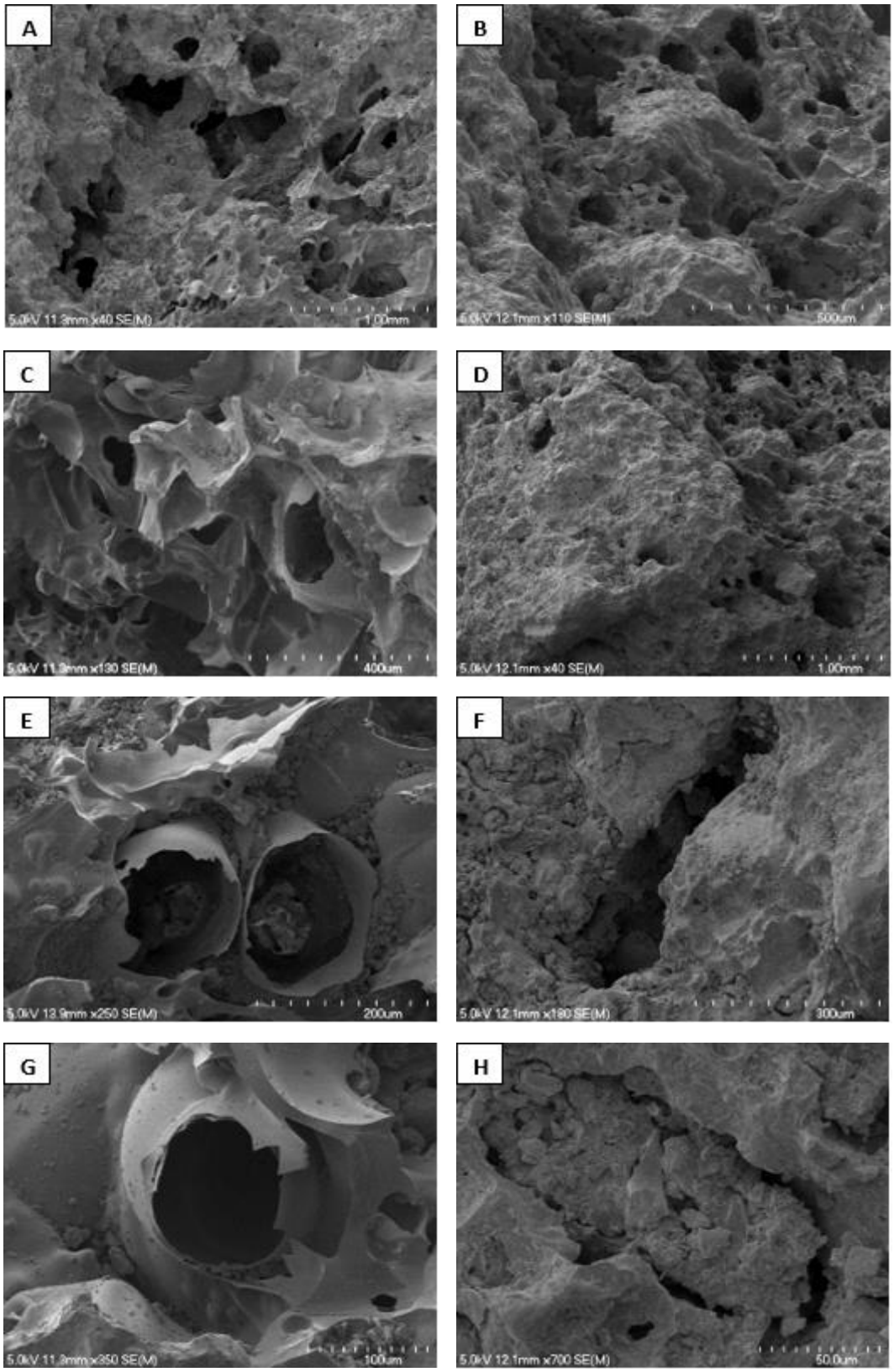

Figure 4.30 Secondary electron SEM images showing surface morphologies of a highly vesicular scoria clast (images on the left) and a moderately vesicular scoria clast (images on the right). A) Abundant irregular and isolated vesicles, B) sub-round to irregular vesicles, C) tightly packed/polygonal vesicles with thin vesicle walls, D) heterogenous vesicle distribution and thicker vesicle walls, E) delicate, thin-walled vesicles, F) elongate surface vesicle, G) vesicles existing within spherically intact bubble walls, and H) surface vesicle infilled with other material.

4.4 Quantitative Vesicularity

4.4.1 Methodology

4.4.1.1 Bulk vesicularity

Bulk vesicularity measurements were obtained following the methods by Houghton and Wilson (1989) (Appendix 6a). Clast samples from each facies were dried in the oven prior to recording the dry weights. Clasts were then wrapped firmly using Parafilm M®, and the number of 10 by 10 cm wax sheets used for each sample was recorded. The wet weight of each sample was measured in a beaker of water and recorded, in addition to the weight of a lead ballast that was used if required to keep the sample submerged.

All values were recorded in a spreadsheet that calculated the density and vesicularity of each clast, and the mean, standard deviation, and maximum and minimum vesicularities for each sample set. The dense rock equivalent (DRE) density value used in bulk vesicularity calculations was obtained by crushing three random samples from the 1975 deposit, determining the solid density of the powder using a pycnometer (see section 4.4.1.2), and then taking the average.

4.4.1.2 Pycnometer vesicularity

The UltraPycnometer 1000 Automatic Density Analyzer was used to measure the average solid density (i.e. excluding vesicles connected to the surface but including internal isolated vesicles) of 1954 and 1975 clasts, which were collected and cut into cylinders previously by H. Goddard (2010, unpublished University of Waikato data). There were two different cylinder sizes depending on the original sample size; some were approximately 2 cm in diameter and 2 cm in length, while others were approximately 3.7 cm and 3.4 cm respectively.

The pycnometer was calibrated at the start of each session and whenever a different sized sample holder was used following instructions in Quantachrome Instruments (2007). The gas used was oxygen-free nitrogen; the input gas pressure was set to a maximum of 20 psi (~2 psi above the desired target pressure), and the rate of pressurization in the sample cell was adjusted to be achieved in 30-60 seconds. This rate was re-checked when a different sample cell size was used.

Each sample was weighed prior to being analysed, and the weight was entered into the pycnometer to obtain an average volume and density from three consecutive runs. The proportion of isolated vesicles was calculated from the difference between the DRE density (see section 4.4.1.1) and the pycnometer density, and the connected vesicle proportion was subsequently calculated by subtracting the isolated vesicularity from the bulk vesicularity taken using the mass and cylinder volume of the cores (Appendix 6b). Any negative isolated vesicularities were corrected for by being assigned a zero, and the corresponding connected vesicularity was adjusted to match the bulk vesicularity of that sample.

4.4.2 Results

4.4.2.1 Bulk vesicularity

Facies A appears to have a higher proportion of dense clasts with <40% vesicularity than moderately vesicular clasts with vesicularities between 51-70% (Figure 4.31). There is also a higher proportion of very dense clasts (with only 1-10% vesicularity) in Facies A compared to the other facies which comprise the 1975 inner crater rim deposit (Figure 4.31). Facies A lacks clasts with vesicularities between 41-50% and has a small proportion of very light clasts which float in water (Figure 4.31 A). The two clasts that floated have vesicularities of 84% and 65%; quite high for a typical clast of basaltic andesite composition.

Facies B, C, and D are all bimodal in clast bulk vesicularity (Figure 4.31). Facies B has a clast mode at 11-20% and 61-70% vesicularity, with a lack of clasts containing vesicularities between 31-40% (Figure 4.31 B). One clast contains a very high vesicularity of 72%, and floats in water. Facies C also has two peaks in clast vesicularity, at 11-20% and 51-70%, with a lack of clasts containing 41-50% vesicles (Figure 4.31 C). In contrast, clasts from Facies D range from 1-70% vesicularity, with a peak of clasts containing 21-30% vesicles and another peak of clasts containing 51-60% vesicles (Figure 4.31 D). All sampling localities within facies D appear to have this bimodal trend in clast vesicularity, with the higher clast mode consistently at 51-60% (Appendix 6a). The lower modal peak is at 31-40% vesicularity for the lower sampling localities in Facies D but is slightly lower at 21-30% vesicularity for clasts collected from the uppermost sampling

locality (Appendix 6a).

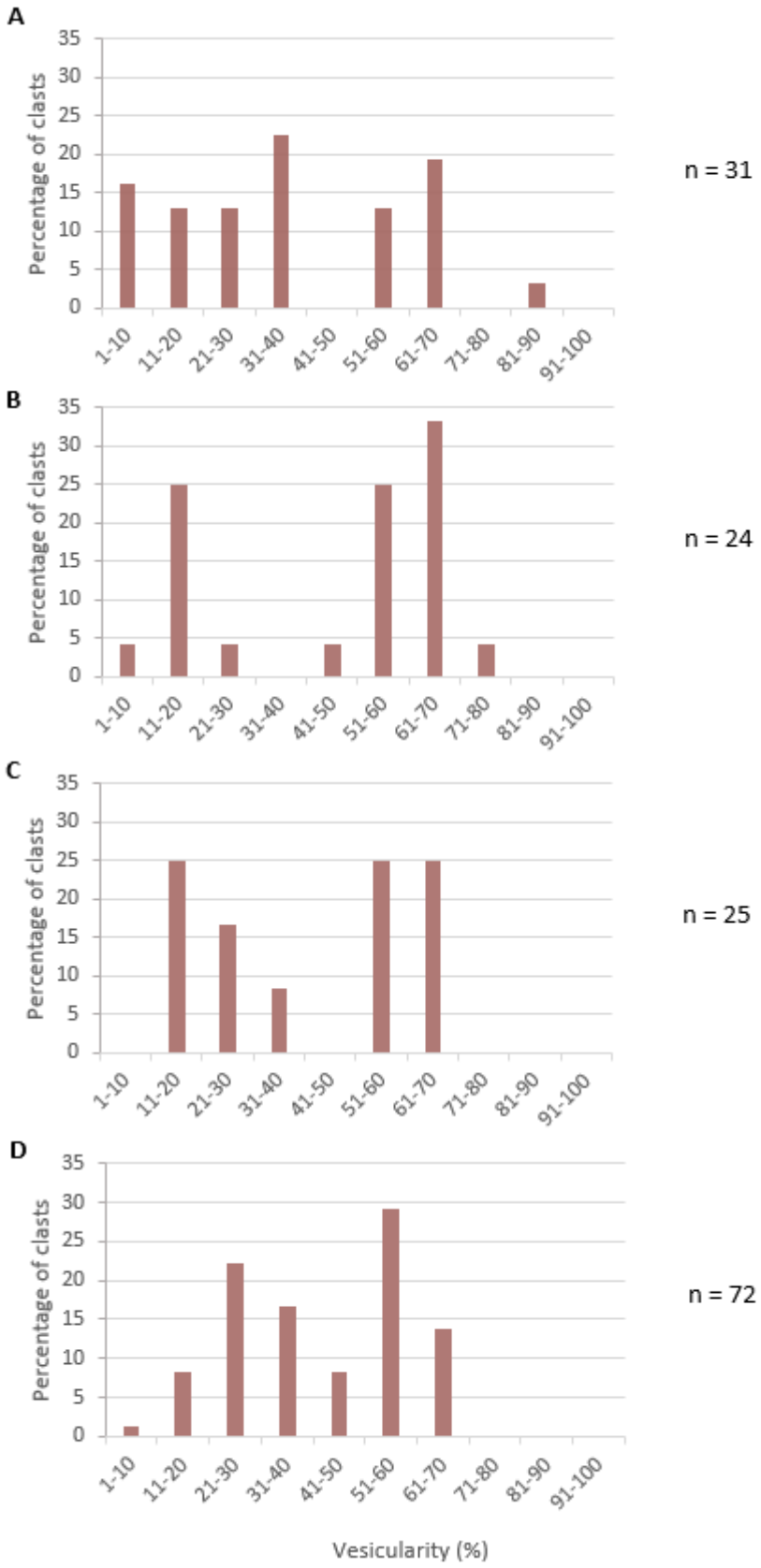

Figure 4.31 Bulk vesicularity results, obtained from the Houghton and Wilson (1989) wrapping method, for the various facies comprising the 1975 inner crater rim deposit. A) Facies A, B) facies B, C) facies C, and D) facies D (combined vesicularity results for the three different sampling localities within this facies; D1, D2 and D3). n = total number of clasts in the sample set.

Bulk vesicularity results for the 1975 clasts can also be compared against the bulk vesicularity results acquired for the 1954-55 clasts (H. Goddard and A. Pittari, 2010, University of Waikato, unpublished data), where both set of results were obtained from the Houghton and Wilson (1989) wrapping method. The 1954-55 clasts range in bulk vesicularity from 14-75%, while the 1975 clasts range from 6-84% (Appendix 6a). The 1954-55 clasts appear to have a unimodal distribution in bulk vesicularity, with ~42% of the samples containing 61-70% bulk vesicularity (although mostly the lower end of this range). Clast bulk vesicularities are negatively skewed, with clasts having as low as 11% vesicularity (Figure 4.32). In contrast, clasts from the 1975 eruption appear to have a more bimodal bulk vesicularity distribution with a peak at 21-30% vesicularity and another peak at 51-60% (Figure 4.32). A small proportion of clasts from both eruptions have an unusually high bulk vesicularity for typical basaltic andesite scoria (>65%). However, it is possible that the wrapping of highly irregular scoria clasts could also result in higher than expected vesicularities.

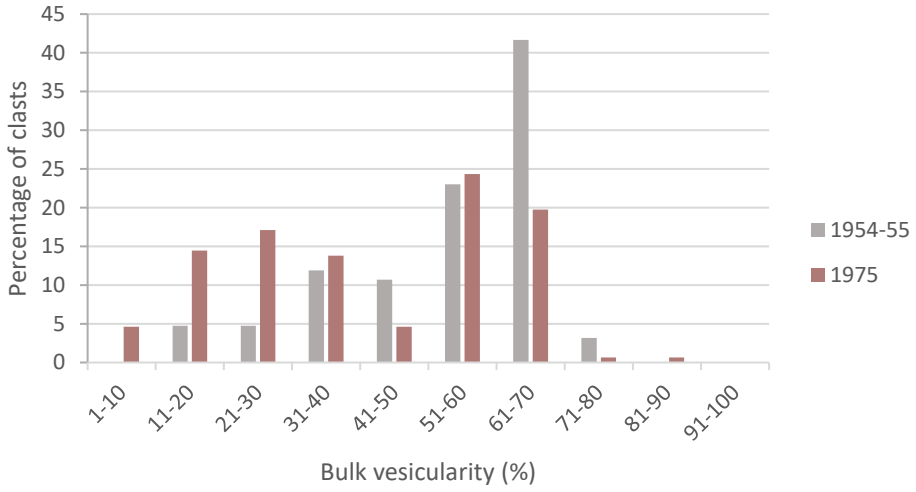

Figure 4.32 Bulk vesicularity results obtained from the Houghton and Wilson (1989) wrapping method for clasts from the 1954-55 and 1975 eruptions of Ngauruhoe. Note that the 1954-55 values are obtained from previous work (H. Goddard and A. Pittari, 2010, unpublished University of Waikato data). Refer to Appendix 6.

Bulk vesicularity values were also obtained from measurements related to the cylinder samples cut for the pycnometer (Appendix 6b). Bulk vesicularity was calculated in this manner for the 1954-55 and 1975 samples collected H. Goddard (2010, unpublished University of Waikato data), and also for some 1954-55 samples by Krippner (2009). The calculation used is as follows:

$$bulk\ vesicularity = \left(\frac{DRE\ density - bulk\ density}{DRE\ density}\right) \times 100,$$

where the DRE density is the average pycnometer density of three crushed basaltic andesite scoria clasts from the 1975 deposit, and the bulk density is calculated from the mass and bulk volume of each cylinder core.

The bulk vesicularity results obtained from the Houghton and Wilson (1989) wrapping method and the cylinder sample measurements show a similar distribution for both the 1954-55 clasts and the 1975 clasts (Figure 4.33). This is a good indication that the data represents the true variation of clast bulk vesicularity in both eruption deposits, particularly since the clasts used for the wrapping method were not the same clasts used for the cylinder calculation.

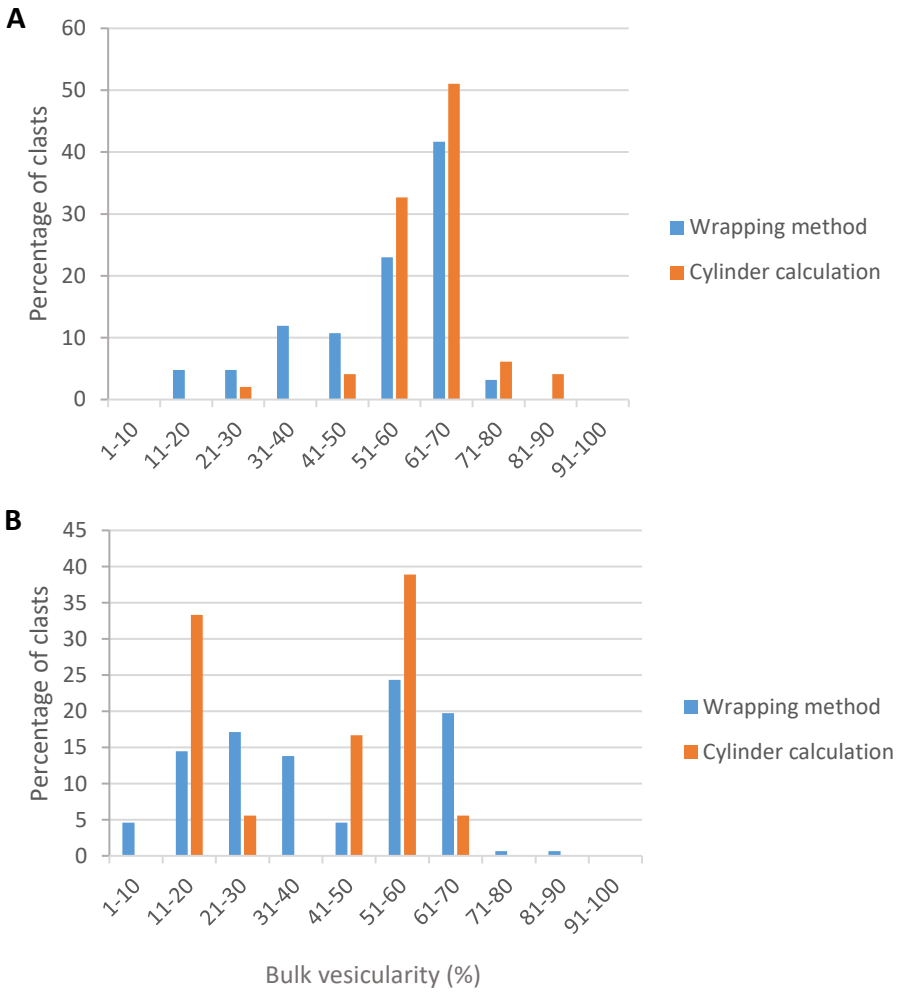

Figure 4.33 Distribution of clast bulk vesicularity calculated by the Houghton and Wilson (1989) wrapping method compared to those calculated with pycnometer cylinder measurements for A) 1954-55 samples, and B) 1975 samples.

4.4.2.2 Pycnometer vesicularity

Further clast vesicularity data is provided from pycnometer analyses of 1954-55 clasts collected by Krippner (2009), as well as 1954-55 and 1975 clasts collected by H. Goddard (2010, unpublished University of Waikato data). Results from pycnometer calculations suggest that most of the vesicles within both the 1954-55 and 1975 samples are connected to the outside of the clast, with only a small proportion of isolated vesicles (Figure 4.34). The 1954-55 samples have connected vesicle proportions ranging from 22-81% (although most samples have >45% connected vesicles), and isolated vesicle proportions <6.95% (Figure 4.34). In contrast, the 1975 samples have connected vesicle proportions ranging from 9-62%, and isolated vesicle proportions <3% (Appendix 6b). The 1975 samples appear to have two distinct clast groups; a dense group with 10-20% connected vesicles and <2% isolated vesicles, and a more vesicular group with 40-60% connected vesicles and only about 2-4% isolated (Figure 4.34).

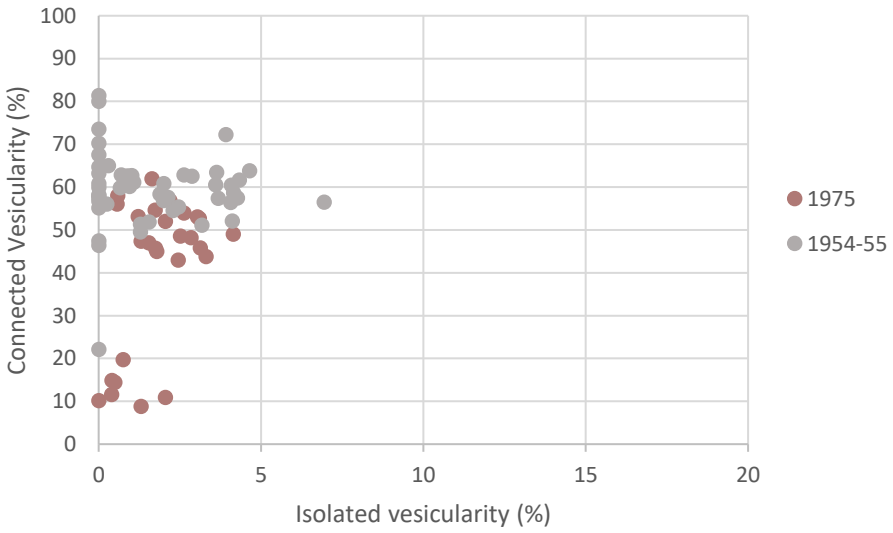

Figure 4.34 Percentage of isolated vesicles versus connected vesicles for clasts from the 1954-55 and 1975 eruptions, as calculated from pycnometer density data.

4.5 Componentry and Shape Analysis of Ash Samples

Changes in ash componentry and juvenile grain shapes from several eruptions between 1972 and 1975, may provide insight into eruption and fragmentation processes leading up to the explosive eruption on the 19th of February 1975. In particular, changes in the proportion of lithics and juvenile material could reveal when substantial vent clearing occurred, and when juvenile magma was first involved in the years prior to 1975. X-ray powder diffraction (XRD) analyses may provide additional information about changes in mineralogy through time, and identify any samples affected by hydrothermal alteration. Fragmentation mechanisms associated with eruptions between 1972 and 1975 may also be identified by shape analyses, with inter-comparability possible due to analysis of a consistent grainsize (Liu *et al.*, 2015).

4.5.1 Methodology

4.5.1.1 Preparation of ash samples

Ash samples for analysis were selected based on a large enough median grain size (>50 µm), and for a range of months from 1972-1975 (refer to Table 3.2). Bulk ash samples were used for XRD analyses, but samples were subsequently sieved to obtain a single grain-size fraction (3 phi; particles >125 µm but <250 µm) for stereomicroscopic analysis and shape analysis.

4.5.1.2 X-ray powder diffraction (XRD) analysis

Approximately 10 g of each bulk ash sample was crushed with an agate mortar and pestle into a fine powder. These were then added to sample holders and processed by the Panalytical Empyrean XRD in the Faculty of Science and Engineering, University of Waikato. The samples were run for 5-80 °2θ, at 50 seconds per step, and HighScore (powder diffraction software) was used to identify peaks in the resulting diffraction patterns.

4.5.1.3 Classification of ash grains

The 3-phi sieve fraction of each sample was delicately sprinkled on a glass slide and observed under a stereomicroscope to classify grain-types (crystal phases, black glassy grains, juvenile scoria grains, and lithics), describe physical

characteristics (morphology, vesicularity/density, and colour), and record differences in componentry between samples.

4.5.1.4 Image shape analysis of juvenile ash grains

The 3-phi fraction of ash samples were analysed under the stereomicroscope, and juvenile particles were separated from lithics and crystals. For each sample, the juvenile grains were spread out on a glass slide (using a metal rod under the stereomicroscope) to avoid particle contact. The grains were subsequently picked up by double-sided sticky tape applied to the base of an epoxy block mould. Each base was then fixed together with the top part of the mould and filled with approximately 1 cm of resin and harder at a ratio of 2:1 (Figure 4.35). These were left on a hot plate at ~50 °C overnight, and once completely set, the epoxy blocks were removed from their moulds and polished.

Backscattered electron SEM images of each sample were taken at a consistent magnification, and shape analyses were attained following methods by Liu *et al.* (2015). Each image was thresholded to binary, and then filtered (to minimise non-natural grain complexity introduced during thresholding) by the removal of one-pixel outliers, followed by pixel dilation and erosion. The shape analysis macro for ImageJ supplied in the online supplementary material (Liu *et al.*, 2015) was applied to each image to obtain solidity and convexity data (Appendix 7). Any grain shapes affected by bubbles in the resin were ignored, and anywhere between 60-140 grains were analysed in each ash sample.

Figure 4.35 Epoxy block moulds with juvenile material spread out on the base (lined with double-sided sticky tape) and filled with approximately 1 cm of resin/hardener.

4.5.2 Ash Analysis Results

4.5.2.1 Stereomicroscope analysis of ash samples

Noticeable differences in grain-type proportions were analysed between several 1972-1975 eruptions. The ash sample from the 24th of March 1972 eruption was particularly distinct from the others, with hydrothermally altered lithics being the most abundant component (Figure 4.36). These are predominantly sub-angular, irregularly shaped, pale grains which appear to be composed of a quartz-rich matrix. There are also less common sub-rounded to sub-angular, dull, grey lithics. The 26th of October 1973 ash sample contains a slightly higher proportion of lithics than the following eruptions, but still significantly less than the 1972 ash sample (Figure 4.36).

In contrast, all of the ash samples from eruptions following 1972 are predominantly composed of glassy grains. The 1972 ash sample only contains a minor amount of dense black vitreous grains, while the other eruptions contain a significant proportion of black glassy grains (in addition to some reddish-brown coloured scoria) (Figure 4.36). Volcanic ash from the 17th of February 1975 eruption contains a noticeably higher abundance of reddish-brown scoria compared to the other eruptions, and these grains are discernibly more vesicular and irregular in morphology (Figure 4.36).

Three main crystal phases were observed in each of the ash samples, including plagioclase (white translucent grains), pyroxene (shiny black euhedral grains), and olivine (greenish-yellow translucent grains). Transparent quartz crystals sourced from xenoliths and lithics were also present. The overall proportion of crystals varies throughout the eruptions, with a low abundance in the 1972 ash sample relative to subsequent eruptions (particularly the eruptions of 1974 and 1975) (Figure 4.36).


A
Hydrothermally altered lithics
Quartz
Black, glassy grains
Dull lithic
400 µm

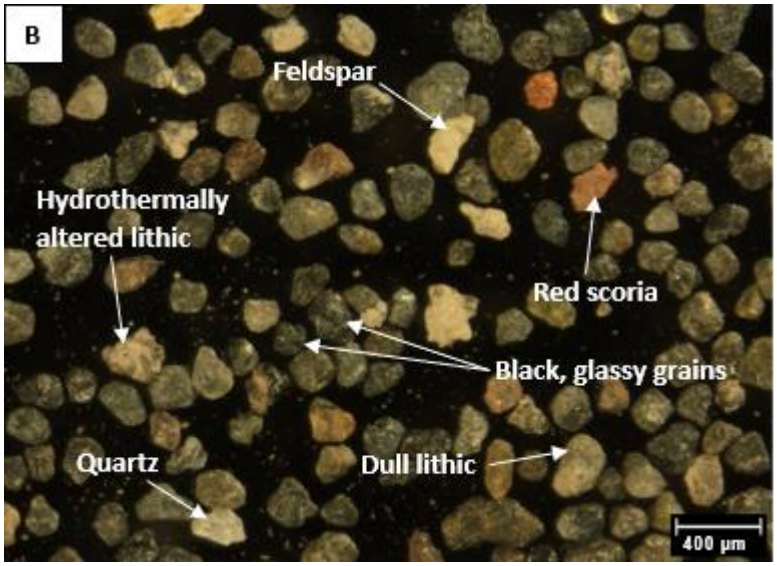
B
Feldspar
Hydrothermally altered lithic
Red scoria
Black, glassy grains
Quartz
Dull lithic
400 µm

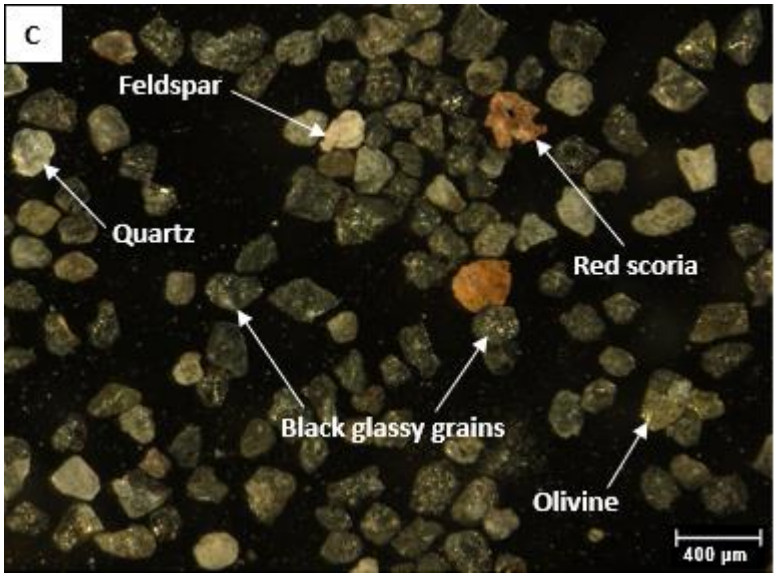
C
Feldspar
Quartz
Red scoria
Black glassy grains
Olivine
400 µm

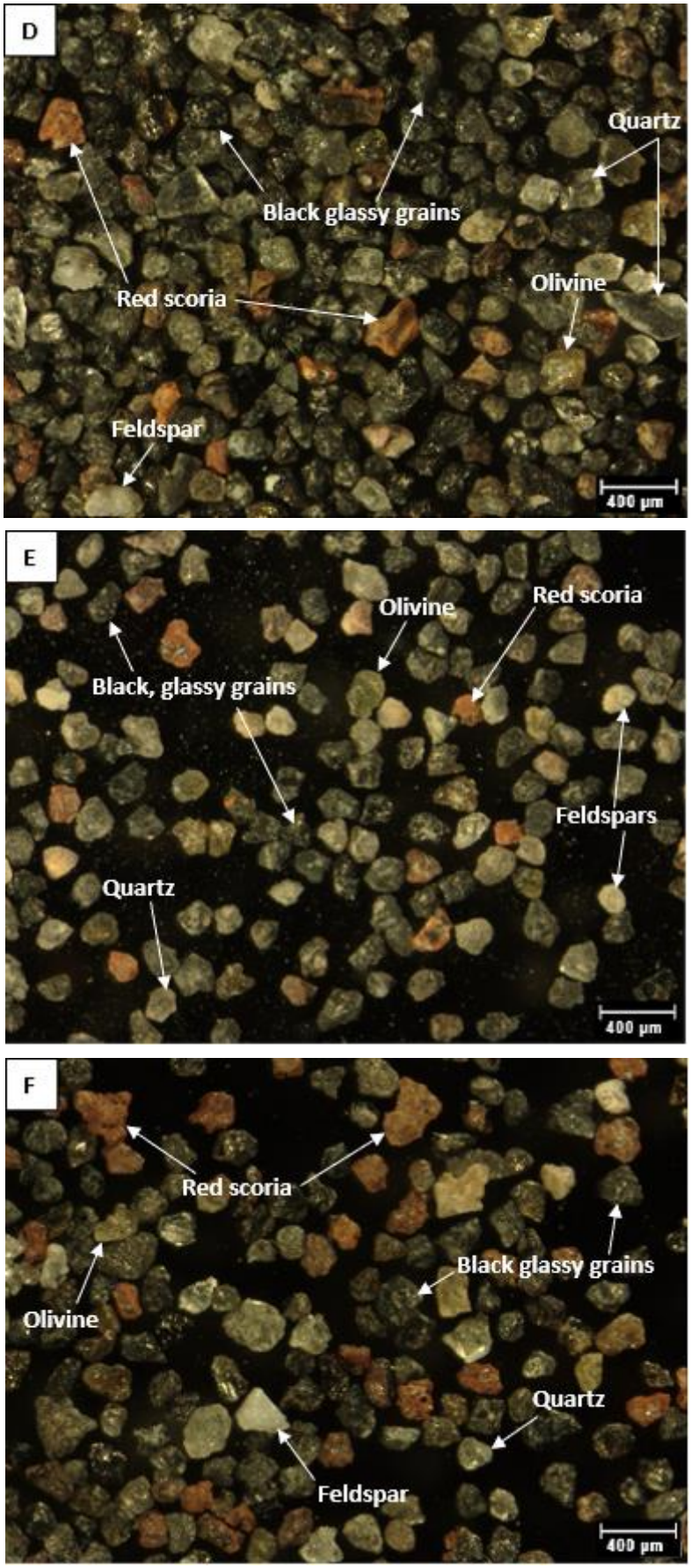

Figure 4.36 Stereomicroscope photomicrographs of ash samples from several Ngauruhoe eruptions between 1972 and 1975, including A) 24/03/72, B) 26/10/73, C) 7/12/73, D) 24/01/74, E) 28/03/74, and F) 17/02/75. Note that pyroxenes, although difficult to distinguish in these photomicrographs, were also observed in the 1972-1975 ash samples.

4.5.2.2 X-ray powder diffraction (XRD) analysis

XRD analyses (Appendix 8) indicate that all ash samples from eruptions between 1972 and 1975 contain primary volcanic minerals including plagioclase feldspars and clinopyroxenes (predominately augite and potentially some pigeonite). Orthopyroxene (enstatite) peaks were also identified in most ash samples following and including the sample from the 7th of December 1973 eruption. These minerals identified by XRD analyses were also observed in the ash samples under the stereomicroscope, and petrographically in the 1954/55 (Krippner, 2009) and 1975 clasts. A key difference between the ash samples is the presence of cristobalite in Ng2 (ash produced from the 24th of March 1972 eruption), which was not identified by XRD in any of the other ash samples (Appendix 8).

4.5.2.3 Ash shape analysis

The shape analysis macro for ImageJ provided by Liu *et al.* (2015) deduces two key parameters of interest; solidity and convexity. Solidity, or morphological roughness, compares the area of a convex hull (Figure 4.37) to the area of a juvenile grain. In contrast, convexity (or textural/surface roughness) compares the perimeter of a convex hull to that of a juvenile grain. Small scale irregularities/convexities on the grain surface thus greatly affect convexity values (Liu *et al.*, 2015). Variations in these parameters can distinguish between different juvenile components (Figure 4.38).

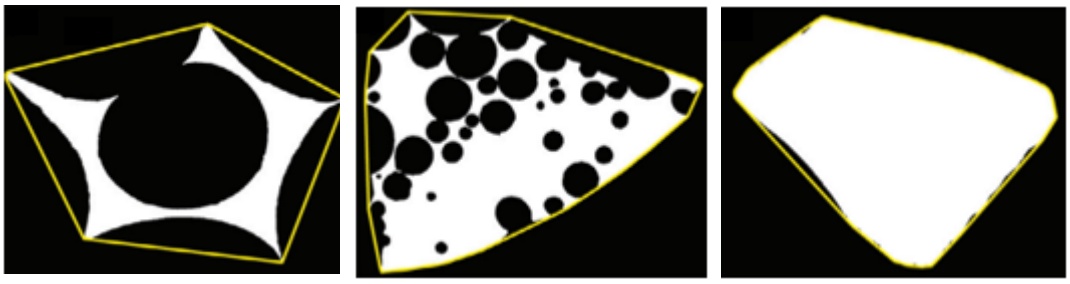

Figure 4.37 Yellow line illustrates a bounding reference shape (convex hull); an important factor in determining the solidity and convexity of juvenile ash grains (Liu *et al.*, 2015).

Ash sample Ng2 (from the 24/03/72 eruption) and sample Ng12A (from the 26/10/73 eruption) predominately consist of glassy dense grains with high convexity and solidity values (Figures 4.39 and 4.40). In contrast, samples from later eruptions (including ash from the 17th of February 1975) have a significantly wider spread in solidity and convexity, with both dense and vesicular glassy grains (Figures 4.39 and 4.41).

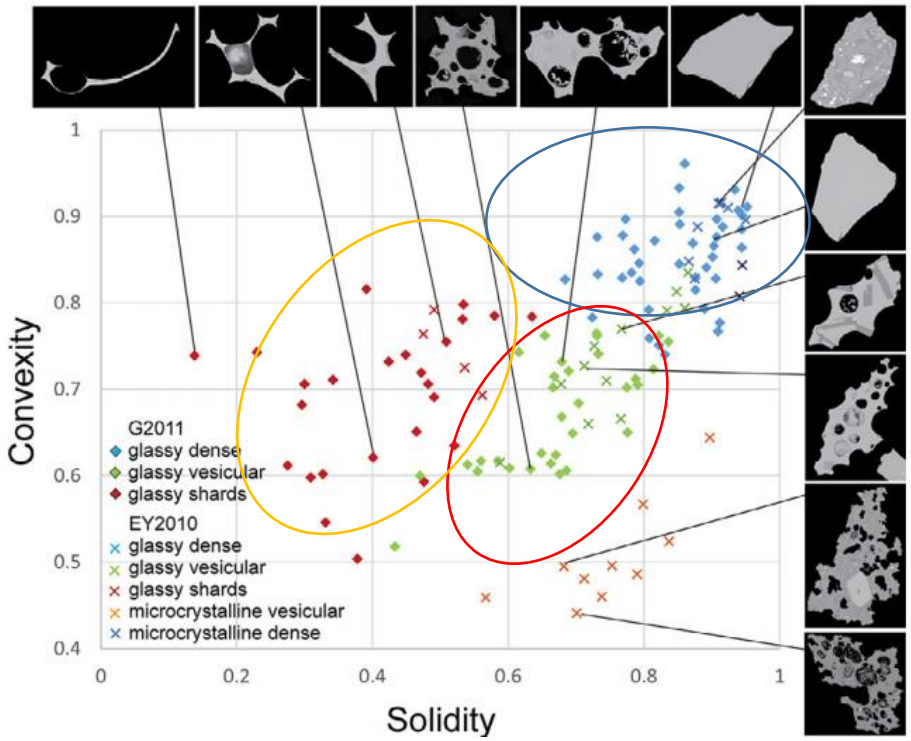

Figure 4.38 Modified from Liu *et al.* (2015), illustrating how solidity and convexity can provide information about the morphology of glassy grains. Note that glassy dense grains typically plot at high solidity and convexity values, while glassy vesicular grains typically plot at lower convexity and solidity values.

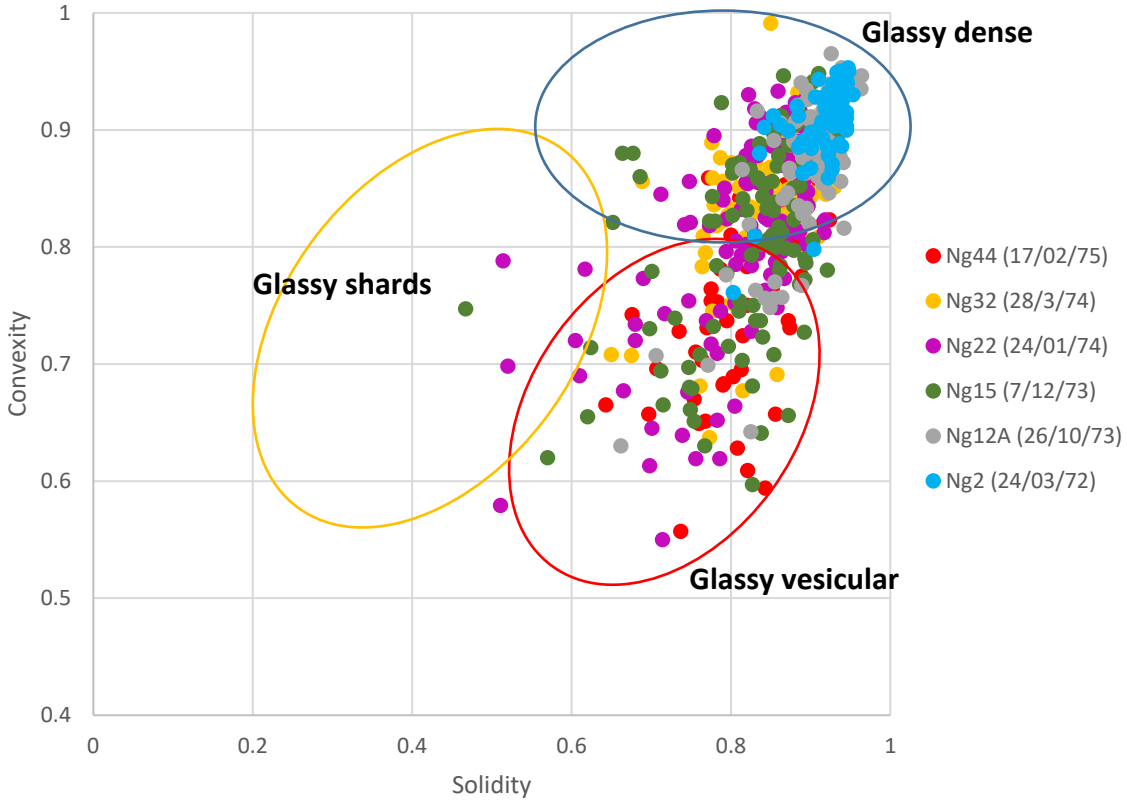

Figure 4.39 Shape analyses (solidity vs. convexity) of glassy grains from several Ngauruhoe eruptions between 1972 and 1975. Note that the envelopes classifying the range of convexity and solidity for glassy dense grains, glassy vesicular grains, and glassy shards are derived from Liu *et al.* (2015), as depicted in Figure 4.38.

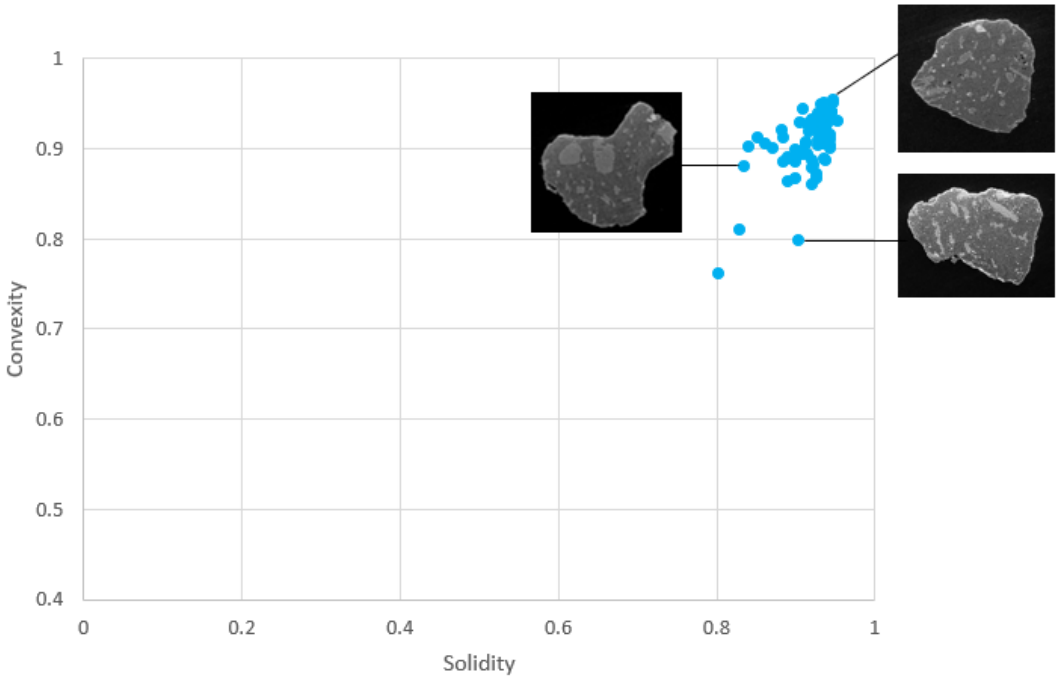

Figure 4.40 Shape analysis results for juvenile ash grains from sample Ng2 (24/03/72 Ngauruhoe eruption). Notice how the grains are predominantly plotting at high convexity and solidity values (typically >0.8 for both values).

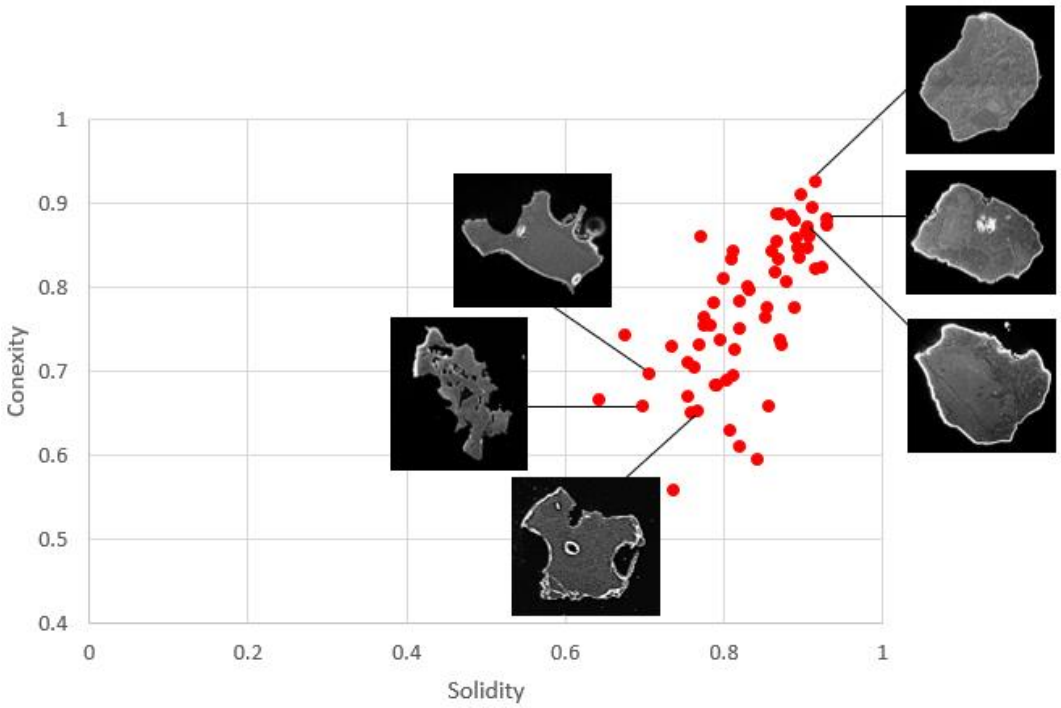

Figure 4.41 Shape analysis results for juvenile ash grains from sample Ng44 (17/02/75 Ngauruhoe eruption). Notice the wider spread in convexity and solidity compared to ash from the 1972 eruption (Figure 4.40).

4.6 Summary of Key Findings

The main findings from this chapter are summarised below.

- The mineralogy of clasts erupted during the 1975 eruption of Ngauruhoe includes plagioclase, orthopyroxene, clinopyroxene, olivine, and Fe-Ti oxides (predominantly magnetite).

- Plagioclase crystals commonly display resorption textures such as sieve textures and embayments. Cavities and embayments are also present in a few orthopyroxene and clinopyroxene phenocrysts, and typically in larger crystals.

- Oscillatory zoning is a common feature of plagioclase phenocrysts. Zoning is also common in pyroxene (particularly clinopyroxene) phenocrysts.

- Some olivine phenocrysts are rimmed by orthopyroxene.

- Plagioclase is often overgrown by magnetite.

- The 1975 clasts also contain a mixture of quartzofeldspathic, feldspathic, and quartzite xenoliths.

- The groundmass of red scoria clasts typically has an opaque tachylyte appearance, whereas the groundmass of black scoria clasts is generally brown with minor opaque areas due to a lesser degree of oxidation. Scoria clasts contain crystallites which are randomly orientated within the groundmass glass, giving it a hyalopilitic texture. The black scoria clasts contain a greater proportion of crystal free glass compared to the red scoria.

- The groundmass of dense clasts is typically more crystalline compared to the scoria clasts.

- The 1975 inner crater rim deposit has two distinct clast types in terms of vesicularity; dense clasts with modal vesicle abundances of less than 18%, and moderately vesicular scoria clasts with modal vesicle abundances ranging from 34-58%.

- All facies comprising the 1975 inner crater rim deposit are bimodal in clast vesicularities, containing a mixture of both dense clasts and moderately vesicular scoria. However, facies A contains a higher proportion of dense clasts compared to the overlying facies.

- A few scoria clasts from facies A and B have very high vesicularities (72% and 84%). These clasts have different surface morphologies compared to the moderately vesicular clasts; displaying tightly packed/polygonal vesicles with thin vesicle walls.

- Clasts are comprised predominantly of connected vesicles and only a minor proportion of isolated vesicles. Pycnometer calculations depict a dense group with 10-20% connected vesicles and <2% isolated vesicles, and a more vesicular group with 40-60% connected vesicles and only about 2-4% isolated vesicles. Additional evidence for bubble coalescence includes the irregular and elongate vesicle morphologies analysed in thin section.

- Ash produced during the eruption on the 24th of March 1972 is quite distinct from the eruptions that followed. The 1972 ash is primarily composed of hydrothermally altered lithics and contains a minor amount of dense black vitreous grains. Cristobalite was identified in the 1972 ash but not in any other samples (via XRD), and shape analyses depict the glassy dense nature of the 1972 grains.

- The eruptions following 1972 contain a significant proportion of black glassy grains, in addition to some reddish-brown coloured scoria. The 1975 eruption, in particular, contains grains with a wide range in solidity and convexity (i.e. a mixture of dense glassy grains and glassy vesicular grains).

Chapter Five

Glass / Mineral Chemistry

5.1 Introduction

This chapter provides detailed mineral and glass chemistry data for both the 1975 inner crater rim samples and the 1954-1975 distal ash samples, obtained from the electron probe micro-analyzer (EPMA). Precise, quantitative elemental analyses of crystal cores and rims are presented for the different mineral phases observed in the Ngauruhoe eruption deposits. Core to rim analyses of zoned phenocrysts provide information regarding changes in magma chemistry during the growth of the crystal, while rim analyses specifically offer insight into the final stage magma composition involved in the 1975 eruption.

Compositional comparisons between the 1975 groundmass glass and phenocryst-hosted melt inclusions can be used to assess the genetic relationship between crystals and their host liquid. Glass chemistry data obtained from samples ejected from eruptions leading up to and including the climactic 19th February 1975 eruption have also been compared, in order to identify any changes through time and any similarities/differences between eruptions. Trends identified between various major elements can be used to examine the evolution of the magma from its storage region to eruption. This chapter uses these data to explore the extent of fractional crystallisation and uses experimentally determined phase diagrams to assess magmatic processes.

5.2 Methodology

5.2.1 Preparation for the Electron Microprobe

5.2.1.1 Grain mount preparation

Grain mounts were made of crystals from some black scoria clasts from facies B of the 1975 inner crater rim deposit (since these clasts were the least oxidised and therefore the best for probing glass surrounding the crystals), and also a selection of ash samples produced from several eruptions between 1954 and 1975 (including 1954, 18th August 1968, March 1972, March 1974, 11th-12th February

1975, and 19th February 1975). A few of the 1975 black scoria clasts were lightly crushed with a mortar and pestle so that pyroxene, olivine, and plagioclase crystals could be picked out under the stereomicroscope (the aim being to increase the likelihood of finding melt inclusions under the SEM).

A square of double-sided sticky tape was applied to the middle of several glass slides and an epoxy block was attached to each. The pre-made epoxy blocks (~8 mm in height, 25 mm in diameter, and consisting of seven holes) were washed and dried prior to use. For the ash grain mounts, the blocks were labelled with sample numbers and each sample was added into two holes, while the remaining holes were covered with tape to avoid cross contamination. For the 1975 crystal grain mounts, crystals were carefully placed into the holes with tweezers.

A single drop of resin was added to each hole and the ash samples were lightly stirred to ensure the grains covered the surface of the mount. The epoxy blocks were left to set on a hotplate at ~50 °C overnight. Ethanol and a sharp blade were later used to separate blocks from the glass slides/sticky tape, and each block was subsequently ground using grit-500 followed by grit-1200 silicon carbide grinding paper, and polished to expose grains at the surface.

5.2.1.2 Microprobe target maps

Following the preparation of epoxy grain mounts and polished thin sections (section 4.3.1.1), both optical microscopy and scanning electron microscopy were used to identify minerals, zoning, melt inclusions, and areas of groundmass glass suitable for EPMA analysis. Microprobe target maps were created by scanning the thin sections and grain mounts, printing them on A3-sized paper, and marking out the locations of interest.

5.2.2 Electron Microprobe Analysis (EPMA)

The major element chemistry of mineral phases and glass (groundmass glass and melt inclusions) were analysed using the JEOL JXA-8230 SuperProbe at the School of Geography, Environment and Earth Sciences at Victoria University, Wellington. Polished thin sections and epoxy grain mounts were carbon coated prior to EPMA.

The microprobe was programmed specifically for mineral and glass analysis. For mineral analysis, beam conditions were set at an accelerating voltage of 15 kV, a current of 12 nA, peak/background count times of 30s/15s respectively, and the focussed beam had a spot diameter of 1 µm. The minerals were standardised against plagioclase (NMNH 115900), Kakanui augite (USNM 122142), Springwater olivine (USNM 2566) and synthetic oxides (Jarosewich *et al.*, 1980). Groundmass glass analyses used a 15 kV voltage, reduced current of 8 nA, and peak/background count times of 30s/15s respectively (except Na which was measured first for 10s/5s with no peak search). A defocused 5 µm beam was used to reduce the effect of alkali loss, but still small enough in diameter to target melt inclusions and avoid groundmass microlites. Glass was standardised against natural glasses of rhyolite (VG-568, USNM 72854) and basalt (VGA-99, USNM 113498/1) composition, and synthetic oxides (Jarosewich *et al.*, 1980).

At least three analyses of appropriate mineral or glass standards were carried out every 20-30 analyses to monitor spectrometer drift and ensure a high level of accuracy. The full set of microprobe data is presented in Appendix 9 and contains data from repeated analysis of the standards during the probe work period.

Analyses were obtained for three representative thin sections, including two juvenile scoria clasts (Bv1 and Bv2) and one dense clast (Cd3) from the 1975 inner crater rim deposit. Crystal cores and rims of each of the crystal phases (plagioclase, clinopyroxene, orthopyroxene, and olivine) were targeted in each thin section. Melt inclusions (mostly pyroxene-hosted) were also probed in each thin section, in addition to groundmass glass in the two juvenile scoria samples. Every effort was made to probe fresh glass and avoid the abundant groundmass microlites.

Melt inclusions and groundmass glass were also targeted in the epoxy grain mounts containing previously hand-picked crystals from the crushed 1975 scoria clasts. The epoxy mounts containing the 1954-1975 ash samples were probed at random due to difficulties distinguishing between crystals and glass fragments. This data was later analysed to identify which fragments had geochemical data representative of glass versus crystals.

5.2.3 Microprobe Data Cleansing

For these samples (which are associated with anhydrous/water-poor magma), any microprobe points with elemental totals of less than 98% were identified and excluded from further analyses. However, it is important to note that this method would not be applicable to volcanoes with water-rich magmas (e.g. Indonesian volcanoes) which often have low elemental totals of ~94% (Vigouroux *et al.*, 2012; Geoff Kilgour, personal communication, 2019). The data was then rearranged and normalised so that the sum of elements probed for each point equated to 100%. Upon further examination of the data, notes were made if the elemental proportions suggested a different component than what was thought to have been targeted (Appendix 9).

5.2.4 Geothermometry Methods

The estimation of magmatic temperature conditions associated with the 1975 Ngauruhoe eruption was calculated using the clinopyroxene-liquid geothermometer workbook downloaded from Putirka (2016) (Appendix 10), since it applies to rocks which have water contents between 0-10 wt. %, and which equilibrate at temperatures between 700-1700 °C and pressures of 1 bar-70 kbar (Putirka, 2008). Normalised rim composition data for clinopyroxene (cpx) phenocrysts probed in the 1975 clasts were entered into this workbook. Each cpx rim was paired with three different groundmass glass compositions (including the most mafic, most silicic, and average) to determine which cpx-liquid pair was closest to equilibrium. A nominal value of 0.6 wt. % H_2O (Lormand *et al.*, n.d.) and an average value of 0.2 wt. % P_2O_5 (Kilgour, 2013) was entered for glass.

5.3 Mineral EPMA Results

5.3.1 Plagioclase

The feldspar series includes the sodium endmember; albite (Ab), the potassium endmember; orthoclase (Or), and the calcium endmember; anorthite (An). Plagioclase phenocrysts from the 1975 Ngauruhoe eruption range from labradorite to bytownite (An_{59-90}) (Table 5.1; Figure 5.1). Similar results (An_{53-87}) were also obtained for the 1954-75 clasts analysed by Krippner (2009). There does

not appear to be any clear differences in plagioclase composition between clast types (i.e. dense versus vesicular clasts) from the 1975 inner crater rim deposit (Figure 5.1).

Plagioclase cores appear to have a greater range in compositions (An_{62-90}) compared to the rims (An_{59-71}), with core compositions extending to higher An contents (Table 5.1; Figure 5.2). Normal zoning is common in zoned plagioclase phenocrysts, with crystal cores typically containing higher anorthite contents compared to the rims (Table 5.1; Figure 5.2). However, it is important to note that this is not always the case as one of the plagioclase crystals probed displays reverse zoning with a higher anorthite content in the rim (An_{75}) compared to the core (An_{70}) (Figure 5.2). Probe data also suggests that across a crystal, there can be variations in composition, i.e., a simple one-way solid solution pattern is not always the case (Table 5.1; Figure 5.2).

Table 5.1 Endmember proportions calculated for cores and rims and intermediate zones of plagioclase phenocrysts from the 1975 inner crater rim deposit of Ngauruhoe (calculations based on normalised microprobe data). Feldspar endmembers include anorthite (An), albite (Ab), and orthoclase (Or).

Spot[1]	An	Ab	Or
Bv1_plagb_core	62.53	36.13	1.34
Bv1_plagb_zone1	81.71	17.83	0.46
Bv1_plagb_zone2	62.31	36.64	1.05
Bv1_plagb_rim	60.45	37.85	1.70
Bv1_plagc_core	67.16	31.67	1.17
Bv1_plagc_rim	59.01	39.22	1.77
Bv1_plagd_core	89.46	10.45	0.09
Bv1_plagd_rim	71.36	27.98	0.67
Bv1_plage_core	90.39	9.45	0.16
Bv1_plage_rim	70.37	28.87	0.76
Bv2_plaga_core	69.82	29.13	1.06
Bv2_plaga_rim	74.87	24.47	0.66
Bv2_plag4_core	68.51	30.34	1.15
Bv2_plag4_rim	65.54	33.17	1.29
Cd3_plag1_core	75.95	23.04	1.01
Cd3_plag1_zone1	87.33	12.37	0.30
Cd3_plag1_rim	63.90	34.78	1.32
Cd3_plag3_core	88.20	11.49	0.31
Cd3_plag3_rim2	69.85	28.92	1.23
Cd3_plag4_core	81.77	17.71	0.52
Cd3_plag4_zone1	66.88	31.91	1.21
Cd3_plag4_zone2	80.61	18.88	0.52
Cd3_plag4_rim	61.77	36.41	1.82

[1]Filename nomenclature for each probe spot begins with a thin section reference, including the facies from which the clast was derived from (e.g. B or C), clast type (d = dense, v = vesicular), and the clast number (e.g. 1 = first clast, 2= second clast). Second part of file nomenclature is the crystal reference used for probe work (e.g. plag1 = plagioclase crystal 1), and final part of file nomenclature is the probe location (e.g. core, rim, or intermediate zone).

Barton (2011) carried out microprobe analyses on plagioclase crystals from historical Ngauruhoe lava flows and block-and-ash flows (from eruptions in 1870, 1949, 1954, and 1974-75). Plagioclase crystals were found to have compositions ranging from labradorite to anorthite (An_{51-92}), with cores typically containing higher anorthite (Ca) contents than the rims. Barton (2011) also noted the presence of complex zoning patterns and sodic cores in some plagioclase crystals, consistent with microprobe analyses in this study.

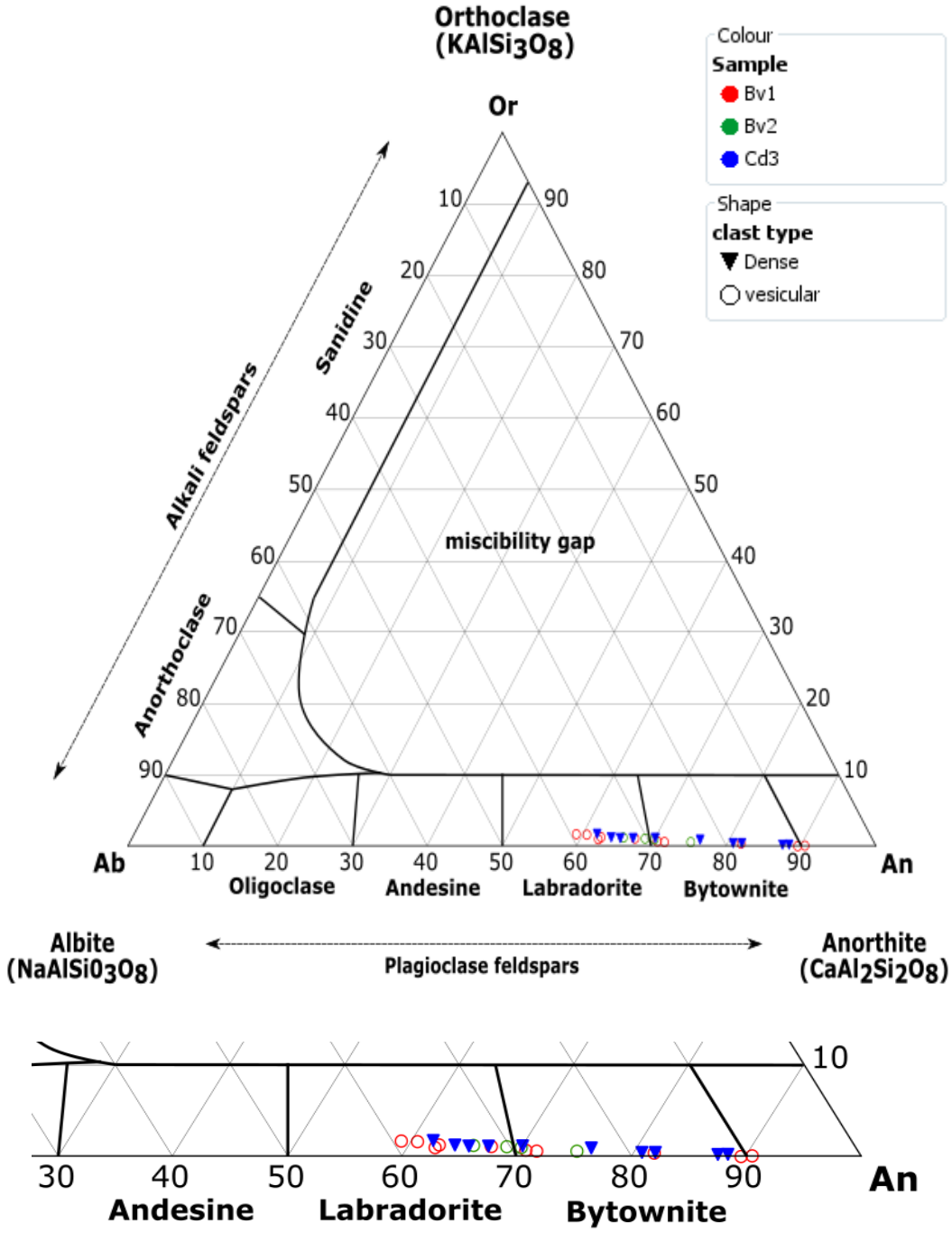

Figure 5.1 Ternary diagram for plagioclase compositions in dense and vesicular clasts from the 1975 eruption of Ngauruhoe. Note that the bottom figure is an enlarged extract of data from the above ternary diagram.

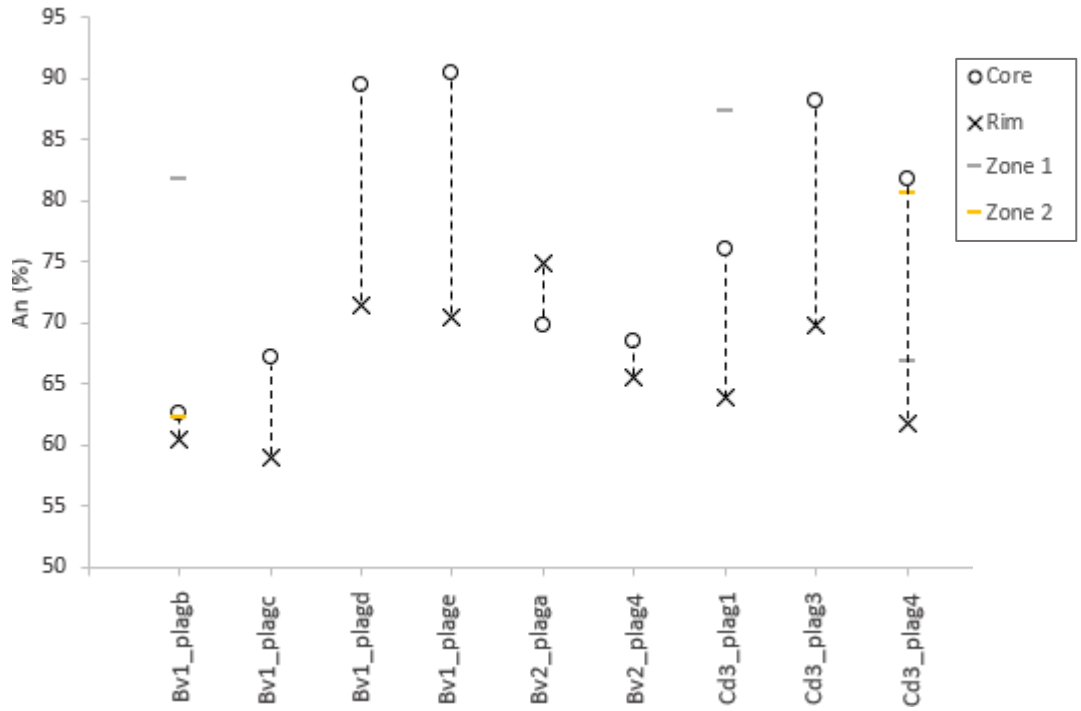

Figure 5.2 Graphical representation of the compositional variability within single plagioclase crystals (core and rim) using their anorthite contents, in various clasts from the 1975 eruption of Ngauruhoe. Anorthite compositions of intermediate zones are also displayed. Note that the x-axis represents the thin section (e.g. Bv1) and crystal analysed (e.g. plagb).

Figure 5.3 plots the composition of plagioclase crystals from the 1975 clasts in addition to any plagioclase crystals that were accidentally probed in the 1954-1975 ash samples. Although the EPMA was set for glass when analysing the ash samples (i.e. a lower current of 8 nA and a focused beam, as opposed to 12 nA and a defocussed beam used for crystals), the plagioclase spots still have good totals (100% ± ~0.3%) so it is reasonable to assume they are giving a good indication of the plagioclase composition. The plagioclase crystals from all eruptions generally have compositions ranging from labradorite to bytownite, although a few crystals fall in the andesine composition range (Figure 5.3). All plagioclase crystals from the 1975 eruptions contain >An_{60}, while plagioclase from earlier Ngauruhoe eruptions (including 1968, 1972, and 1974) have a greater range in compositions, extending as low as An_{48} (Figure 5.3).

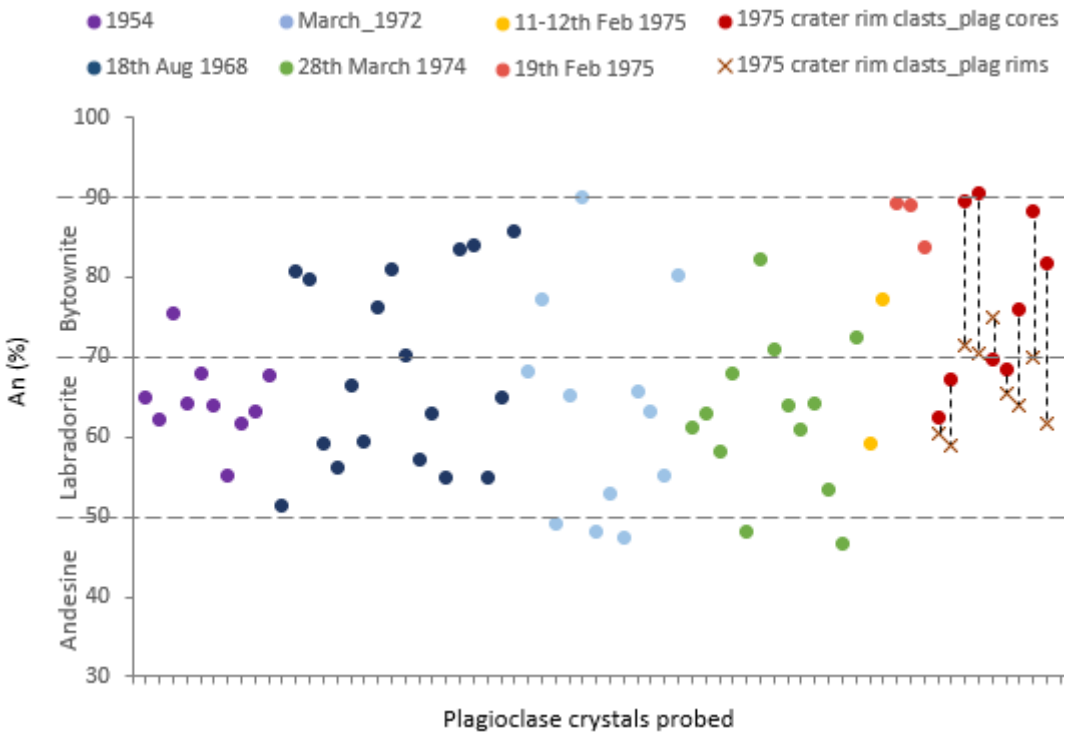

Figure 5.3 Anorthite contents of plagioclase feldspars probed in the 1954-1975 ash samples, in addition to those probed in the 1975 inner crater rim deposit. Tie lines are displayed only for plagioclase crystals in the 1975 crater rim clasts, for which the cores and rims were analysed. The crystal position (core versus rim) probed was not recorded for the ash samples as these were unintentionally analysed whilst probing glass, however they are most likely rim compositions. Note that the x-axis represents individual crystals probed (i.e. 1 through to 67).

5.3.2 Pyroxenes

The pyroxene silicate mineral series includes the calcium endmember; wollastonite (Wo), the iron endmember; ferrosilite (Fs), and the magnesium endmember; enstatite (En). Pyroxene compositions form two distinct clusters on the ternary diagram (Figure 5.4), with clinopyroxene compositions ranging from $Wo_{36}En_{39}Fs_{12}$ to $Wo_{42}En_{50}Fs_{24}$, and clinoenstatite (orthopyroxene) compositions ranging from $Wo_{3}En_{49}Fs_{25}$ to $Wo_{10}En_{72}Fs_{44}$. Orthopyroxene rims have a larger spread in compositions (cores range from $En_{62\text{-}72}$, while rims range from $En_{49\text{-}70}$) and tend to be more ferrosilite (Fe-rich) compared to the cores which are correspondingly higher in enstatite (Table 5.2; Figure 5.4). Clinopyroxene crystals appear to have a more similar spread between core and rim compositions (cpx cores range from $En_{42\text{-}50}$, while cpx rims range from $En_{39\text{-}45}$), although rims are also often higher in ferrosilite compared to the cores (Table 5.3; Figure 5.4).

Table 5.2 Endmember proportions calculated for cores and rims of orthopyroxene phenocrysts from the 1975 inner crater rim deposit of Ngauruhoe (calculations based on normalised microprobe data). Pyroxene endmembers include wollastonite (Wo), ferrosilite (Fs), and enstatite (En).

Spot[1]	Wo	Fs	En
Bv1_opx6_core01	3.76	24.69	71.54
Bv1_opx6_rim01	3.82	26.60	69.58
Bv2_opx2_core01	4.46	28.06	67.48
Bv2_opx2_rim01	3.92	35.94	60.14
Bv2_opx3_core01	3.95	28.69	67.36
Bv2_opx3_rim01	5.98	34.92	59.10
Bv2_opx3_rim02	3.26	29.89	66.85
Cd3_opx2_core01	4.18	32.58	63.24
Cd3_opx2_rim01	10.40	40.43	49.18
Cd3_opx3_core01	3.51	34.11	62.38
Cd3_opx3_rim01	4.29	25.72	69.99
Cd3_opx3_rim02	3.91	44.17	51.92
Cd3_opx5_core01	3.34	31.81	64.84
Cd3_opx5_rim01	9.61	35.48	54.91
Cd3_opx5(crystalbelow)_core01	3.85	32.50	63.65
Cd3_opx5(crystalbelow)_rim01	8.27	40.52	51.21

[1] Filename nomenclature for each probe spot begins with a thin section reference, including the facies from which the clast was derived from (e.g. B or C), clast type (d = dense, v = vesicular), and the clast number (e.g. 1 = first clast, 2= second clast). Second part of file nomenclature is the crystal reference used for probe work (e.g. opx6 = orthopyroxene 6), and final part of file nomenclature is the probe location (e.g. core, rim, or intermediate zone).

These results are similar to EPMA analyses conducted by Barton (2011) on pyroxene crystals from the historical Ngauruhoe lava flows and block-and-ash flows. Barton (2011) found clinopyroxene crystals from historical eruptions to range from diopside to augite in composition, and also recognised that clinopyroxene cores were generally higher in enstatite compared to the rims. In contrast, only some of the orthopyroxene crystals from historical eruptions contain enstatite-rich cores (rims and zones of many orthopyroxene crystals contain greater or equal proportions of enstatite compared to the cores).

Table 5.3 Endmember proportions calculated for cores, rims, and intermediate zones of clinopyroxene phenocrysts from the 1975 inner crater rim deposit of Ngauruhoe (calculations based on normalised microprobe data). Pyroxene endmembers include wollastonite (Wo), ferrosilite (Fs), and enstatite (En).

Spot[1]	Wo	Fs	En
Bv1_cpx1_rim01	39.79	16.93	43.28
Bv1_cpx5_core01	36.14	21.09	42.77
Bv1_cpx5_rim01	42.49	12.93	44.58
Bv1_cpx5_rim02	38.32	22.31	39.37
Bv1_cpx5_rim03	40.00	16.58	43.42
Bv1_cpx13_core01	39.40	19.01	41.59
Bv1_cpx13_rim01	37.78	22.31	39.91
Bv1_cpxb_core01	39.75	18.14	42.11
Bv1_glom1_rim02	38.36	22.14	39.50
Bv2_cpx2_core01	39.74	18.69	41.57
Bv2_cpx2_rim01	37.14	21.77	41.09
Bv2_cpx3_core01	41.60	16.29	42.11
Bv2_cpx3_rim01	38.33	17.24	44.43
Cd3_cpx2_core01	37.67	12.14	50.19
Cd3_cpx2_zone1	37.92	19.12	42.96
Cd3_cpx2_zone2	36.61	24.33	39.06
Cd3_cpx2_rim01	37.19	20.30	42.51

[1] Filename nomenclature for each probe spot begins with a thin section reference, including the facies from which the clast was derived from (e.g. B or C), clast type (d = dense, v = vesicular), and the clast number (e.g. 1 = first clast, 2= second clast). Second part of file nomenclature is the crystal reference used for probe work (e.g. cpx1 = clinopyroxene crystal 1), and final part of file nomenclature is the probe location (e.g. core, rim, or intermediate zone).

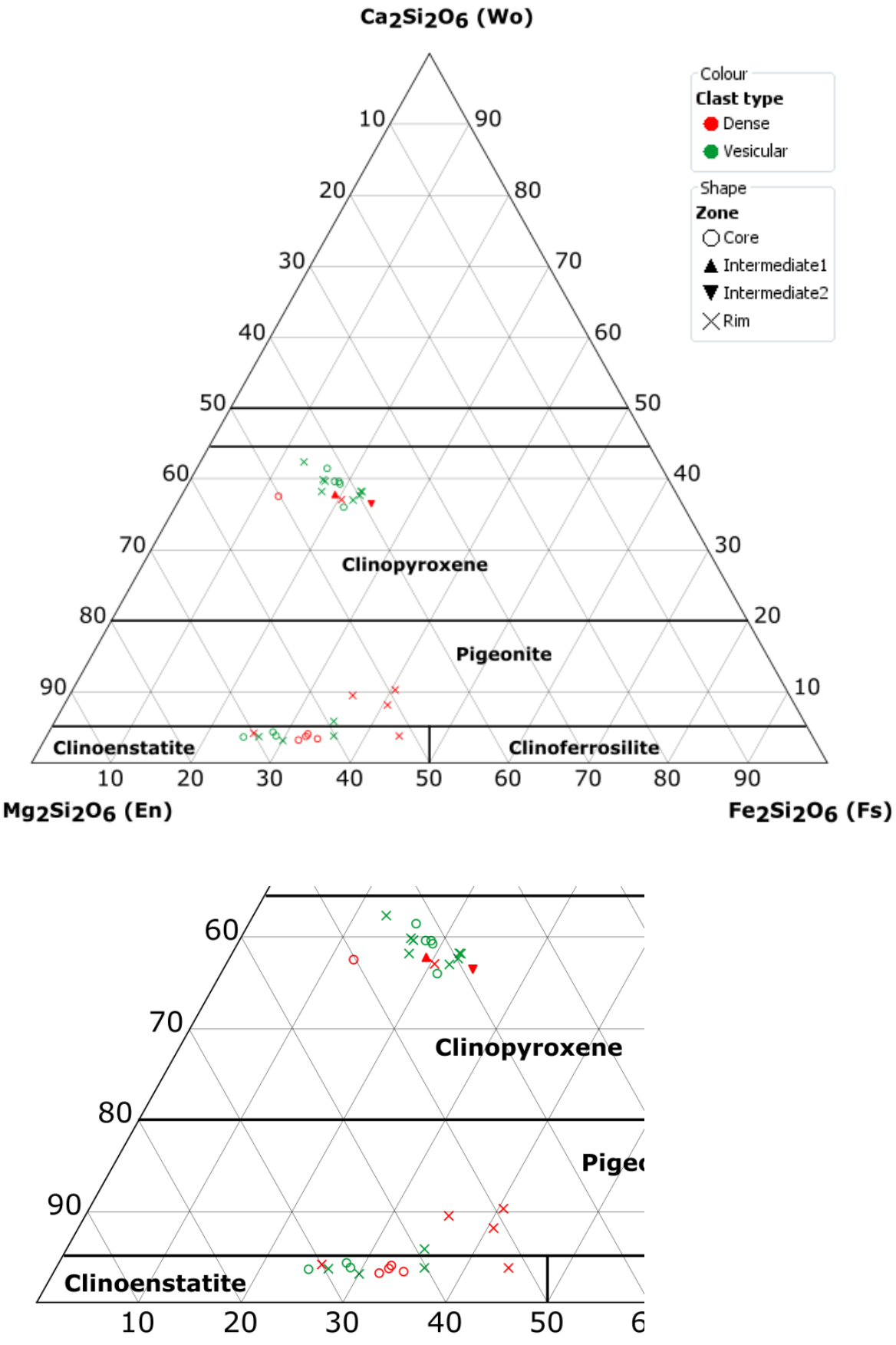

Figure 5.4 Ternary diagram of pyroxene core and rim compositions probed in dense and vesicular clasts from the 1975 eruption of Ngauruhoe. Note that the bottom figure is an enlarged extract of the data from the above ternary diagram.

5.3.3 Olivine

The olivine solid solution series includes the magnesium endmember forsterite (Fo), i.e., Mg/(Mg + Fe), and the iron endmember fayalite (Fa), i.e., Fe/(Fe + Mg). Olivine phenocrysts from the 1975 Ngauruhoe eruption range from $Fo_{67-80,}$ and many of the olivine crystals have orthopyroxene rims with compositions of En_{57-65} (Table 5.4). This enstatite content is similar to the orthopyroxene analyses above, and in particular the orthopyroxene rims which were found to range from $En_{49-70.}$ Olivine phenocrysts with pyroxene rims have also been observed in the 1954 lava flows (Sanders, 2010), the 1954 crater rim deposit (Krippner, 2009), and other Tongariro North Crater deposits (Griffin, 2007). Microprobe data was only obtained for one olivine core/rim pair, for which Mg is more enriched in the core and Fe is more enriched in the rim (Table 5.5).

Table 5.4 Endmember proportions for olivine pyroxene rims, based on calculations from normalised microprobe data. Pyroxene endmembers include wollastonite (Wo), ferrosilite (Fs), and enstatite (En).

Spot[1]	Wo	Fs	En
Bv1_olivine1_rim	9.23	34.21	56.57
Bv1_olivine3_rim	4.18	37.55	58.28
Bv2_olivine2_rim	3.79	31.10	65.11
Cd3_olivine2_rim	4.51	30.59	64.90
Cd3_olivine3_rim	4.28	30.60	65.12

Table 5.5 Endmember proportions for olivine phenocrysts, based on calculations from normalised microprobe data. Olivine endmembers include fayalite (Fa), and forsterite (Fo).

Spot[1]	Fa	Fo
Bv1_olivine1_core	22.83	77.17
Bv2_olivine1_core	20.86	79.14
Bv2_olivine1_rim	32.54	67.46
Bv2_olivine3_core	24.09	75.91
Cd3_olivine2_core	21.03	78.97
Cd3_olivine3_core	19.94	80.06

[1] Filename nomenclature for each probe spot begins with a thin section reference, including the facies from which the clast was derived from (e.g. B or C), clast type (d = dense, v = vesicular), and the clast number (e.g. 1 = first clast, 2= second clast). Second part of file nomenclature is the crystal reference used for probe work (e.g. olivine1 = olivine crystal 1), and final part of file nomenclature is the probe location (e.g. core or rim). Note that this footnote applies to both of the above tables.

5.4 Microprobe Glass Results

5.4.1 Groundmass Glass in the 1975 Clasts

Groundmass glass associated with the 1975 eruption of Ngauruhoe is predominantly andesite to dacite in composition (Figure 5.5), typically ranging from ~61 to 65 wt. % SiO_2. Barton (2011) also found groundmass glass from historical Ngauruhoe eruptions to be considerably more silicic (dacitic to rhyolitic), compared to the basaltic andesite bulk rock composition provided by Hobden (1997).

Both TiO_2 (~1.25%) and MgO (~1.5-2%) remain fairly constant with increasing SiO_2, although MgO appears to have a very slight decreasing trend (Figure 5.6). Groundmass glass has a small range in FeO (~8-10%) and Al_2O_3 (~14-17%, although most points fall between ~14 and 15%), and both of these major elements appear to have a slight decreasing trend with increasing SiO_2. A negative correlation also occurs for CaO (which ranges from approximately 4-6%) against SiO_2.

There is no obvious trend between Na_2O and SiO_2 in the groundmass glass data (for which Na_2O ranges from 2.5-4.5%) (Figure 5.6) Groundmass glass associated with the 1975 eruption mostly plots in the medium K calc-alkaline series (1.5-2.25%), however there is also a smaller grouping of data plotting in the high K calc-alkaline series (2.5-3.25%). Several groundmass points also have very high (>4 %) K_2O and fall in the shoshonite series (Figure 5.6). A positive correlation may exist between K_2O and SiO_2, particularly within the medium K calc-alkaline series (Figure 5.6).

5.4.2 Melt Inclusions in the 1975 Clasts

Two different populations of melt inclusions are identified in the Harker plots and TAS diagram. Group 1 overlaps with the groundmass glass data but has a much wider range in SiO_2 (~56-64%), while group 2 contains much higher SiO_2 values (66-70%) and consistently plots as a separate grouping (Figures 5.5 and 5.6). Group 1 melt inclusions contain a much wider range in TiO_2 (~0.75-1.6%) and FeO (~12-19%) compared to the groundmass glass (Figure 5.6). Due to high scatter, there is no obvious correlation between SiO_2 and these elements. There is also substantial

variation in MgO (~1.5-10%) and Na_2O (~0.5-4.5%), however there may be a slight positive trend between Na_2O and SiO_2 (Figure 5.6). A majority of the group 1 melt inclusions range from 1-3% MgO and follow the same trend as the groundmass glass, however some points deviate from this trend and range from 4-10% MgO.

There appears to be two distinct clusters in K_2O for the group 1 melt inclusions (Figure 5.6). Both clusters display an increasing trend between K_2O and SiO_2; however, one predominantly falls in the medium K calc-alkaline series (~0.75-2.25%) while the other contains very high K (>3.37%) and falls in the shoshonite series. In contrast, a negative correlation exists between SiO_2 and CaO (~2.5-8%), and SiO_2 and FeO (~7-12%), and the group 1 melt inclusions have a wider range in these major element proportions compared to groundmass glass (Figure 5.6).

The group 2 melt inclusions are generally lower in TiO_2 (~0.5-1%), FeO (<5%), MgO (<1%), and CaO (<3.5%) compared to the groundmass glass and group 1 melt inclusions (Figure 5.6). In contrast, Al_2O_3 is typically higher in the group 2 melt inclusions compared to the groundmass glass (Figure 5.6). There appears to be a positive correlation between SiO_2 and K_2O, with the group 2 melt inclusions predominantly falling in the high K calc-alkaline series (~2.5-4.5% K_2O) (Figure 5.6).

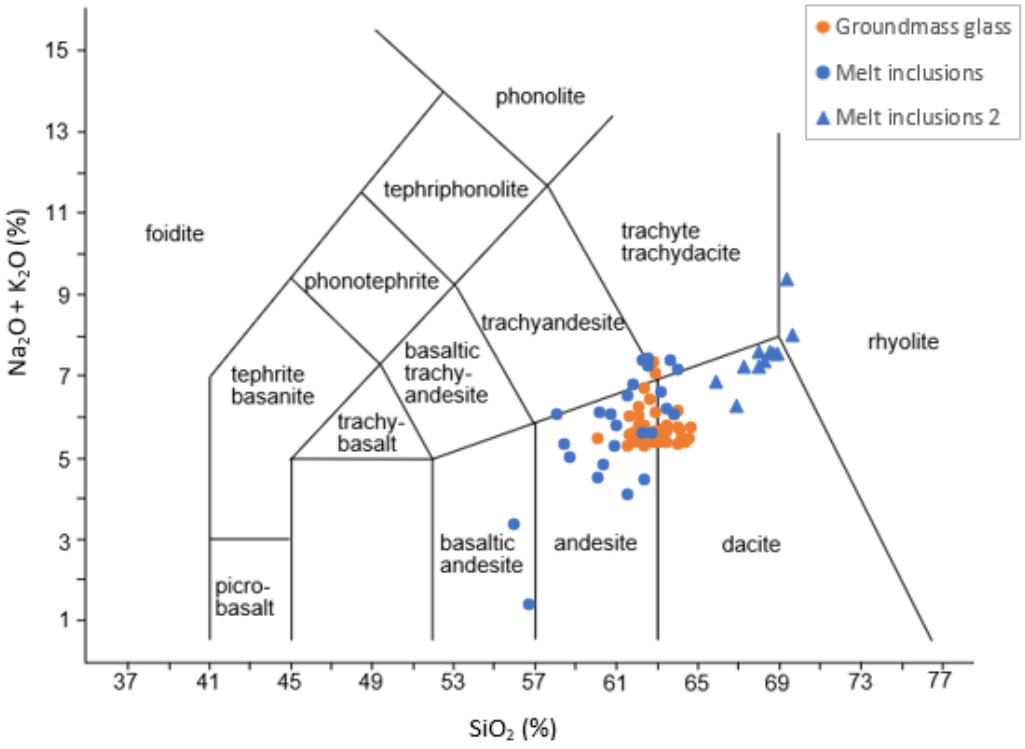

Figure 5.5 Total alkali versus silica (TAS) classification diagram of groundmass glass and melt inclusions in clasts from the 1975 eruption of Ngauruhoe. Note that the triangles represent the higher SiO2 (group 2) melt inclusions.

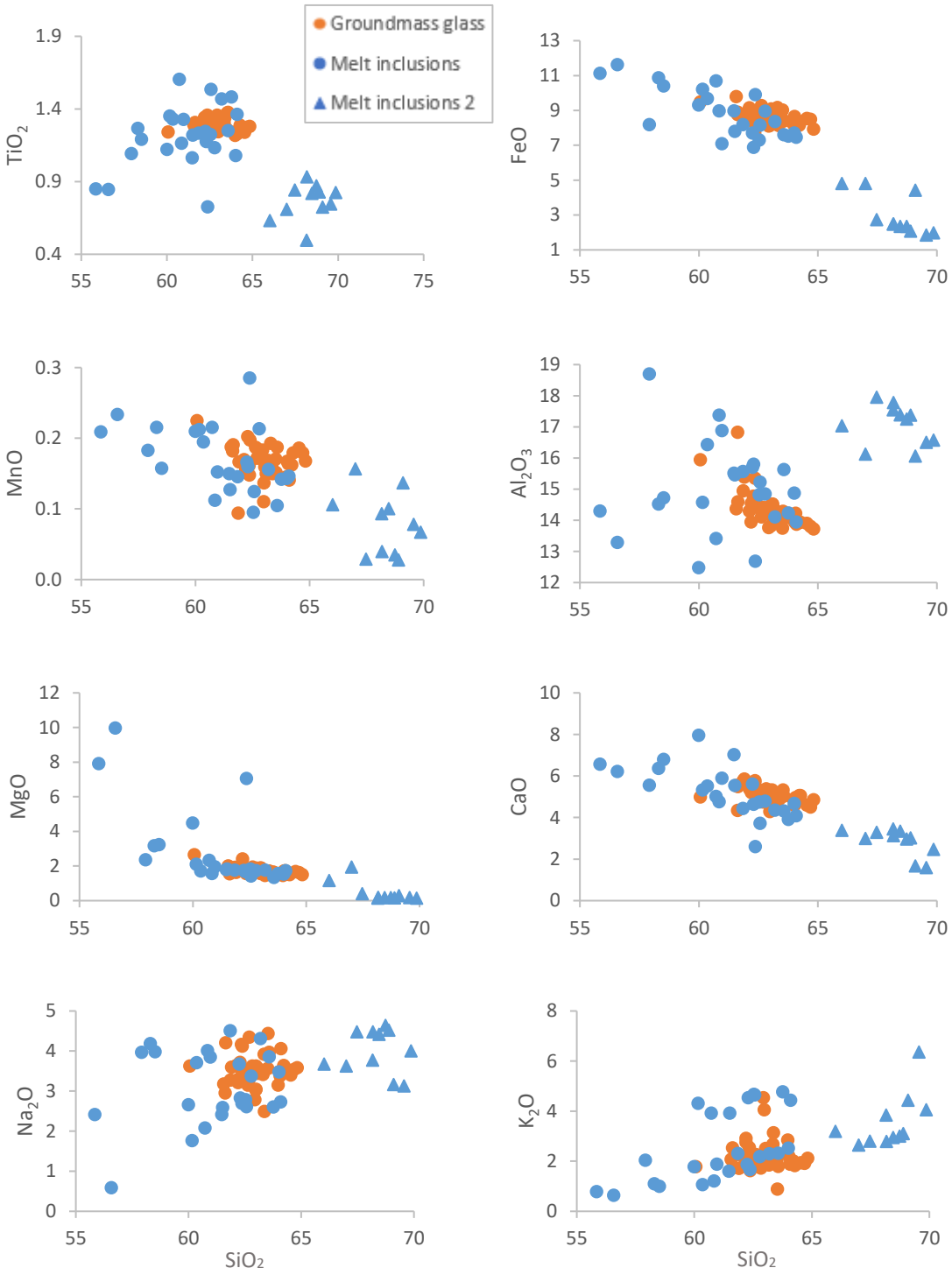

Figure 5.6 Harker diagrams illustrating the proportion of SiO_2 against various element oxides in groundmass glass and crystal-hosted melt inclusions from the 1975 Ngauruhoe eruption (data from normalised microprobe analyses). Note that blue triangles represent the group 2 melt inclusions; they have been identified to plot in a consistent grouping across all Harker plots, with a very high SiO_2 content i.e., >65%.

Figure 5.7 plots K_2O and Na_2O against FeO in order to compare the on-cone glass analyses against the glass analyses in tephras obtained by Moebis *et al.* (2011). Groundmass glass analyses of clasts from the 1975 inner crater rim deposit plot consistently in the realm of the Ngauruhoe tephra data (i.e. ~3-4 wt. % Na_2O, ~7-10 wt. % FeO, and ~1.5-3 wt. % K_2O) (Figure 5.7). While the groundmass glass analyses seem to match, the melt inclusions are quite different, containing lower FeO (i.e ~2-5%) compared to the tephras analysed by Moebis (Figure 5.7).

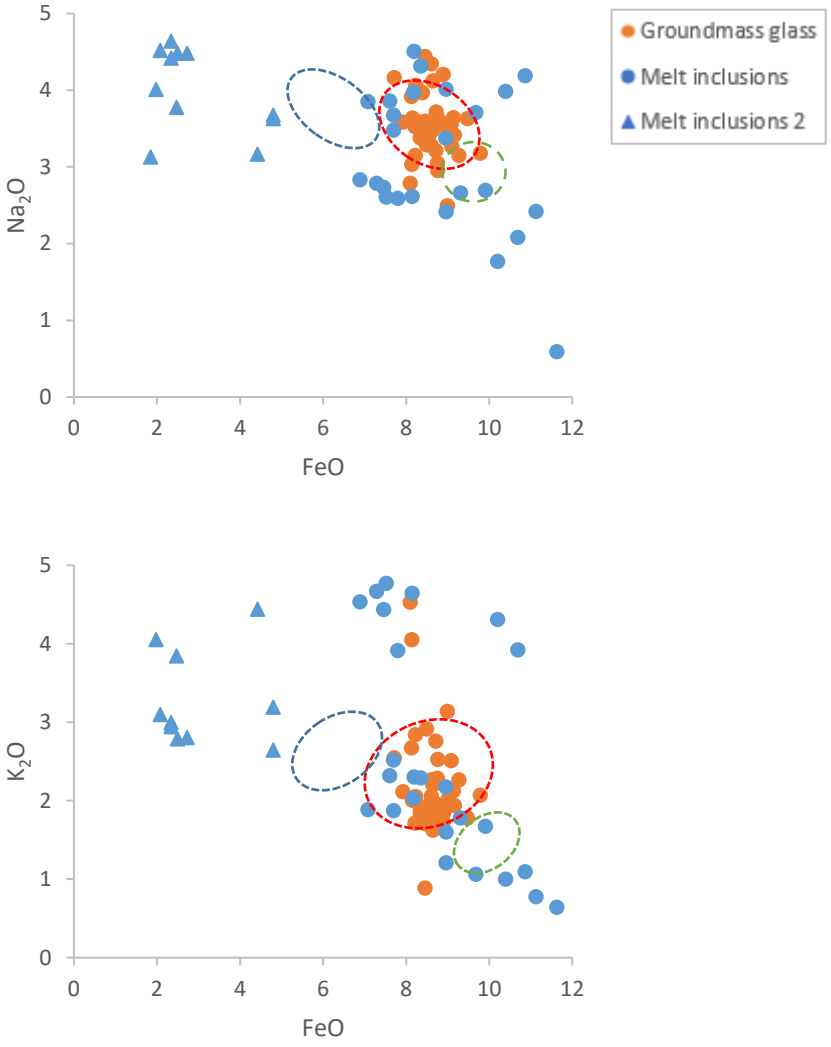

Figure 5.7 Major element compositions of groundmass glass and crystal-hosted melt inclusions within clasts erupted from Ngauruhoe in 1975, compared to tephra data from Moebis *et al.* (2011). The ellipsoids represent the glass chemistry of tephras erupted from Ruapehu (blue) and Tongariro (red = Ngauruhoe, green = Red Crater) that are younger than c. 12,000 years.

5.4.3 Glass Compositions (1954-1975)

Glass from various Ngauruhoe eruptions over time (1954-1975) have been plotted on Harker diagrams to help identify any sequential/eruption-based trends, as well as any correlations between various element oxides and silica content.

There appears to be two recognisably different groups of data which consistently plot discrete from one another (Figures 5.8 and 5.9). One group (group 1) primarily includes glass in the 19th February 1975 ash and groundmass glass of the 1975 crater rim clasts. Some ash probed from earlier eruptions (11-12th February 1975 and 28th March 1974) also fall in this grouping, in addition to the lower SiO_2 group of melt inclusions identified in Figures 5.5 and 5.6 (although their wider spread in element oxides relative to the 1975 groundmass glass is described in section 5.4.2.). Group 1 mostly falls in the andesite to dacite fields (Figure 5.8) with silica contents between ~57.5-67.5%. In contrast, the remaining glass data (group 2) ranges from dacite to rhyolite in composition (i.e. contains higher silica contents of ~65-80%) and includes glass from events prior to the climactic 19th February 1975 eruption (Figure 5.8). The Si-rich melt inclusions identified in the 1975 clasts (Figures 5.5 and 5.6) also plot in the realm of earlier eruptions. It is important to note that some ash grains probed (particularly from the 1968 and 1972 eruptions) have unusually high silica contents >77% (Figure 5.8).

Group 1 glass is higher in TiO_2 (~1-1.75%), FeO (~7-12%), CaO (~4-9%), and slightly higher in MnO (~0.1-0.25%) and MgO (1-3%), compared to glass associated with group 2 (containing ~0-1%, 0-7%, 0-4%, ~0-0.1%, and <1% respectively) (Figure 5.9).

In contrast, group 1 glass contains less K_2O compared to group 2. Group 1 glass is predominantly medium K calc-alkaline (~1-3% K_2O), with a few data points extending into the high K calc-alkaline field (Figure 5.9). However, there appears to be a distinct population of glass from group 1 which are classified as shoshonite due to very high K_2O values of 4-5%. This includes some of the 1975 melt inclusions, some 11-12th February ash, and some 1975 groundmass glass (Figure 5.9). Glass associated with group 2 ranges from ~2-6% K_2O, and mainly falls in the high K calc-alkaline series (Figure 5.9).

There is a negative trend in Al_2O_3 and CaO, and a positive trend in K_2O, with increasing SiO_2 for all glass data (Figure 5.9). There is also a negative trend in FeO and MgO (and a slight negative trend in MnO) with increasing SiO_2, when solely focusing on group 1 glass. A slight negative correlation also exists between SiO_2 and Na_2O for glass from the earlier group 2 eruptions (Figure 5.9). No obvious correlation exists between SiO_2 and TiO_2 (in any glass data), SiO_2 and Na_2O (group 1 glass), or SiO_2 and FeO, MnO or MgO (group 2 glass) (Figure 5.9).

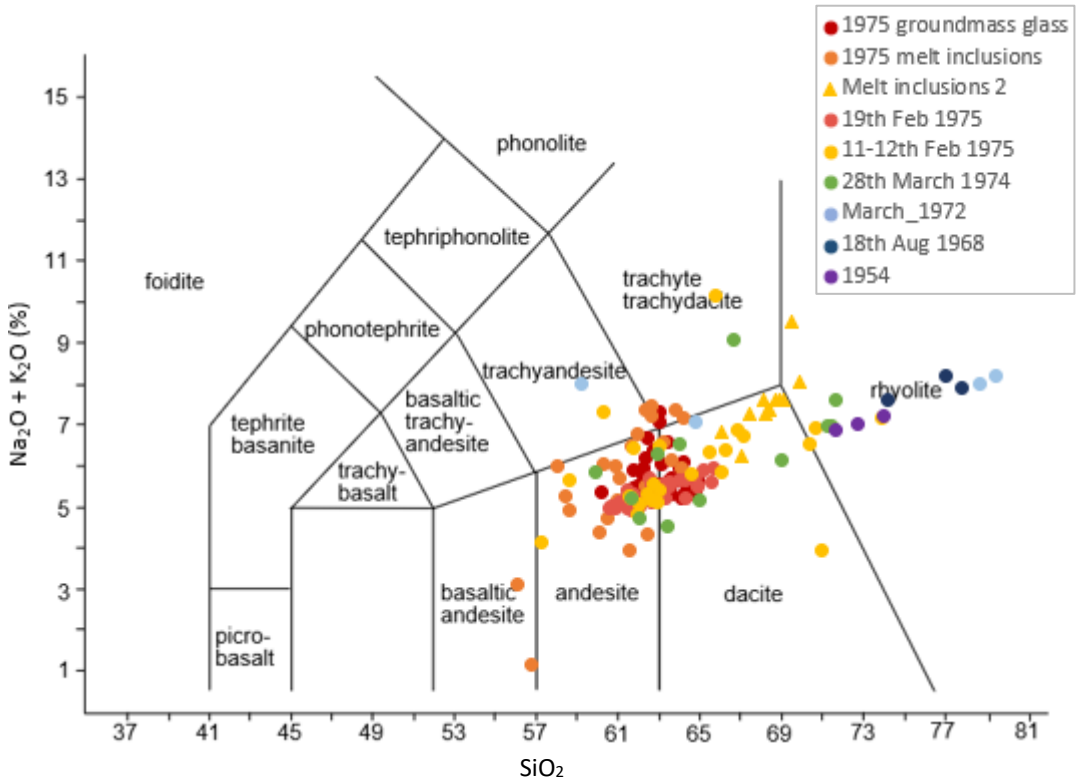

Figure 5.8 Total alkali versus silica (TAS) classification diagram of glass associated with various eruptions from Ngauruhoe (1954-1975).

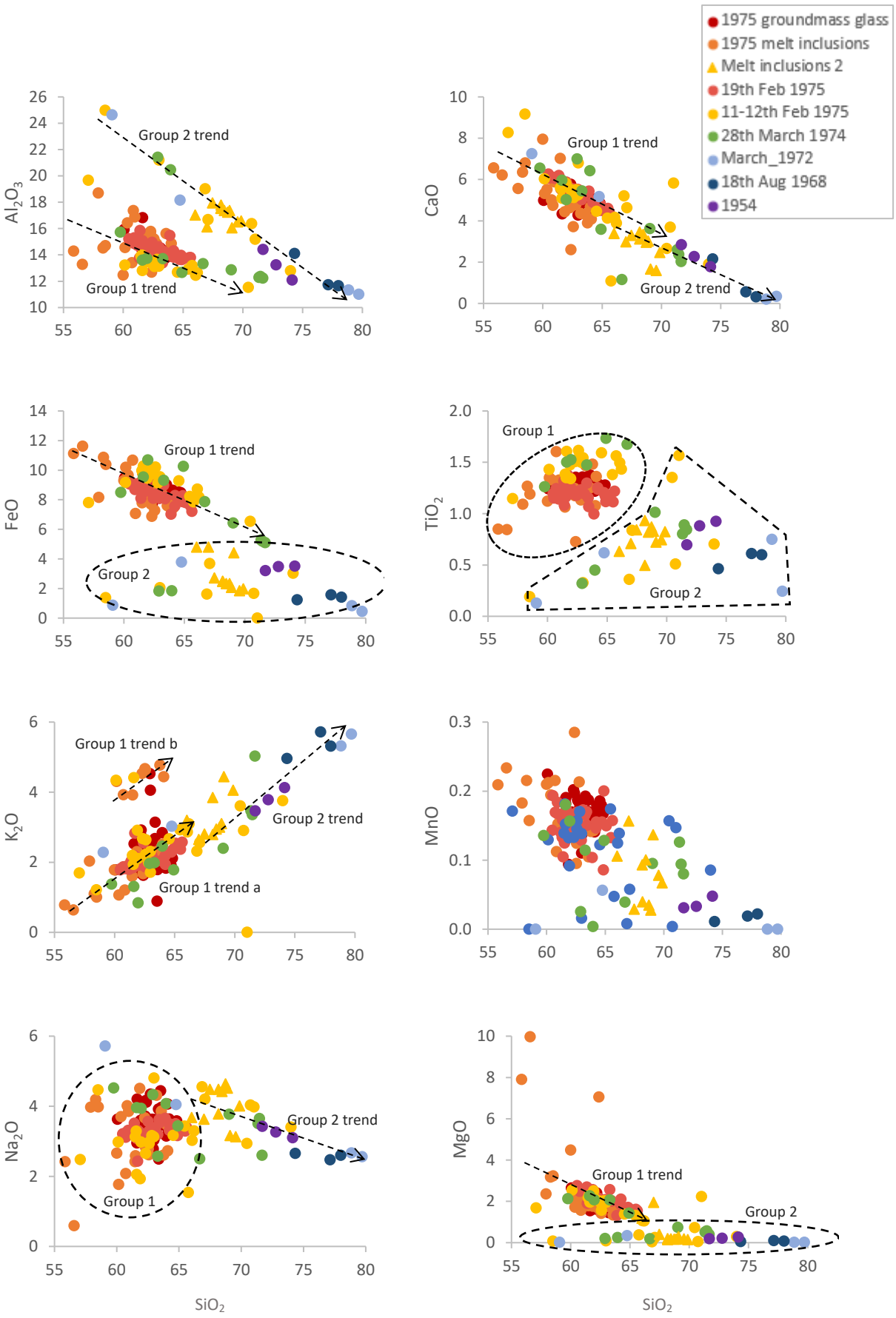

Figure 5.9 Harker diagrams illustrating the proportion of SiO_2 against various element oxides for glass probed from Ngauruhoe eruptions through time. Group 1 comprises the 19th February 1975 ash, groundmass glass of the 1975 clasts, some ash from earlier eruptions (11-12th February 1975 and 28th March 1974), and the lower SiO_2 'group 1' melt inclusions. Group 2 includes glass from events prior to the climactic 19th February 1975 eruption, in addition to the Si-rich 'group 2' melt inclusions identified in the 1975 clasts.

5.5 Geothermometry

The Rhodes diagram is a visual way to test for equilibrium between clinopyroxene and a coexisting liquid (Putirka, 2008). The exchange of Fe for Mg between a crystal and an equilibrium melt can be quantified by the Fe-Mg exchange coefficient ($Kd^{Mineral/Melt}$), which is equal to $(Fe/Mg)^{Mineral}$/ $(Fe/Mg)^{Melt}$ (Bédard, 2010). The equilibrium curve displayed in Figure 5.10 assumes an Fe-Mg exchange coefficient of 0.27, with an error of ± 0.03 (Putirka, 2008). By plotting the Mg# $\left(\frac{Mg}{Mg+Fe} \times 100\right)$ of three different groundmass glass populations against the Mg# of all the clinopyroxene rims, it becomes apparent that the clinopyroxenes are in equilibrium with the most mafic (60.06% SiO_2) groundmass glass composition. In contrast, the clinopyroxene crystals are not in equilibrium with the other groundmass glass populations (62.98% and 64.82% SiO_2) and move further away from equilibrium with increasing silica content (Figure 5.10).

According to Putirka (2008), clinopyroxene thermobarometers by Putirka *et al.* (1996) and Putirka *et al.* (2003) provide the highest precision and least systematic errors for anhydrous and hydrous systems respectively. The temperature conditions of the clinopyroxene-liquid equilibrium provided here are based on Putirka *et al.* (1996) since the water content of Ngauruhoe magmas is negligible (Lormand *et al.* (n.d.) provides an average H_2O content of 0.6 wt. %). Based on temperature calculations for the mafic liquid (which was found to be in equilibrium with the clinopyroxene rims), the temperature of the eruptible magma involved in the 1975 Ngauruhoe eruption was likely to be somewhere between 1018-1114 °C (Appendix 10). The average liquid composition provides a similar temperature range (1006-1109 °C), whereas the most silicic liquid composition gives a lower temperature range of 981-1078 °C. It is important to note that these temperature estimates are associated with an error of ±56 °C (this is the standard error given by Putirka, 2008). Although pressures were also deduced, they are not cited here due to substantially large errors of ± ~3-5 kbar (equivalent to ± ~10-15 km) (Putirka, 2008).

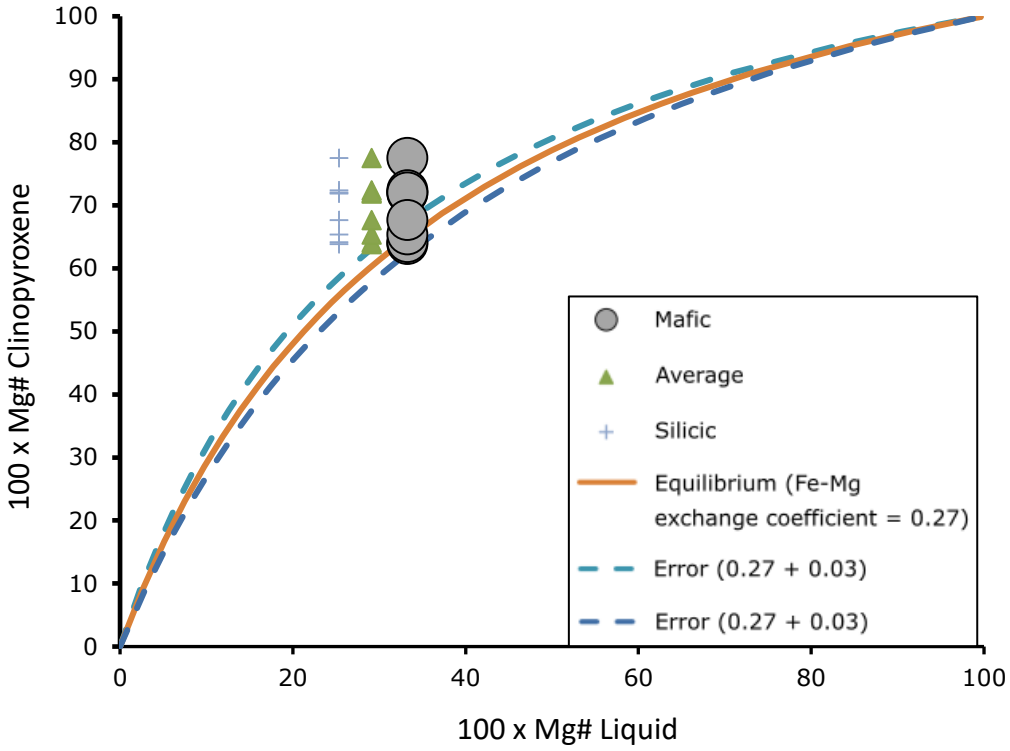

Figure 5.10 Rhodes diagram depicting the Mg# of three different liquid compositions versus the Mg# of clinopyroxene rims. The three liquid compositions illustrated include the most mafic (60.06% SiO_2), the average (62.98% SiO_2), and the most silicic composition (64.82% SiO_2). Note that the orange curve represents the exchange of Fe for Mg between a crystal and an equilibrium melt.

5.6 Summary of Key Findings

5.6.1 Mineral Chemistry

- Plagioclase phenocrysts from the 1975 Ngauruhoe eruption range from labradorite to bytownite (An_{59-90}). No clear differences were identified for plagioclase compositions between clast types (i.e. dense versus vesicular clasts).

- Plagioclase crystals commonly display normal zoning; however, one crystal probed displays reverse zoning with a higher anorthite content in the rim (An_{75}) compared to the core (An_{70}).

- Probe data suggests that across a crystal, compositional variations may be present, i.e., a simple one-way solid solution pattern is not always the case.

- Plagioclase crystals from the 1954-1975 Ngauruhoe eruptions typically range in composition from labradorite to bytownite, although a few crystals fall in the andesine composition range. All plagioclase from the

1975 eruptions contain >An_{60}, while plagioclase from earlier Ngauruhoe eruptions (including 1968, 1972, and 1974) have a greater range in compositions, extending as low as An_{48}.

- Clinopyroxene crystals have compositions ranging from $Wo_{36}En_{39}Fs_{12}$ to $Wo_{42}En_{50}Fs_{24}$, while orthopyroxene compositions range from $Wo_3En_{49}Fs_{25}$ to $Wo_{10}En_{72}Fs_{44}$. Both pyroxenes generally have more ferrosilite (Fe-rich) rims compared to the cores which are correspondingly higher in enstatite.

- Olivine phenocrysts from the 1975 Ngauruhoe eruption range from $Fo_{67\text{-}80,}$ and many have orthopyroxene rims with compositions of $En_{57\text{-}65}$ (similar to the orthopyroxene crystal rim analyses). The single olivine core/rim pair analysed contains an enstatite-enriched core and a ferrosilite-enriched rim.

5.6.2 1975 Groundmass Glass Chemistry

- Groundmass glass is predominantly andesite to dacite in composition, typically ranging from ~ 61 to 65 wt. % SiO_2. Glass analyses revealed decreasing trends in MgO, FeO, Al_2O_3, and CaO with increasing SiO_2, while a positive correlation may exist between K_2O and SiO_2, particularly within the medium K calc-alkaline series.

5.6.3 Crystal-Hosted Melt Inclusion Chemistry

- Two different populations of crystal-hosted melt inclusions were identified within the 1975 clasts. Group 1 melt inclusions overlap with the groundmass glass data but have a much wider range in SiO_2 (~56-64%), while group 2 melt inclusions contain much higher SiO_2 values (66-70%) and consistently plot as a separate grouping. Group 2 melt inclusions are generally lower in TiO_2, FeO, MgO and CaO than the groundmass glass and group 1 melt inclusions.

- Group 1 melt inclusions display a slight positive trend between Na_2O and K_2O with increasing SiO_2. Within these inclusions there appears to be two distinct clusters in terms of K_2O; one predominantly falls in the medium K

calc-alkaline series (~0.75-2.25%) while the other contains very high K (>3.37%) and falls in the shoshonite series. Decreasing trends in MgO, CaO and FeO with increasing SiO_2 are also associated with the group 1 melt inclusions.

- Group 2 melt inclusions also display a positive correlation between SiO_2 and K_2O, and predominantly fall in the high K calc-alkaline series.

5.6.4 Glass Chemistry (1954-1975)

- There appears to be two chemically different groupings (trends) of data; group one primarily includes glass in the 19th February 1975 ash, groundmass glass of the 1975 crater rim clasts, some ash from earlier eruptions (11-12th February 1975 and 28th March 1974), and the lower SiO_2 group one melt inclusions. Group 1 mostly falls in the andesite to dacite fields, while the remaining glass data (group 2) ranges from dacite to rhyolite in composition. Group 2 includes glass from events prior to the climactic 19th February 1975 eruption, as well as the Si-rich group 2 melt inclusions identified in the 1975 clasts.

- Some ash grains (particularly from the 1968 and 1972 eruptions) have unusually high silica contents, >77%.

- Group 1 glass is higher in TiO_2, FeO, CaO, (and slightly higher in MnO and MgO), but lower in K_2O, compared to glass associated with group 2.

- There is a negative trend in Al_2O_3 and CaO, and a positive trend in K_2O, with increasing SiO_2 for all glass data. A negative trend also exists for FeO and MgO in the group 1 glass, and a slight negative trend between Na_2O and SiO_2 in glass from the earlier group 2 eruptions. No obvious correlation exists between SiO_2 and TiO_2 (in any glass data), SiO_2 and Na_2O (group 1 glass), or SiO_2 and FeO, MnO or MgO (group 2 glass).

5.6.5 Geothermometry

- The temperature of the eruptible magma involved in the 1975 Ngauruhoe eruption was likely somewhere between 1018-1114 (±56) °C, based on clinopyroxene-liquid equilibrium.

Chapter Six

Discussion

6.1 Introduction

This chapter discusses the processes associated with the 1975 Ngauruhoe eruption based on the results of this study, including long-term magma evolution, inferences regarding precursory eruptions, and shallow magma priming. Field evidence and eye-witness accounts are later incorporated into a discussion of the various styles of activity (and accompanying magmatic and fragmentation mechanisms) that occurred during this eruptive period. Cooling and degassing processes, and emplacement processes on the crater rim, are subsequently addressed, in addition to the application of this research to understanding the volcanic hazard.

6.2 Precursory Eruptions (Leading up to February 1975)

The precursory sequence leading up to the eruption in February 1975 is considered to begin from early 1972. While a large number of ash samples were available for analysis, time constraints and extensive trial and error associated with shape studies (in addition to insufficient ash quantities of some sub-samples) limited analyses to six ash samples from different eruptions through time; including eruptions on the 24th of March 1972, 26th of October 1973, 7th of December 1973, 24th of January 1974, 28th of March 1974, and 17th of February 1975. Geochemical data of 1954 and 1968 ash, and tephra erupted from Ngauruhoe over the past 7 ka (Moebis *et al.*, 2011), also provide a comparison for this study.

6.2.1 Geochemical Comparison between the 19th February 1975 Eruption and Precursory Eruptions

Glass analyses of ash samples from several eruptions between 1954-1975 indicate that the 1975 eruption is geochemically different to earlier eruptions (particularly those which occurred in 1954, 1968 and 1972). This is evident from the distinct trends/groupings displayed by these eruptions across various Harker diagrams

(Figure 5.9). The earlier eruptions appear to be associated with a more evolved melt compared to 1975, with most glass analyses ranging from dacite to rhyolite in composition (whereas most glass analyses from 1975 fall in the andesite to dacite fields) (Figure 5.8). Some glass analyses from 1968 and 1972 contain unusually high SiO_2 contents (>77%), which may be a consequence of hydrothermal alteration especially if associated with the formation of silica-polymorphs (Boudon *et al.*, 1998), such as cristobalite identified in the March 1972 ash.

6.2.2 Precursory Events to 1975

Samples of volcanic ash produced from several eruptions between 1972 and 1975 were analysed to detect any changes in componentry or grain morphologies over time, and thus make inferences about processes/events that may have been involved in the lead up to the climactic 19th of February 1975 eruption. Results from combined stereoscopic observations, XRD analyses, and ImageJ shape analyses indicate that ash produced from the eruption on the 24th of March 1972 is particularly different from the eruptions that followed.

The 1972 ash is predominately composed of lithics, which appear to be quartz-rich and hydrothermally altered. This stereoscopic observation is supported by XRD analyses, in which the presence of cristobalite was identified solely in this ash sample. Cristobalite is a non-magmatic mineral that is reported to be associated with hydrothermal alteration in several volcanic settings, such as Ruapehu and White Island (Wood, 1994) and Soufriere Hills volcano in Montserrat (Boudon *et al.*, 1998). At White Island, the presence of cristobalite is also related to halogen degassing (i.e. the portioning of chlorine and fluorine into H_2O-rich fluid in isolated pores) during shallow magma ascent (Schipper *et al.*, 2017). Therefore, this could provide an alternative explanation for the presence of cristobalite in the 1972 Ngauruhoe ash.

The high abundance of lithics in the 1972 ash suggests that this eruption involved conduit wall degassing, or simply strong degassing, that mined some of the plug/hydrothermally altered rock (perhaps in the restricted extent of the hydrothermal system) (Clarke *et al.*, 2015). The lithics possibly represent degassed

and solidified magma remaining in the conduit from earlier eruptions in 1954-55. A high volume of magma was erupted from strombolian-style fire fountains and lava flows during these eruptions (i.e. ~10 million m^3 between June and September of 1954) and incandescent lava remained in the crater until the 25th of June (Gregg, 1956; Cole & Nairn, 1975; Hobden *et al.*, 2002). It is therefore highly likely that some magma would have solidified in the conduit and undergone subsequent hydrothermal alteration. However, it is also possible that at least some of the lithics were older, i.e., pre-1954 wall rock similar to hydrothermally altered rock outcrops at the bottom of the crater.

Shape analyses also support the above interpretation regarding the 1972 ash, as it is primarily composed of glassy dense grains with high convexity and solidity values. Nurfiani and de Maisonneuve (2018) and Liu *et al.* (2015) discuss how shape analyses of a consistent grainsize can provide important information about fragmentation processes, due to obvious differences between dense grains, often derived from the brittle fragmentation of non-juvenile, poorly-vesicular, and hydrothermally altered conduit rock, and vesicular grains, produced by the fragmentation of gas-bearing juvenile magma.

It is difficult to say with certainty when juvenile magma was fragmented and then incorporated into ash-producing events between 1972 and 1975. It is likely that eruptions following, and possibly including, the 26th of October 1973 eruption involved fragmentation of a fresh magmatic component based on stereomicroscopic observations (the presence of black vitreous grains and red vesicular grains) and shape analyses (the presence of glassy vesicular grains). This is consistent with Cole and Nairn (1975), and Nairn and Self (1978), who found petrographic evidence for a fresh glassy magmatic component from eruptions including and following the minor eruptive period which took place on the 7-15th of December 1973.

A few red vesicular grains were observed (under the stereomicroscope) in ash produced during October 1973, and a minor amount of glassy vesicular grains were identified from shape analyses carried out as part of this study. This may be evidence for the involvement of a very minor fresh magmatic component during

this eruption, in contrast to Nairn *et al.* (1976), who did not find any evidence for a fresh magmatic component.

6.3 Magmatic Evolution Processes

6.3.1 Crystal Fractionation

Crystal fractionation is the process by which crystals are formed and removed from the melt, and the composition of the remaining liquid follows the liquid line of descent (i.e. becomes progressively enriched in SiO_2). This is considered one of the dominant methods by which magmas differentiate from the initial parent liquid (Winter, 2013) and has been suggested to be a key process resulting in the diversity of major element compositions throughout the TgVC eruptives (Gamble *et al.*, 1990). Crystal fractionation can explain why the composition of 1975 groundmass glasses are consistently more felsic (typically ranging from about 61-65 wt. % SiO_2) compared to the bulk composition i.e., 52-58 wt. % SiO_2 (basaltic-andesite to andesite) (Hobden, 1997; Krippner, 2009).

Some identifiable major element trends from the groundmass glass of 1975 scoria clasts are consistent with crystal fractionation processes. The decreasing trend in MgO, FeO and CaO with increasing SiO_2 is consistent with the removal of early-crystallizing olivine, pyroxene and plagioclase phases from the cooling liquid. A slight negative correlation also exists between Al_2O_3 and SiO_2 which is consistent with the crystallization of plagioclase.

Two distinct groups of melt inclusions were identified in the 1975 clasts; group 2 melt inclusions contain much higher SiO_2 and lower CaO, Al_2O_3, and MgO contents compared to the groundmass glass and group 1 melt inclusions (and also bulk rock compositions, by XRF analysis, Krippner, 2009). Moebis *et al.* (2011) attained geochemical data for tephra glass erupted from Ngauruhoe over the last 7 ka, for which SiO_2 was found to range from ~58.6-63 wt. %. This is fairly consistent with the range of SiO_2 measured in groundmass glass (61-65 wt. %) and the group 1 crystal-hosted melt inclusions (56-64%) in clasts erupted during 1975. The group 1 melt inclusions occupy a wider range and are often less evolved than the groundmass glass (i.e. range to lower SiO_2 and higher MgO contents), which is to be expected if they were entrapped within an evolving magma.

Both groups of melt inclusions display decreasing trends in MgO with increasing SiO_2, consistent with crystal fractionation of pyroxene and early-crystallizing, forsterite-rich olivine (part of the 1975 mineral assemblage). Similar to the groundmass glass, crystal fractionation is also supported in both groups of melt inclusions by the decrease in CaO and Al_2O_3, and apparent increase in K_2O (and Na_2O in the group 1 inclusions), with increasing silica. Interestingly, both groups display a substantial amount of scatter in terms of FeO (i.e. no obvious trends to support crystal fractionation), and the more silicic melt inclusions are generally quite high in Fe. The high iron content could be due to dissolution of magnetite in homogenised (re-melted) inclusions, and in which case would not reflect the original composition of the trapped melt (Rowe *et al.*, 2006).

Some chemical features cannot be explained by crystal fractionation (the most noticeable being the group of melt inclusions with higher SiO_2 contents compared to the groundmass glass), suggesting that an open-system process, i.e., magma mixing, likely occurred during the evolution of the magma.

6.3.2 Magma Mixing

Magma mixing is another process that can modify the composition of an eruptible magma. Until recently, magma chambers were thought of as large pools of melt in the shallow crust, and there are two scenarios which may lead to magma mixing on the basis of this assumption: 1) due to thermal or chemical convection in a single temperature-zoned magma chamber (Couch *et al.*, 2001), or 2) as a result of recharge of the magma chamber due to the interaction of a new magma with contrasting composition and temperature (Sparks *et al.*, 1977; Huppert *et al.*, 1982; Grove, 2000; Murphy *et al.*, 2000). Convective self-mixing involves a magma body of a single composition which is heated from below, usually by a hot, mafic magma intruded into the base of the magma chamber (Figure 6.1). The formation of a thermal boundary layer typically results in crystal resorption, and the subsequent convective mixing that occurs may account for disequilibrium textures such as sieve-textures and crystal zonation (Couch *et al.*, 2001). However, magma chambers are now considered to be reservoirs with distinct crystal-rich (mush)

versus crystal-poor (melt-rich) zones that may mix in the lead up to an eruption (Kilgour *et al.*, 2013; Cashman & Giordano, 2014; Cashman *et al.*, 2017).

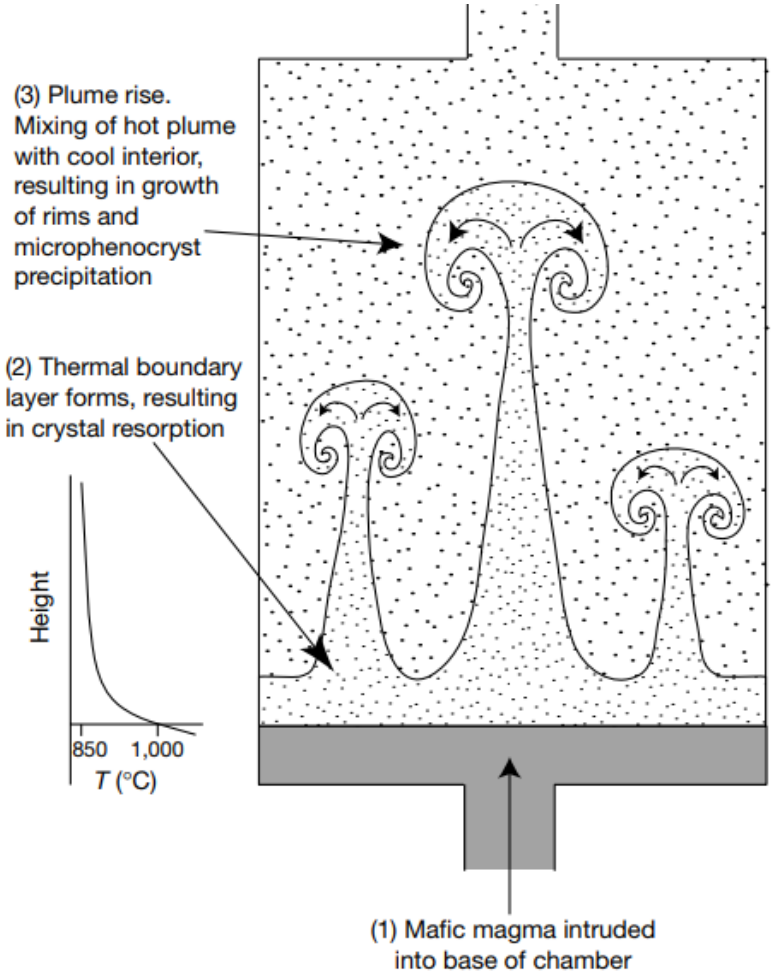

Figure 6.1 Conceptual model of convective-self mixing that may occur in a temperature-zoned magma chamber. The intrusion of hot mafic material into the base of a cooler, more silicic, magma body results in a hot siliceous layer. This thermal layer eventually becomes buoyant and leads to the development of convective plumes which mix with the cooler siliceous magma (Couch *et al.*, 2001).

Evidence for magmatic processes and compositions can be preserved during the growth of minerals as they respond to changing magmatic environments (Ginibre *et al.*, 2007; Streck, 2008). According to Streck (2008), mineral textures and compositional zoning provide some of the best evidence for magma mixing. Abundant phenocryst resorption textures were observed in the Ngauruhoe 1975 inner crater eruptives; including subhedral morphologies, cavities, and embayments in some larger pyroxenes (Figures 4.6 and 4.8), and frequent sieve-textures in plagioclase (Figure 4.4).

Plagioclase phenocrysts commonly exhibit sieved centres and non-sieved rims, multiple clear and sieved concentric zones, and both fine and coarse sieving within

a single sample. Sieve-textures represent partial dissolution driven by thermal and chemical disequilibrium, while non-sieved zones represent continued crystal growth following re-equilibration between the crystal and the melt (Streck, 2008; Maro & Caffe, 2016). Therefore, it can be interpreted that some plagioclase crystals (with multiple clear and sieved zones) have undergone several partial dissolution and crystal growth events during their history. Most plagioclase crystals contain non-sieved, euhedral rims which may be attributed to crystallization following re-equilibration, but also to cooling and the loss of volatiles in shallow crustal magmas prior to eruption (Nelson & Montana, 1992).

The occurrence of sieve textures can be attributed to convective-self mixing, rising and falling within the conduit, or magma mixing of two chemically distinct melts (in which the crystals are out of equilibrium) (Tsuchiyama, 1985; Couch *et al.*, 2001; Gill, 2012). There are many volcanic examples where sieve textures have been attributed to magma mixing, such as Tongariro, New Zealand (Hobden 1999), Narcondam volcano, Andaman Sea (Tsuchiyama, 1985), Stromboli, Italy (Landi *et al.*, 2004), and Mount St. Helens, Washington (Pearce *et al.*, 1987). However, some studies also suggest that sieve textures (particularly coarse sieving) may also result from rapid decompression in a dry system (Vance, 1965; Stormer Jr, 1972; Nelson & Montana, 1992; Hobden, 1997; Blundy & Cashman, 2001). Therefore, it may not be appropriate to infer magma mixing solely on the basis of sieving. Additional evidence to support this process can be obtained from compositional crystal zoning, and compositional analyses of groundmass glass and melt-inclusions.

Crystal zonation is a consequence of changes in temperature, pressure, water content, and/or oxygen fugacity, and oscillatory zoning which was observed in plagioclase crystals from the 1975 eruption may be associated with pulsatory changes in these factors (Humphreys *et al.*, 2006). Plagioclase has been widely used to study and reconstruct crustal magmatic processes since its stability and growth are sensitive to changes in water content, temperature, and melt composition (Coote & Shane, 2016). Most of the plagioclase phenocrysts analysed from the 1975 eruption of Ngauruhoe exhibited normal zoning (i.e. anorthite content is typically higher in the cores compared to the rims), congruous with findings from Coote and Shane (2016) and Barton (2011) who studied historic lava

flows from Ngauruhoe. This compositional change preserved during crystal growth is consistent with a progressively evolving melt (i.e. it reflects the cooling and chemical differentiation of the host magma) (Streck, 2008).

Unlike Coote and Shane (2016) who found all plagioclase rims to be in equilibrium with the erupted melt, in this study reverse plagioclase zoning was identified in some plagioclase phenocrysts thus providing evidence for magma mixing during the evolution of the magma which erupted in 1975 (Hobden *et al.*, 1999; Ginibre *et al.*, 2007; Streck, 2008). Reverse zoning may be present if plagioclase crystals grew from a more calcic/mafic melt which subsequently mixed with a more evolved melt, or if there was an increase in temperature (i.e. due to convective self-mixing or interaction with a hotter, recharging magma) (Couch *et al.*, 2001; Streck, 2008).

Reaction textures, such as the formation of growth mantles on existing minerals, have also been interpreted to result from magma mixing (Tepley *et al.*, 1999; Streck, 2008). The peritectic reaction that gives rise to olivine crystals rimmed by orthopyroxene is a two-step process induced by disequilibrium conditions. The first step involves dissolution of forsteritic (Mg-rich) olivine which leads to Mg being enriched in the melt boundary layer around the crystal. This layer then facilitates nucleation and growth of magnesian pyroxenes, which shield the olivine from the melt and prevent further dissolution (Tsuchiyama, 1985; Coombs & Gardner, 2004; Zellmer *et al.*, 2016). Olivine crystals with orthopyroxene rims observed in the Ngauruhoe 1975 eruptives, similarly to those observed in andesite-dacite form the Narcondam and Barren volcanic islands (Tsuchiyama, 1985; Ray *et al.*, 2011), provide evidence for magma mixing.

Evidence for magma recharge can also be obtained by analysing the composition of groundmass glass and crystal-hosted melt inclusions. Geochemical analyses of groundmass glass provide compositional information regarding the final stage magma, while melt inclusions preserve compositional information from the time of entrapment. Compositional analyses of the groundmass glass in two black scoria clasts from facies B of the inner crater rim deposit show a wide range (~5 wt%) in SiO_2, attesting to the heterogenous nature of the groundmass glass.

This can be interpreted to result from the mixing of compositionally different magmas, as suggested by Kilgour (2013) who also found groundmass glasses from Ruapehu to be heterogenous in silica content.

The occurrence of a melt inclusion population containing higher silica contents than the groundmass glass is not an uncommon phenomena and has been detected in several volcanic settings worldwide, including Arenal volcano in Costa Rica (Streck & Wacaster, 2006), Ruapehu volcano in New Zealand (Kilgour *et al.*, 2013), and Soufriere Hills volcano in Montserrat (Murphy *et al.*, 2000), to name a few. Based on these studies which suggest that the high silica melt inclusion population is not directly related to the host melt, it can thus be inferred that the transporting magma involved in the 1975 Ngauruhoe eruption may have interacted with, and entrained, exotic crystals from a cooler, more evolved crystal mush zone formed by an antecedent magma (Figure 6.2) (Streck & Wacaster, 2006; Kilgour *et al.*, 2013). This interpretation is also supported by the group 2 melt inclusions being geochemically similar to glass analyses from earlier eruptions as opposed to 1975 groundmass glass and ash analyses (Figure 5.8).

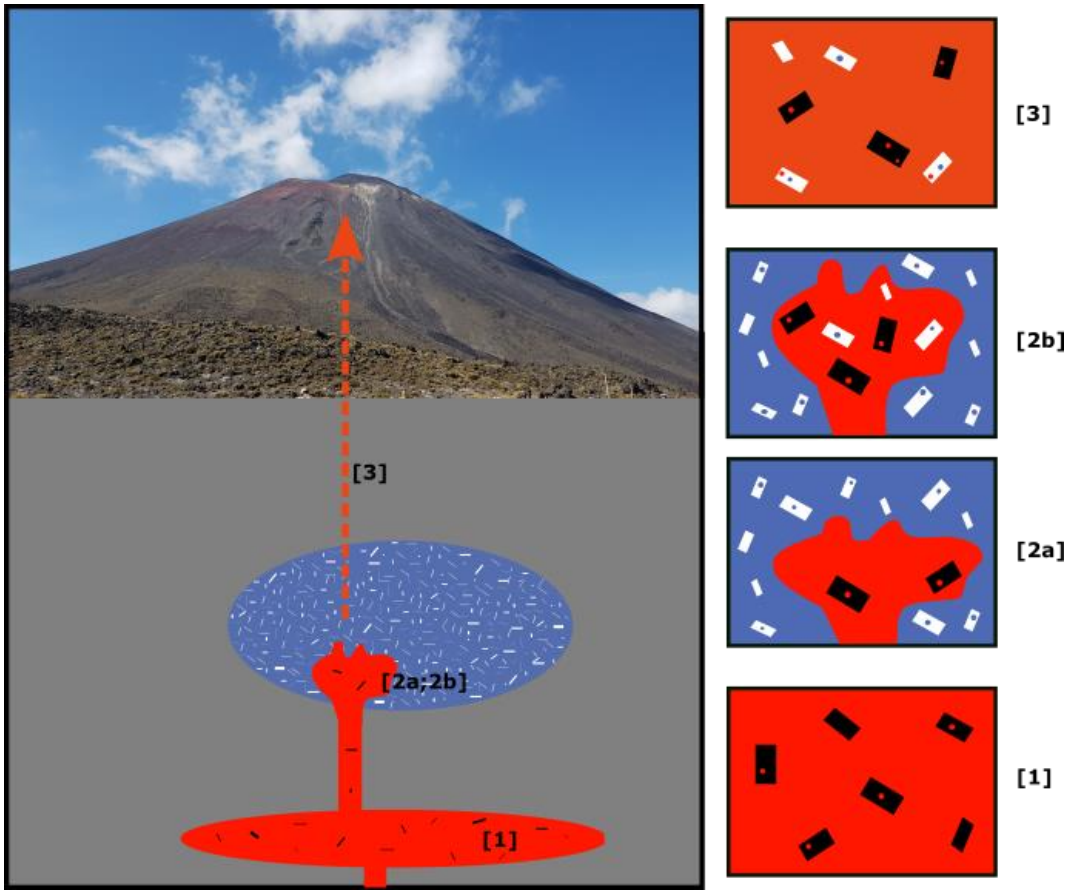

Figure 6.2 Basic conceptual model illustrating an open-system interaction that occurred during the evolution of the magma involved in the climactic 1974-75 eruptions of Ngauruhoe (based on groundmass glass and crystal-hosted melt inclusion analyses). [1] New (high temperature, crystal-poor, less evolved) magma. Melt inclusions trapped in individual crystals record magmatic conditions of the new melt. [2a] The new magma ascends and intrudes into a cold, crystal-rich, more evolved crystal mush zone. [2b] Upon interaction with the crystal mush zone, the new magma entrains some of the exotic crystals. Melt inclusions associated with these crystals record the magmatic conditions of the earlier melt. [3] Final eruptible magma contains phenocryst-hosted melt inclusions which record magmatic conditions of the new melt, as well as antecryst-hosted inclusions which record magmatic conditions of the previous melt (genetically linked to historical eruptions). Some exotic crystals also contain melt inclusions that were entrapped after being entrained in the new melt.

6.4 1975 Shallow Magma Priming

The processes discussed here are related to priming of the magma involved in the 1975 eruptive activity (including the climactic 19th of February eruption).

6.4.1 Vesiculation, Degassing, and Coalescence

Volatile exsolution and transport within the conduit is one of the key physical controls on the resulting style of eruption (Polacci *et al.*, 2009a). Exsolved volatiles are recorded in volcanic rocks as vesicles; therefore, quantitative and textural studies of clast vesicles from the 1975 eruption can provide information about magma rise, vesiculation, and the dynamics of gas transport in the shallow conduit.

Implications regarding eruptive behaviour associated with this event can also be drawn from vesicularity studies.

The 1975 inner crater rim deposit is composed of two distinct non-coalesced clast types based on a bimodal distribution in vesicularity (Figure 4.31). The vesicular scoria clasts (with bulk vesicularities ranging from ~50-85%) are derived from juvenile magma and can thus provide evidence for the shallow magma priming mechanisms associated with the 1975 eruption. In contrast, the dense, poorly vesicular clasts have bulk vesicularities typically ranging from ~5-40%, indicating that they have undergone significant degassing due to cooling and solidification of either the upper crust of juvenile magma or a non-juvenile cap rock. Further evidence regarding the origin of these dense clasts is provided in sections 6.5 and 6.6.

Hand sample and petrographic observations, SEM imagery, and gas-pycnometry studies provide abundant evidence for the interconnected nature of vesicles in the 1975 clasts; scoria clasts contain 40-60% connected vesicles. As similarly interpreted for scoria from Stromboli (Burton *et al.*, 2007; Polacci *et al.*, 2009b), these large and connected vesicles indicate efficient gas segregation and transport to the surface along preferential percolation pathways. This process is not uncommon in low viscosity magmas with low to moderate ascent rates, as gas segregation can occur readily and the resultant bubbles have time to migrate, expand, and coalesce (Herd & Pinkerton, 1997; Taddeucci *et al.*, 2015). Efficient degassing in an unplugged conduit typically leads to either fire-fountaining or mildly explosive Strombolian activity (Vergniolle & Mangan, 2000; Burgisser & Degruyter, 2015; Taddeucci *et al.*, 2015). However, the presence of a coherent caprock can lead to bubble accumulation and coalescence in the underlying magma, which can result in more explosive eruptions (Clarke *et al.*, 2015). This was probably an important factor leading to the climactic 19th February 1975 eruption. Further discussion about the likely fragmentation processes that occurred during 1975 is presented in section 6.5, with regards to eye-witness accounts of eruption activity, and evidence from the inner crater rim deposit.

Bubble coalescence occurs when sufficient bubble volume fractions lead to the thinning and collapse of bounding melt films. Surface tension usually results in subsequent retraction/relaxation and the formation of a single larger bubble (Herd & Pinkerton, 1997; Cashman & Scheu, 2015). Abundant, irregularly shaped vesicles were observed in thin sections of scoria from the 1975 eruption, most likely resulting from the partial collapse of bubble walls between the main vesicle cavities (Figure 4.29). However, the bubble's ability to attain a spherical form may also be limited by the abundant groundmass microlites. This observation, in addition to the lack of spherical vesicles, suggests that there may have been insufficient time for bubble wall retraction to form spherical vesicles following coalescence (i.e. bubble coalescence occurred not long before the 1975 eruption).

6.4.2 Magmatic Temperature

The magma primed for eruption in 1975 likely had a temperature of somewhere between 1018-1114 (±56) °C, based on equilibrium clinopyroxene-liquid geothermometry of black scoria clasts (refer to section 5.5). This temperature is relatively comparable to other temperature estimates for Ngauruhoe. For example, Barton (2011) calculated magma temperatures ranging from 1032-1064 ° C for all historic lava flows using the two-pyroxene geothermometer from Putirka (2008).

Basaltic-andesites produced from other volcanoes globally are also associated with comparable temperature estimates to the 1975 eruptible magma. For example, basaltic-andesite lavas from the western Mexican volcanic belt are likely associated with magmatic temperatures ranging from 1000-1150 °C (Moore & Carmichael, 1998). Magmatic temperature estimates of ~1016 °C and ~1087 °C have been provided for basaltic-andesites from the Farallón Negro Volcanic Complex in Argentina and Villarrica Volcano in Chile, respectively (based on a Mg-exchange thermometer combined with a recent model for hydrous silicate melts) (Sun & Liang, 2017). Basaltic-andesite flows from Arenal Volcano in Costa Rica are also associated with a temperature estimate ranging from 1000–1100 °C (Cigolini, 1998).

These magmatic temperatures contrast to rhyolitic magmas which are often lower. Some examples include rhyolites in the central and western Snake River Plain, Idaho, which have magmatic temperature estimates ranging from 850-1000 °C (Honjo *et al.*, 1992), and rhyolites and pumices of the Pleistocene-Recent central volcanic region of New Zealand which have magmatic temperature range estimates of 735–780 °C and 860–890 °C, respectively (based on titanomagnetite-ilmenite pairs) (Ewart *et al.*, 1971).

6.5 1975 Fragmentation Processes and Eruptive Activity

Vulcanian eruptions are typically associated with magmas of intermediate composition (Clarke *et al.*, 2015). They are short-lived volcanic outbursts, lasting on the order of seconds to minutes, and are small to moderate in scale, potentially ejecting pyroclasts to heights of >20 m (Morrisey & Mastin, 2000). Vulcanian eruptions are characterised by loud, discrete, intermittent explosions, often accompanied by a dark eruption cloud and atmospheric shock waves (Morrisey & Mastin, 2000; Clarke *et al.*, 2015). According to Nairn *et al.* (1976), vulcanian activity dominated during commencement of the 1975 Ngauruhoe eruptions. Similar activity has been documented in several volcanoes worldwide including Sakurajima, Japan (since 1955), Irazu, Costa Rica (1963-1966), Galeras volcano, Colombia (1992-1993), Karymsky, Russia (1970-1992 and the beginning of the 1996 eruption), and Vulcano, Aeolian Islands (Stix *et al.*, 1997; Johnson *et al.*, 1998; Zobin & Levina, 1998; Morrisey & Mastin, 2000; Vergniolle & Mangan, 2000; Watt *et al.*, 2007; Clarke *et al.*, 2015).

The explosive nature of vulcanian eruptions is attributed to the brittle fracturing of a degassed and solidified magma plug above a magmatic conduit in response to two common mechanisms: 1) magma interaction with ground water or hydrothermal fluids (i.e. phreatomagmatic mechanism), or 2) exsolution and accumulation of volatiles as pressurised gas bubbles in magma underlying the cap rock (i.e. magmatic mechanism) (Clarke *et al.*, 2015). These two mechanisms are discussed and illustrated by Woods (1995) and Platz *et al.* (2007), respectively.

Vulcanian eruptions initiated by phreatomagmatic processes involve the buoyant accumulation of vaporised external water and exsolved volatiles below a cap rock

plugging the vent (Woods 1995). Explosive vulcanian activity may occur if this two-phase (magma-volatile) foam layer undergoes rapid decompression and expansion in response to disruption of the cap rock (Woods, 1995). In contrast, vulcanian eruptions caused solely by magmatic mechanisms are associated with the exsolution of volatiles from a crystallizing magma below a coherent and degassed cap rock. Bubble coalescence and the accumulation of pressurised gas bubbles can lead to overpressure in the conduit, resulting in mechanical failure of the plug. A violent eruption is initiated upon plug disruption due to the propagation of a decompression wave into the conduit, causing rapid expansion and fragmentation of the magma (Platz *et al.*, 2007; Clarke *et al.*, 2015). Experimental fragmentation of dome cores (Kennedy *et al.*, 2005; Mueller *et al.*, 2005), show similar processes of fragmentation and this is a plausible mechanism to explain the 1975 eruption of Ngauruhoe.

Nairn and Self (1978) suggested that explosions from Ngauruhoe during 1975 were largely driven by phreatic steam (i.e. similar to the model proposed by Woods, 1995). This proposal is based on a plume of white steam which appeared through the centre of the eruption column during the 19th February 1975 eruption (Nairn & Self, 1978). However, the 1975 inner crater rim deposit does not display any accretionary lapilli or quenching textures indicative of magma-water interactions. This deposit and ash from 1974 and 1975 also lack country rock fragments, which are normally abundant in pyroclastic material produced from phreatomagmatic eruptions (Clarke *et al.*, 2015). The lack of field evidence to support the involvement of water suggests that magmatic processes as illustrated by Platz *et al.* (2007) are more likely to be the dominant cause for the explosive activity that occurred during 1975. Minor magma-water interaction may have occurred in conjunction with magmatic processes to produce the steam observed in the eruption column.

The presence of sub-angular to angular dense lapilli throughout the 1975 inner crater rim deposit, and the higher proportion of these clasts in facies A, supports the brittle disruption of a cap rock upon commencement of this eruption (Taddeucci *et al.*, 2015). The cap rock was likely comprised of a solid plug from the 1954-55 eruptions, as well as any recycled material and crater collapse debris from

subsequent, less explosive activity in the late 1960's, 1972, and 1973 (Nairn *et al.*, 1976). The quiet years leading up to the climactic 1975 eruption would have allowed for this material to form a coherent, solidified, and degassed cap rock; resulting in a highly pressurised magma system below due to the exsolution and accumulation of volatiles as pressurised gas bubbles (Clarke *et al.*, 2015). There are several other volcanoes where a similar process has accounted for the transition from strombolian to more explosive vulcanian activity. Some examples include the final stages of the 1954-55 Ngauruhoe eruption (Krippner, 2009), the AD1655 Taranaki eruption (Platz *et al.*, 2007), and the 2002-2003 eruptions from Stromboli Volcano in Italy (Harris *et al.*, 2008).

Following these earlier vulcanian eruptions, the largest volume of pyroclastic material was erupted on the 19th February 1975, during 1.5 hours of vigorous gas-streaming (Nairn & Self, 1978). Lube *et al.* (2007) referred to this as a subplinian phase due to the continuous and large volume of ash emission, which resulted in a sustained eruption column to 8 km above the summit. As discussed above, this eruption is unlikely to have resulted primarily from water-magma interaction (as suggested by Nairn, 1978) due to the lack of field evidence. Therefore, the continuous nature of this climactic event may be due to the earlier presence of a cap rock allowing significant gas build-up in the underlying magma, of which a large fraction still needed to be released following the earlier vent clearing eruptions. Some highly vesicular black scoria clasts from facies A and B contain thin vesicle walls, providing evidence for the involvement of a very gas-rich magma with tightly packed bubbles (Figure 4.30) (Herd & Pinkerton, 1997). Due to the high explosivity and extensive fragmentation associated with such an eruption, most of the erupted material would likely have been deposited as a distal ash deposit and is unlikely to have contributed much to building up the inner crater rim (Cioni *et al.*, 2015).

There are, however, eye-witness accounts of incandescent ejecta being visible at the base of the large 'subplinian' eruption plume (Figure 6.3) (Nairn, 1976; Williams, 1989; Lube *et al.*, 2007). The higher abundance of scoria and spatter in facies C and D compared to the underlying facies (Figure 3.6) may be indicative of a transition in eruption style. The componentry of these facies is consistent with a

spatter-fed eruption, suggesting that they may have been mostly emplaced during strombolian fire-fountaining activity associated with the continuous (1.5-hour) eruption on the 19th February 1975. Emplacement processes are discussed in section 6.7.

Figure 6.3 Fire-fountaining activity observed at the base of the large continuous eruption plume produced on the 19th February 1975. Photo by Herb Spannagl, in Williams (1989).

A simple model relating different eruption styles to varying two-phase flow regimes is provided by Vergniolle and Mangan (2000) (Figure 6.4); and is summarised below.

- Effusive activity is typically associated with “bubbly flow” in magmas (i.e. melt containing small discrete bubbles in suspension), which occurs at gas contents less than 30% (Vergniolle & Mangan, 2000).

- Pulsatory and mildly explosive strombolian eruptions occur when large over-pressured gas slugs burst at the magma surface (Vergniolle & Mangan, 2000;

Parfitt, 2004; Houghton & Gonnermann, 2008; Taddeucci *et al.*, 2015). Two-phase slug flow (Figure 6.4) is therefore a key process accompanying strombolian eruptions, and typically occurs when gas contents are ~70% (Vergniolle & Mangan, 2000; Houghton & Gonnermann, 2008). There are two models which explain the formation of gas slugs; one suggests that they form dynamically during ascent through the conduit due to bubble coalescence and high bubble rise velocities relative to magma ascent rates (Wilson & Head III, 1981; Parfitt & Wilson, 1995; Parfitt, 2004), while the other model suggests that gas slugs form by foam collapse at the boundary between the magma chamber and conduit (Vergniolle & Jaupart, 1986; Jaupart & Vergniolle, 1988, 1989; Vergniolle & Jaupart, 1990).

- Fire-fountaining and subplinian activity typically result from either annular flow (gas volume fractions >70%) or dispersed flow (gas volume fractions substantially larger than 70%) (Figure 6.4). The former is typically associated with the development of a foam at the roof of a shallow magma chamber due to bubble accumulation and coalescence. Collapse of this foam results in annular two-phase flow up the conduit (i.e. a central gas jet surrounded by magma along the conduit walls), and the ensuing sustained jetting of gas and fluidal pyroclasts (Vergniolle & Jaupart, 1986; Jaupart & Vergniolle, 1988, 1989; Vergniolle & Jaupart, 1990; Vergniolle & Mangan, 2000).

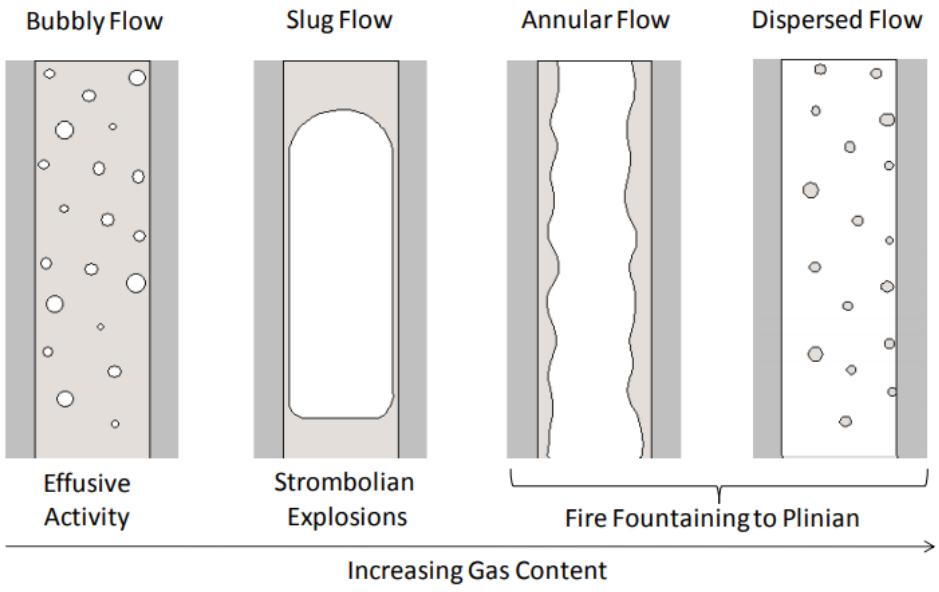

Figure 6.4 The two-phase flow regimes that give rise to different styles of activity. Diagram from Krippner (2009), modified from Vergniolle and Mangan (2000).

The complex hybrid nature of eruption styles involved during the eruption on the 19th February 1975 suggests that these simple models may not necessarily be applicable in this case (i.e. slug flow, annular flow, and dispersed flow cannot operate at the same time). The highly voluminous and continuous 'subplinian' eruption does, however, indicate that the magma was probably gas-rich to sustain such an explosive eruption for 1.5 hours (Vergniolle & Mangan, 2000; Cioni *et al.*, 2015). This is supported by vesicularity data ranging from 50-70% for most of the 1975 scoria clasts, in addition to a few clasts with very high vesicularities of 72% and 80%, which is consistent with the suggestion by Cioni *et al.* (2015) that the bulk vesicularity of subplinian juvenile fragments can range from 10 up to 80% within a single eruption. The 1.5-hour event was followed by a series of violently explosive vulcanian explosions accompanied by visible air shock waves and large volcanic earthquakes (Nairn & Self, 1978; Lube *et al.*, 2007). It is therefore possible that some scoria in the upper portion of facies D may have also been emplaced during these subsequent eruptions.

6.6 Degassing and Cooling Processes

The groundmass textures of different emplacement products within the 1975 inner crater rim deposit provide information about their cooling history. Crystallization of anhydrous phases, particularly plagioclase, is promoted by the exsolution of water that occurs in response to pressure reduction during magma ascent (resulting in a corresponding shift in the liquidus) (Clarke *et al.*, 2015). Crystallization, degassing and continued cooling at shallow levels induce further crystallization by increasing magma viscosity and concentrating volatiles in the remaining melt. The dense clasts from the 1975 Ngauruhoe eruption display a highly crystalline, plagioclase-dominated groundmass which can be attributed to shallow degassing, suggesting that they are probably derived from a dense, degassed, cap rock. In contrast, the scoria clasts contain portions of relatively microlite-poor glass (melt) between the groundmass crystals (i.e. they are less crystalline than the dense clasts), indicating that they were erupted quickly and thus rapidly cooled and quenched prior to emplacement (Vergniolle & Mangan, 2000). Spatter clasts, on the other hand, have undergone limited cooling prior to

deposition, leading to deformation and agglutination upon landing (see section 6.7.1).

Chemical changes associated with post-emplacement cooling may also provide an alternative explanation for the silica-rich population of melt inclusions identified in the 1975 crater rim deposit. The more evolved melt inclusions are typically hosted in dense clasts (Appendix 9b), which is not surprising since these inclusions would continue to crystallise along their interface with the host crystal (Kilgour *et al.*, 2013). The melt inclusions analysed were mostly glassy which may suggest that water diffusion was limited (i.e. due to a weak gradient associated with the H_2O-poor melt inclusions) and that edge crystallisation dominates.

6.7 Emplacement Processes on the Crater Rim

This section discusses emplacement processes on the crater rim; however, it is important to note that other emplacement processes were simultaneously occurring elsewhere (e.g. flank block and ash flows and distal ash fallout) but are not within the scope of this study.

6.7.1 Spatter Deposition and Variations in Viscous Sintering

Basaltic fire fountaining often results in spatter deposits; the accumulation of hot, fluid, juvenile pyroclasts which may preserve enough heat to agglutinate upon landing (Wolff & Sumner, 2000; Sumner *et al.*, 2005). Agglutination is defined as the almost instantaneous deformation and adhesion of pyroclasts upon deposition due to their own momentum (Wolff & Sumner, 2000; Houghton & Carey, 2015). In contrast, welding refers to the post depositional sintering, flattening and adhesion of hot, plastic, pyroclastic fall material. This process is assisted by the load pressure of overlying tephra, and often results in a cohesive deposit associated with viscous pore collapse and a non-linear increase in strength (Wolff & Sumner, 2000; Carey *et al.*, 2008; Vasseur *et al.*, 2013). According to Sumner *et al.* (2005), the rate of accumulation and the rate (and amount) of cooling are the most important controls on the degree of agglutination and welding in strombolian/fire-fountaining deposits (Figure 6.5). Other factors which affect the heat of individual clasts and can thus influence the occurrence and degree of welding include clast flight time and grain size (Thomas & Sparks, 1992;

Capaccioni & Cuccoli, 2005; Vasseur *et al.*, 2013; Houghton & Carey, 2015). In the case of the Ngauruhoe crater rim deposit, these factors do not vary significantly so their influence is probably negligible.

Facies A and B of the inner crater rim deposit are predominantly comprised of loose clasts, which could imply that the clasts were ejected high and cooled quickly. The absence of welding could also be attributed to a low accumulation rate associated with weak ejections and small amounts of magma being erupted as scoria (Clarke *et al.*, 2015). In this scenario, pyroclasts from the first ejection would have landed on previously cooled material (deposited by an earlier eruption), thus cooling quickly instead of welding together (Figure 6.5). It is therefore unlikely that facies A and B were deposited during the 1.5-hour 'subplinian' eruption on the 19th February 1975, as the continuous nature of this event would have favoured high deposit temperatures and load pressures (Houghton & Carey, 2015). It seems more feasible that they were emplaced during discrete, less continuous vulcanian activity leading up to this climactic eruption.

In contrast, facies C and D of the inner crater rim deposit are both spatter-rich deposits, likely emplaced from fire-fountaining/strombolian activity associated with the large continuous eruption plume on the 19th February 1975 (as discussed in section 6.5). Spatter agglutination and welding in these facies was probably assisted by the continuous nature of this eruption, as this would contribute to a low rate of cooling (Figure 6.5).

Facies C contains a large proportion of densely welded/coherent domains (~51%) compared to the rest of the deposit, suggesting that rapid spatter accumulation was likely involved during its emplacement (high accumulation rates lead to high deposit temperatures and load pressures which favour welding) (Sparks & Wright, 1979; Head & Wilson, 1989; Wolff & Sumner, 2000; Capaccioni & Cuccoli, 2005; Sumner *et al.*, 2005; Vasseur *et al.*, 2013). However, it is important to note that the degree of welding is laterally and vertically variable throughout facies C (components range from individual and weakly agglutinated clasts to densely welded/coherent units), which might be indicative of fluctuations in accumulation rates.

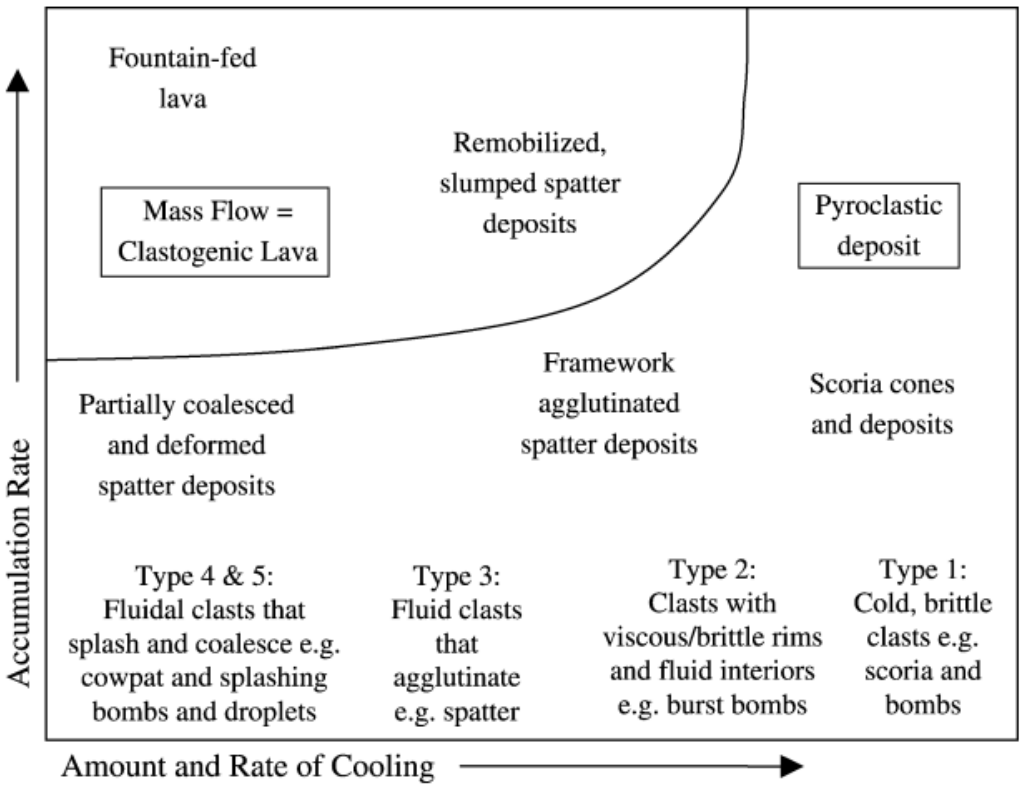

Figure 6.5 Accumulation rate and cooling rate are important factors influencing the degree of welding in strombolian fire fountain deposits. The 1975 inner crater rim deposit of Ngauruhoe displays a wide range in the degree of welding and includes cold, brittle scoriaceous clasts, agglutinated spatter, and partially coalesced and deformed spatter deposits (Sumner *et al.*, 2005).

Flattened and deformed, grey/black-coloured scoria were also observed within some of the dense coalesced units in facies C. This indicates that scoria lapilli of varying temperature came into contact with hotter, more fluidal material and were subsequently compressed, deformed and elongated (i.e. the clasts were not fluidal enough to form a homogenous liquid) (Sumner, 1998). This may be due to some scoria clasts coming from the lower temperature region of fire fountain, which are more likely to have a lower initial temperature compared to clasts transported in the denser and higher temperature region (Houghton & Carey, 2015).

Following the emplacement of facies C, it appears that the accumulation rate may have decreased, suggested by the mixture of individual clasts and spatter bombs (but lack of large cohesive units) throughout facies D (Figure 6.5).

6.7.2 Physical Abrasion

Campbell *et al.* (2013) suggests that "milling" of clasts in volcanic conduits during explosive eruptions can involve both mechanical processes related to physical contact between clasts or wall rocks, and thermal processes linked to intense heat within the conduit. Facies D of the 1975 crater rim deposit contains more spherical dense clasts compared to the underlying facies. These clasts are considered non-juvenile due to similarities in colour and texture to the angular to sub-rounded dense lapilli. Based on this interpretation, it is reasonable to suggest that these clasts were milled around in the vent and abraded prior to their emplacement.

This process has been invoked in other eruptions, such as the 2360 B.P. subplinian eruption of Mount Meager (British Columbia), based on the presence of rounded lithic clasts within the pyroclastic fallout deposits (Campbell *et al.*, 2013). The high degree of rounding associated with the largest lithics in the Kaingaroa ignimbrites has also been attributed to repeated fall back and milling in the vent(s) by Nairn *et al.* (1994). As many of the dense rounded clasts in facies D are relatively larger compared to the less rounded clasts, this is consistent with Campbell *et al.* (2013) who found the extent of surface rounding to be proportional to clast residence times within the conduit (since larger and denser clasts are typically associated with higher residence times).

6.8 Application to Understanding the Volcanic Hazard

Volcanic arc (subduction zone) systems can be highly complex and involve a wide range of processes prior to the eruption of associated magmas. It is important to understand these processes as best we can, particularly considering the vast majority of global volcanism is associated with volcanic arcs (Deligne & Sigurdsson, 2015) and eruptions from these volcanoes can be hazardous. Some of the most well-known examples of eruptions which results in thousands of fatalities include the 1883 eruption of Krakatau (Indonesia) and the 1902 eruption of Mt Pelée (Martinique) (Tanguy *et al.*, 1998). Although Ngauruhoe is not in close proximity to any highly populated centres, this research still has significant implications to the safety of hundreds of people walking the Tongariro Alpine Crossing each day. In 2014 it was reported that daily visitor numbers to the crossing could reach up

to 1500 during the busiest summer period (Jolly *et al.*, 2014c), and this number has likely increased substantially over the past five years.

This study has provided improved knowledge regarding magmatic and volcanic processes (including magma evolution and ascent, priming conditions, triggers and eruption mechanisms) likely associated with the 1975 eruptions from Ngauruhoe. It is hoped that this improved understanding will assist with more reliable interpretation of monitoring data prior to and during such eruptions (not only associated with Ngauruhoe, but also to basaltic-andesite volcanoes worldwide).

Chapter Seven

Conclusions and Future Work

7.1.1 Conclusions

Ngauruhoe is a young (~7 ka), basaltic-andesite to andesite, composite cone and is the largest and one of the most active vents of the larger Tongariro Volcanic Complex. The summit of Ngauruhoe consists of two craters; an older crater with a diameter of c. 400 m, and an active summit scoria cone (c. 150 m wide) which was constructed in the northwest sector of the original crater during the eruptions of 1954 to 1975. The last significant eruption of 1975 added ~9 m of scoria and ash to the inner crater rim.

This project has provided insight into the pre-eruptive conditions and processes that led to the eruption and emplacement of the 1975 inner crater rim deposit. The main conclusions from this study are summarised below.

- There is sufficient evidence for crystal fractionation and magma mixing processes being involved in the evolution of the magma that erupted during 1975. In particular, the presence of more evolved melt inclusions (c.f. groundmass glass) may suggest that the transporting magma interacted with, and entrained, exotic crystals from a cooler, more evolved crystal mush zone formed by an antecedent magma.

- The 1975 eruption is geochemically different to earlier eruptions, particularly those which occurred in 1954, 1968, and 1972 (the earlier eruptions appear to be associated with a more evolved melt). Some very high silica contents in glass from earlier eruptions may be associated with hydrothermal alteration and/or halogen degassing and the formation of cristobalite.

- The high abundance of lithics in the 1972 ash suggests that this eruption involved conduit wall degassing, or simply strong degassing, that mined some of the plug/hydrothermally altered rock (perhaps in the restricted

extent of the hydrothermal system). The lithics may be derived from the brittle fragmentation of a degassed and hydrothermally altered plug from earlier 1954-55 eruptions, and at least some of the lithics may also be derived from older pre-1954 wall rock. No clear evidence for the involvement of a fresh magmatic component was found.

- Evidence for the involvement of a fresh magmatic component was identified in ash samples following and including the 7th of December 1973 eruption, which is consistent with findings from Cole & Nairn (1975) and Nairn & Self (1978). However, stereoscopic observations and shape analyses of ash from the 16th October 1973 eruption display evidence for a potentially minor contribution of fresh magma during this eruption (c.f. Nairn *et al.,* 1976 who did not find any evidence).

- Vesicularity studies indicate that efficient gas segregation and transport to the surface along preferential percolation pathways was a key process involved in priming the magma for the 1975 eruption. Based on equilibrium clinopyroxene-liquid geothermometry, the eruptible magma likely had a temperature of 1018-1114 (±56) °C.

- The presence of a coherent, degassed, and hydrothermally altered caprock contributed to the high explosivity of the climactic eruption which took place on the 19th of February 1975. This cap rock may have been a solidified cap on the juvenile magma, and/or a plug consisting of solidified non-juvenile magma from the 1954-55 eruption as well as any recycled material and crater collapse debris from subsequent, less explosive activity in the late 1960's, 1972, and 1973. Whatever the origin, this cap rock led to the accumulation and coalescence of pressurised gas, resulting in overpressure in the conduit and subsequent mechanical failure of the plug. A violent vulcanian eruption was initiated upon plug disruption and was followed by a voluminous and continuous eruption plume lasting 1.5 hours due to the significant amount of gas that had built up beneath the cap rock.

- It is unlikely that the 1974-75 eruption was primarily triggered by a phreatomagmatic event, as suggested by Nairn & Self (1978), due to the lack of evidence displayed in the crater rim deposit. It is more feasible that the primary eruption mechanism was dominantly magmatic, with only minor magma-water interaction producing the steam observed in the eruption column.

- The 1975 inner crater rim is comprised of three different clast types which vary in terms of origin and cooling processes. The moderately vesicular scoria and fluidal spatter are both derived from the juvenile magma; scoria clasts erupted quickly and thus rapidly cooled and quenched prior to emplacement, whereas spatter clasts have undergone limited cooling prior to deposition, leading to deformation and agglutination upon landing. The sub-angular to angular dense clasts are derived from a solidified and degassed cap rock and were thus solid upon emplacement.

- Two populations of melt inclusions are recorded in the 1975 deposit. The unusually evolved population are typically hosted in dense clasts, possibly related to post-entrapment crystallisation during slow cooling (these inclusions likely continued to crystallise along their interface with the host crystal).

The 1975 inner crater rim deposit has been divided into four facies (A through D) based on textural characteristics and componentry. Interpretations regarding these facies and their relationship to eruptive processes and behaviour during this period, are based on deposit characteristics and eye-witness accounts. The main interpretations are summarised below.

- Facies A and B were most likely emplaced during discrete vulcanian activity associated with disruption of a caprock, leading up to the climactic eruption on the 19th February 1975. This is consistent with the presence of loose clasts, and the higher proportion of dense clasts in facies A relative to the overlying facies.

- Facies C and D were most likely deposited during the continuous 1.5 hour 'subplinian' eruption on the 19th February 1975 (from strombolian fire-fountaining activity at the base of large eruption plume). This is suggested by the mixture of scoria, agglutinated spatter, and dense clasts throughout these facies; which are indicative of a spatter-fed eruption. The densely welded domains within facies C suggest the involvement of a higher accumulation rate compared to that involved during the emplacement of facies D.

7.1.2 Future Work

Further work on Ngauruhoe could involve constraining the likely depth of melts and dykes associated with the 1975 eruption, based on volatile contents of phenocryst-hosted melt inclusions. There are a few ways in which probing transects across a crystal could also provide some useful information; 1) assuming that there is a well constrained experimental phase diagram, a transect could show how compositional changes reflect pressure or temperature dependence, and 2) a low pressure signature associated with decompression may be recorded in small zones near the rim, since the partition of trace elements between the melt and the crystal is partly pressure dependant. Plagioclase crystals from Mount St. Helens vary in composition due to being transported from depth into the cryptodome, and thus provide a good example (Berlo *et al.*, 2007).

The key factors that influence the ability of a magma to transport xenoliths to the surface include xenolith size and density, and the ascent velocity of the magma (Spera, 1984; Rutherford *et al.*, 2000). Therefore, by using the settling velocity of quartz-rich xenoliths, combined with knowledge of the viscosity and density of the magma, it may be possible to work out a minimum ascent velocity required to keep the xenoliths from settling. This calculation could have several applications from a geological/petrological perspective, such as developing a conduit flow model and assisting with future monitoring of Ngauruhoe.

It may also be useful to obtain strontium (Sr) and/or oxygen (O) isotope data from mineral zones. Combining elemental zoning with Sr isotopic variations in plagioclase may help assess the extent of crustal contamination involved in the

evolution of the 1975 magma, and may also help identify the occurrence of magmatic recharge events (Sas *et al.*, 2019). Oxygen isotope ratios within various minerals are also useful for providing evidence for crustal contamination since crustal materials typically have elevated ^{18}O compared to mantle-derived magmas (e.g. Baker *et al.*, 2000; Troll *et al.*, 2013).

References

Alcaraz, S., Rattenbury, M., Soengkono, S., Bignall, G., & Lane, R. (2012). A 3D multi-disciplinary interpretation of the basement of the Taupo Volcanic Zone, New Zealand. In *Proceedings, 37th workshop on geothermal reservoir engineering*. Stanford, CA.

Allen, L. (1948). Activity at Ngauruhoe, April-May, 1948: New Zealand. *Science & Technology, 30*(3), 187-193.

Allen, L. (1949). The eruption of Ngauruhoe, February-March, 1949. *New Zealand Science Review, 7*(10), 180-183.

Arpa, M. C., Zellmer, G. F., Christenson, B., Lube, G., & Shellnutt, G. (2017). Variable magma reservoir depths for Tongariro Volcanic Complex eruptive deposits from 10,000 years to present. *Bulletin of Volcanology, 79*(7), 56.

Baker, J. A., Macpherson, C. G., Menzies, M. A., Thirlwall, M. F., Al-Kadasi, M., & Mattey, D. P. (2000). Resolving crustal and mantle contributions to continental flood volcanism, Yemen; constraints from mineral oxygen isotope data. *Journal of Petrology, 41*(12), 1805-1820.

Bardsley, C. J. (2004). *Physical Volcanology of Red Crater, Tongariro.* MSc thesis, University of Waikato, Hamilton.

Barton, S. J. (2011). *Crystal Forensics of Historical Lava Flows from Mt Ngauruhoe.* MSc thesis, University of Victoria, Wellington.

Basher, R. (2005). *Physical Volcanology and Future Volcanic Risk from Te Maari Craters, Tongariro.* MSc thesis, University of Waikato, Hamilton.

Battey, M. (1949). The recent eruption of Ngauruhoe. *Records of the Auckland Institute and Museum*, 387-395.

Bebbington, M., & Lai, C. (1996). Statistical analysis of New Zealand volcanic occurrence data. *Journal of Volcanology and Geothermal Research, 74*(1-2), 101-110.

Bédard, J. H. (2010). Parameterization of the Fe = Mg exchange coefficient (Kd) between clinopyroxene and silicate melts. *Chemical Geology, 274*(3), 169-176.

Beetham, R., & Watters, W. (1985). Geology of Torlesse and Waipapa terrane basement rocks encountered during the Tongariro power development project, North Island, New Zealand. *New Zealand Journal of Geology and Geophysics, 28*(4), 575-594.

Berlo, K., Blundy, J., Turner, S., & Hawkesworth, C. (2007). Textural and chemical variation in plagioclase phenocrysts from the 1980 eruptions of Mount St. Helens, USA. *Contributions to Mineralogy and Petrology, 154*(3), 291-308.

Bibby, H. M., Caldwell, T. G., Davey, F. J., & Webb, T. H. (1995). Geophysical evidence on the structure of the Taupo Volcanic Zone and its hydrothermal circulation. *Journal of Volcanology and Geothermal Research, 68*(1), 29-58.

Bibby, H. M., Risk, G. F., & Caldwell, T. G. (2002). Long offset tensor apparent resistivity surveys of the Taupo Volcanic Zone, New Zealand. *Journal of Applied Geophysics, 49*(1), 17-32.

Bidwill, J. C. (1841). *Rambles in New Zealand*. (1st ed.). Orr, London.

Blundy, J., & Cashman, K. (2001). Ascent-driven crystallisation of dacite magmas at Mount St Helens, 1980–1986. *Contributions to Mineralogy and Petrology, 140*(6), 631-650.

Boudon, G., Villemant, B., Komorowski, J. C., Ildefonse, P., & Semet, M. P. (1998). The hydrothermal system at Soufriere Hills Volcano, Montserrat (West Indies): Characterization and role in the on-going eruption. *Geophysical Research Letters, 25*(19), 3693-3696.

Breard, E., Lube, G., Cronin, S., Fitzgerald, R., Kennedy, B., Scheu, B., Montanaro, C., White, J., Tost, M., & Procter, J. (2014). Using the spatial distribution and lithology of ballistic blocks to interpret eruption sequence and dynamics: August 6 2012 Upper Te Maari eruption, New Zealand. *Journal of Volcanology and Geothermal Research, 286*, 373-386.

Briggs, R. M. (1981). *Geological Society of New Zealand 1981 Conference, Hamilton: field excursions guide book*. International Inter-INQUA Field Conference and Workshop on Tephrochronology, Loess, and Paleopedology. Hamilton, N.Z.: Geological Society of New Zealand.

Burgisser, A., & Degruyter, W. (2015). Magma ascent and degassing at shallow levels. In *The Encyclopedia of Volcanoes* (pp. 225-236). Elsevier.

Burton, M., Mader, H., & Polacci, M. (2007). The role of gas percolation in quiescent degassing of persistently active basaltic volcanoes. *Earth and Planetary Science Letters, 264*(1-2), 46-60.

Campbell, M. E., Russell, J. K., & Porritt, L. A. (2013). Thermomechanical milling of accessory lithics in volcanic conduits. *Earth and Planetary Science Letters, 377*, 276-286.

Capaccioni, B., & Cuccoli, F. (2005). Spatter and welded air fall deposits generated by fire-fountaining eruptions: cooling of pyroclasts during transport and deposition. *Journal of Volcanology and Geothermal Research, 145*(3-4), 263-280.

Carey, R., Houghton, B., & Thordarson, T. (2008). Contrasting styles of welding observed in the proximal Askja 1875 eruption deposits II: local welding. *Journal of Volcanology and Geothermal Research, 171*(1-2), 20-44.

Cashman, K. V., & Giordano, G. (2014). Calderas and magma reservoirs. *Journal of Volcanology and Geothermal Research, 288*, 28-45.

Cashman, K. V., & Scheu, B. (2015). Magmatic fragmentation. In H. Sirgudsson (Ed.), *The Encyclopedia of Volcanoes* (pp. 459-471). Elsevier.

Cashman, K. V., Sparks, R. S. J., & Blundy, J. D. (2017). Vertically extensive and unstable magmatic systems: a unified view of igneous processes. *Science, 355*(6331), eaag3055.

Cassidy, J., Ingham, M., Locke, C. A., & Bibby, H. (2009). Subsurface structure across the axis of the Tongariro Volcanic Centre, New Zealand. *Journal of Volcanology and Geothermal Research, 179*(3), 233-240.

Chizmar, J. M. (2003). *The Nature and Dynamics of Explosive Eruptions and Associated Crater Formation at Tama Lakes, Tongariro Volcano.* MSc thesis, University of Waikato, Hamilton.

Christenson, B., Reyes, A., Young, R., Moebis, A., Sherburn, S., Cole-Baker, J., & Britten, K. (2010). Cyclic processes and factors leading to phreatic eruption events: Insights from the 25 September 2007 eruption through Ruapehu Crater Lake, New Zealand. *Journal of Volcanology and Geothermal Research, 191*(1-2), 15-32.

Cigolini, C. (1998). Intracrustal origin of Arenal basaltic andesite in the light of solid–melt interactions and related compositional buffering. *Journal of Volcanology and Geothermal Research, 86*(1-4), 277-310.

Cioni, R., Pistolesi, M., & Rosi, M. (2015). Plinian and subplinian eruptions. In *The Encyclopedia of Volcanoes* (pp. 519-535). Elsevier.

Clarke, A. B., Esposti Ongaro, T., & Belousov, A. (2015). Chapter 28 - Vulcanian Eruptions. In *The Encyclopedia of Volcanoes* (pp. 505-518). Elsevier Inc.

Cloud, P. E. (1951). The 1949 eruption of Ngauruhoe. *The Scientific Monthly, 72*(4), 241-251.

Cole, J. (1990). Structural control and origin of volcanism in the Taupo Volcanic Zone, New Zealand. *Bulletin of Volcanology, 52*(6), 445-459.

Cole, J. W., & Nairn, I. A. (1975). *Catalogue of the Active Volcanoes of the World including Solfatara Fields. Part 22: New Zealand.* International Association of Volcanology and Chemistry of the Earth's Interior. Rome (Italy).

Cole, J. W. (1978). Andesites of the Tongariro Volcanic Centre, North Island, New Zealand. *Journal of Volcanology and Geothermal Research, 3*(1), 121-153.

Coombs, M. L., & Gardner, J. E. (2004). Reaction rim growth on olivine in silicic melts: Implications for magma mixing. *American Mineralogist, 89*(5-6), 748-758.

Coote, A. C., & Shane, P. (2016). Crystal origins and magmatic system beneath Ngauruhoe Volcano (New Zealand) revealed by plagioclase textures and compositions. *Lithos, 260*, 107-119.

Couch, S., Sparks, R., & Carroll, M. (2001). Mineral disequilibrium in lavas explained by convective self-mixing in open magma chambers. *Nature, 411*(6841), 1037.

Cronin, S., Stewart, C., Zernack, A., Brenna, M., Procter, J., Pardo, N., Christenson, B., Wilson, T., Stewart, R., & Irwin, M. (2014). Volcanic ash leachate compositions and assessment of health and agricultural hazards from 2012 hydrothermal eruptions, Tongariro, New Zealand. *Journal of Volcanology and Geothermal Research, 286*, 233-247.

Crouch, J. F., Pardo, N., & Miller, C. A. (2014). Dual polarisation C-band weather radar imagery of the 6 August 2012 Te Maari eruption, Mount Tongariro, New Zealand. *Journal of Volcanology and Geothermal Research, 286*, 415-436.

de Silva, S., & Lindsay, J. M. (2015). Primary volcanic landforms. In H. Sigurdsson (Ed.), *The Encyclopedia of Volcanoes* (pp. 273-297). Elsevier.

Deligne, N. I., & Sigurdsson, H. (2015). Global rates of volcanism and volcanic episodes. In H. Sirgudsson (Ed.), *The Encyclopedia of Volcanoes* (pp. 265-272). Elsevier.

Eaves, S. (2015). *The Glacial History of Tongariro and Ruapehu Volcanoes, New Zealand.* PhD thesis, University of Victoria, Wellington.

Efford, J. T., Bylsma, R. J., Clarkson, B. D., Pittari, A., Mauriohooho, K., & Moon, V. G. (2014). Vegetation dieback as a proxy for temperature within a wet pyroclastic density current: A novel experiment and observations from the 6th of August 2012 Tongariro eruption. *Journal of Volcanology and Geothermal Research, 286*, 367-372.

Ewart, A., Green, D., Carmichael, I., & Brown, F. (1971). Voluminous low temperature rhyolitic magmas in New Zealand. *Contributions to mineralogy and petrology, 33*(2), 128-144.

Fitzgerald, R., Tsunematsu, K., Kennedy, B., Breard, E., Lube, G., Wilson, T., Jolly, A., Pawson, J., Rosenberg, M., & Cronin, S. (2014). The application of a calibrated 3D ballistic trajectory model to ballistic hazard assessments at Upper Te Maari, Tongariro. *Journal of Volcanology and Geothermal Research, 286*, 248-262.

Fournier, N., & Jolly, A. D. (2014). Detecting complex eruption sequence and directionality from high-rate geodetic observations: The August 6, 2012

Te Maari eruption, Tongariro, New Zealand. *Journal of Volcanology and Geothermal Research, 286*, 387-396.

Gamble, J. A., Smith, I. E., Graham, I. J., Kokelaar, B. P., Cole, J. W., Houghton, B. F., & Wilson, C. J. (1990). The petrology, phase relations and tectonic setting of basalts from the Taupo Volcanic Zone, New Zealand and the Kermadec Island Arc-Havre Trough, SW Pacific. *Journal of Volcanology and Geothermal Research, 43*(1-4), 253-270.

Gill, J. B. (2012). *Orogenic andesites and plate tectonics*. (Vol. 16). Berlin: Springer Science.

Ginibre, C., Wörner, G., & Kronz, A. (2007). Crystal zoning as an archive for magma evolution. *Elements, 3*(4), 261-266.

Godfrey, H. J., Shelley, A., & Savage, M. K. (2014). Search for temporal changes in shear-wave splitting associated with the 2012 Te Maari eruptions at Mount Tongariro, New Zealand. *Journal of Volcanology and Geothermal Research, 286*, 277-293.

Graham, I., & Hackett, W. (1987). Petrology of calc-alkaline lavas from Ruapehu Volcano and related vents, Taupo Volcanic Zone, New Zealand. *Journal of Petrology, 28*(3), 531-567.

Graham, I. J., Grapes, R. H., & Kifle, K. (1988). Buchitic metagreywacke xenoliths from Mount Ngauruhoe, Taupo Volcanic Zone, New Zealand. *Journal of Volcanology and Geothermal Research, 35*(3), 205-216.

Graham, I. J., Cole, J. W., Briggs, R. M., Gamble, J. A., & Smith, I. E. M. (1995). Petrology and petrogenesis of volcanic rocks from the Taupo Volcanic Zone: a review. *Journal of Volcanology and Geothermal Research, 68*(1), 59-87.

Gregg, D. R. (1956). Eruption of Ngauruhoe 1954-1955. *New Zealand Journal of Science and Technology,* (B37), 675-688.

Gregg, D. R. (1960). *The Geology of Tongariro Subdivision*. Wellington, N.Z.: Wellington, N.Z. : Govt. Printer.

Greve, A., Turner, G. M., Conway, C. E., Townsend, D. B., Gamble, J. A., & Leonard, G. S. (2016). Palaeomagnetic refinement of the eruption ages of Holocene lava flows, and implications for the eruptive history of the Tongariro Volcanic Centre, New Zealand. *Geophysical Journal International, 207*(2), 702-718.

Griffin, A. M. (2007). *Products and Processes of Cone-Building Eruptions at North Crater, Tongariro.* MSc thesis, University of Waikato, Hamilton.

Grove, T. L. (2000). Origin of magmas. In H. Sirgudsson (Ed.), *Encyclopedia of Volcanoes* (pp. 133-47). New York: Academic Press.

Hackett, W., & Houghton, B. (1989). A facies model for a Quaternary andesitic composite volcano: Ruapehu, New Zealand. *Bulletin of Volcanology, 51*(1), 51-68.

Harris, H., Ripepe, M., Calvari, S., Lodato, L., & Spampinato, L. (2008). The 5 April 2003 explosion of Stromboli: timing of eruption dynamics using thermal data. In *The Stromboli Volcano: An integrated study of the 2002-2003 Eruption*. American Geophysical Union.

Head, J. W., & Wilson, L. (1989). Basaltic pyroclastic eruptions: influence of gas-release patterns and volume fluxes on fountain structure, and the formation of cinder cones, spatter cones, rootless flows, lava ponds and lava flows. *Journal of Volcanology and Geothermal Research, 37*(3-4), 261-271.

Herd, R. A., & Pinkerton, H. (1997). Bubble coalescence in basaltic lava: its impact on the evolution of bubble populations. *Journal of Volcanology and Geothermal Research, 75*(1-2), 137-157.

Hill, G. J., Bibby, H. M., Ogawa, Y., Wallin, E. L., Bennie, S. L., Caldwell, T. G., Keys, H., Bertrand, E. A., & Heise, W. (2015). Structure of the Tongariro volcanic system: Insights from magnetotelluric imaging. *Earth and Planetary Science Letters, 432*, 115-125.

Hobden, B. J., Houghton, B. F., Lanphere, M. A., & Nairn, I. A. (1996). Growth of the Tongariro Volcanic Complex: New evidence from K-Ar age determinations. *New Zealand Journal of Geology and Geophysics, 39*(1), 151-154.

Hobden, B. J. (1997). *Modelling Magmatic Trends in Time and Space: Eruptive and Magmatic History of Tangariro Volcanic Complex, New Zealand.* PhD thesis, University of Canterbury, Christchurch.

Hobden, B. J., Houghton, B. F., Davidson, J. P., & Weaver, S. D. (1999). Small and short-lived magma batches at composite volcanoes: Time windows at Tongariro volcano, New Zealand. *Journal of the Geological Society, 156*, 865-868.

Hobden, B. J., Houghton, B. F., & Nairn, I. A. (2002). Growth of a young, frequently active composite cone: Ngauruhoe Volcano, New Zealand. *Bulletin of Volcanology, 64*(6), 392-409.

Honjo, N., Bonnichsen, B., Leeman, W. P., & Stormer, J. C. (1992). Mineralogy and geothermometry of high-temperature rhyolites from the central and western Snake River Plain. *Bulletin of Volcanology, 54*(3), 220-237.

Houghton, B., & Wilson, C. (1989). A vesicularity index for pyroclastic deposits. *Bulletin of Volcanology, 51*(6), 451-462.

Houghton, B., & Gonnermann, H. (2008). Basaltic explosive volcanism: constraints from deposits and models. *Chemie der Erde-Geochemistry, 68*(2), 117-140.

Houghton, B., & Carey, R. J. (2015). Pyroclastic fall deposits. In *The Encyclopedia of Volcanoes* (pp. 599-616). Elsevier.

Humphreys, M. C., Blundy, J. D., & Sparks, R. S. J. (2006). Magma evolution and open-system processes at Shiveluch Volcano: Insights from phenocryst zoning. *Journal of Petrology, 47*(12), 2303-2334.

Huppert, H. E., Sparks, R. S. J., & Turner, J. S. (1982). Effects of volatiles on mixing in calc-alkaline magma systems. *Nature, 297*(5867), 554.

Hurst, T., Jolly, A. D., & Sherburn, S. (2014). Precursory characteristics of the seismicity before the 6 August 2012 eruption of Tongariro volcano, North Island, New Zealand. *Journal of Volcanology and Geothermal Research, 286*, 294-302.

Jarosewich, E., Nelen, J., & Norberg, J. A. (1980). Reference samples for electron microprobe analysis. *Geostandards Newsletter, 4*(1), 43-47.

Jaupart, C., & Vergniolle, S. (1988). Laboratory models of Hawaiian and Strombolian eruptions. *Nature, 331*(6151), 58.

Jaupart, C., & Vergniolle, S. (1989). The generation and collapse of a foam layer at the roof of a basaltic magma chamber. *Journal of Fluid Mechanics, 203*, 347-380.

Johnson, J. B., Lees, J. M., & Gordeev, E. I. (1998). Degassing explosions at Karymsky volcano, Kamchatka. *Geophysical Research Letters, 25*(21), 3999-4002.

Jolly, A., Sherburn, S., Jousset, P., & Kilgour, G. (2010). Eruption source processes derived from seismic and acoustic observations of the 25 September 2007 Ruapehu eruption—North Island, New Zealand. *Journal of Volcanology and Geothermal Research, 191*(1-2), 33-45.

Jolly, A., Lokmer, I., Kennedy, B., Keys, H., Proctor, J., Lyons, J., & Jolly, G. (2014a). Active seismic sources as a proxy for seismic surface processes: An example from the 2012 Tongariro volcanic eruptions, New Zealand. *Journal of Volcanology and Geothermal Research, 286*, 317-330.

Jolly, A., Jousset, P., Lyons, J., Carniel, R., Fournier, N., Fry, B., & Miller, C. (2014b). Seismo-acoustic evidence for an avalanche driven phreatic eruption through a beheaded hydrothermal system: an example from the 2012 Tongariro eruption. *Journal of Volcanology and Geothermal Research, 286*, 331-347.

Jolly, G. E., Keys, H. J. R., Procter, J. N., & Deligne, N. I. (2014c). Overview of the co-ordinated risk-based approach to science and management response

and recovery for the 2012 eruptions of Tongariro Volcano, New Zealand. *Journal of Volcanology and Geothermal Research, 286*, 184-207.

Kennedy, B., Spieler, O., Scheu, B., Kueppers, U., Taddeucci, J., & Dingwell, D. B. (2005). Conduit implosion during Vulcanian eruptions. *Geology, 33*(7), 581-584.

Kilgour, G., Manville, V., Della Pasqua, F., Graettinger, A., Hodgson, K., & Jolly, G. (2010). The 25 September 2007 eruption of Mount Ruapehu, New Zealand: directed ballistics, surtseyan jets, and ice-slurry lahars. *Journal of Volcanology and Geothermal Research, 191*(1-2), 1-14.

Kilgour, G., Blundy, J., Cashman, K., & Mader, H. M. (2013). Small volume andesite magmas and melt–mush interactions at Ruapehu, New Zealand: evidence from melt inclusions. *Contributions to Mineralogy and Petrology, 166*(2), 371-392.

Kilgour, G. N. (2013). *Magmatic Processes at Mt. Ruapehu, New Zealand.* PhD thesis, University of Bristol, United Kingdom.

Krippner, J. B. (2009). *Ngauruhoe Inner Crater Volcanic Processes of the 1954-1955 and 1974-1975 Eruptions.* MSc thesis, University of Waikato, Hamilton.

Landi, P., Metrich, N., Bertagnini, A., & Rosi, M. (2004). Dynamics of magma mixing and degassing recorded in plagioclase at Stromboli (Aeolian Archipelago, Italy). *Contributions to Mineralogy and Petrology, 147*(2), 213-227.

Leonard, G. S., Stewart, C., Wilson, T. M., Procter, J. N., Scott, B. J., Keys, H. J., Jolly, G. E., Wardman, J. B., Cronin, S. J., & McBride, S. K. (2014). Integrating multidisciplinary science, modelling and impact data into evolving, syn-event volcanic hazard mapping and communication: A case study from the 2012 Tongariro eruption crisis, New Zealand. *Journal of Volcanology and Geothermal Research, 286*, 208-232.

Liu, E., Cashman, K., & Rust, A. (2015). Optimising shape analysis to quantify volcanic ash morphology. *GeoResJ, 8*, 14-30.

Lormand, C., Zellmer, G., Kilgour, G., Németh, K., Palmer, A., Sakamoto, N., Yurimoto, H., Kuritani, T., Iizuka, Y., & Moebis, A. (n.d.). Slow ascent of unusually hot intermediate magmas triggering Strombolian to Plinian eruptions. (Draft manuscript submitted to Journal of Petrology).

Lube, G., Cronin, S. J., Platz, T., Freundt, A., Procter, J. N., Henderson, C., & Sheridan, M. F. (2007). Flow and deposition of pyroclastic granular flows: A type example from the 1975 Ngauruhoe eruption, New Zealand. *Journal of Volcanology and Geothermal Research, 161*(3), 165-186.

Lube, G., Breard, E. C., Cronin, S. J., Procter, J. N., Brenna, M., Moebis, A., Pardo, N., Stewart, R. B., Jolly, A., & Fournier, N. (2014). Dynamics of surges

generated by hydrothermal blasts during the 6 August 2012 Te Maari eruption, Mt. Tongariro, New Zealand. *Journal of Volcanology and Geothermal Research, 286*, 348-366.

Maro, G., & Caffe, P. J. (2016). The Cerro Bitiche Andesitic Field: petrological diversity and implications for magmatic evolution of mafic volcanic centers from the northern Puna. *Bulletin of Volcanology, 78*(7), 51.

Mathews, W. H. (1967). A contribution to the geology of the Mount Tongariro massif, North Island, New Zealand. *New Zealand Journal of Geology and Geophysics, 10*(4), 1027-1039.

Miller, C. A., & Williams-Jones, G. (2016). Internal structure and volcanic hazard potential of Mt Tongariro, New Zealand, from 3D gravity and magnetic models. *Journal of Volcanology and Geothermal Research, 319*, 12-28.

Moebis, A., Cronin, S. J., Neall, V. E., & Smith, I. E. (2011). Unravelling a complex volcanic history from fine-grained, intricate Holocene ash sequences at the Tongariro Volcanic Centre, New Zealand. *Quaternary International, 246*(1), 352-363.

Moore, G., & Carmichael, I. (1998). The hydrous phase equilibria (to 3 kbar) of an andesite and basaltic andesite from western Mexico: constraints on water content and conditions of phenocryst growth. *Contributions to Mineralogy and Petrology, 130*(3-4), 304-319.

Morrisey, M., & Mastin, L. (2000). Vulcanian eruptions In H. Sigurrsson (Ed.), *Encyclopedia of Volcanoes*. Academic Press, New York.

Mount Ngauruhoe, New Zealand. (2019). Retrieved 4 February, 2019, from Google Earth, https://www.google.com/earth/.

Mueller, S., Melnik, O., Spieler, O., Scheu, B., & Dingwell, D. B. (2005). Permeability and degassing of dome lavas undergoing rapid decompression: an experimental determination. *Bulletin of Volcanology, 67*(6), 526-538.

Murphy, M., Sparks, R., Barclay, J., Carroll, M., & Brewer, T. (2000). Remobilization of andesite magma by intrusion of mafic magma at the Soufriere Hills Volcano, Montserrat, West Indies. *Journal of petrology, 41*(1), 21-42.

Nairn, I., Hewson, C., Latter, J., & Wood, C. (1976). Pyroclastic eruptions of Ngauruhoe volcano, central North Island, New Zealand, 1974 January and March. In R. W. Johnson (Ed.), *Volcanism in Australasia* (pp. 385-405). Amsterdam: Elsevier.

Nairn, I., Wood, C., & Bailey, R. (1994). The Reporoa caldera, Taupo volcanic zone: source of the Kaingaroa ignimbrites. *Bulletin of Volcanology, 56*(6-7), 529-537.

Nairn, I. A. (1976). Atmospheric shock waves and condensation clouds from Ngauruhoe explosive eruptions. *Nature, 259*(5540), 190.

Nairn, I. A., & Self, S. (1978). Explosive eruptions and pyroclastic avalanches from Ngauruhoe in February 1975. *Journal of Volcanology and Geothermal Research, 3*(1-2), 39-60.

Nelson, S. T., & Montana, A. (1992). Sieve-textured plagioclase in volcanic rocks produced by rapid decompression. *American Mineralogist, 77*(11-12), 1242-1249.

Nurfiani, D., & de Maisonneuve, C. B. (2018). Furthering the investigation of eruption styles through quantitative shape analyses of volcanic ash particles. *Journal of Volcanology and Geothermal Research, 354*, 102-114.

Pardo, N., Cronin, S. J., Németh, K., Brenna, M., Schipper, C. I., Breard, E., White, J. D., Procter, J., Stewart, B., & Agustín-Flores, J. (2014). Perils in distinguishing phreatic from phreatomagmatic ash; insights into the eruption mechanisms of the 6 August 2012 Mt. Tongariro eruption, New Zealand. *Journal of Volcanology and Geothermal Research, 286*, 397-414.

Parfitt, E., & Wilson, L. (1995). Explosive volcanic eruptions—IX. The transition between Hawaiian-style lava fountaining and Strombolian explosive activity. *Geophysical Journal International, 121*(1), 226-232.

Parfitt, E. A. (2004). A discussion of the mechanisms of explosive basaltic eruptions. *Journal of Volcanology and Geothermal Research, 134*(1-2), 77-107.

Pearce, T., Russell, J., & Wolfson, I. (1987). Laser-interference and Nomarski interference imaging of zoning profiles in plagioclase phenocrysts from the May 18, 1980, eruption of Mount St. Helens, Washington. *American Mineralogist, 72*(11-12), 1131-1143.

Pittari, A., Krippner, J. B., Briggs, R. M., & Kilgour, G. N. (2010). New perspectives on the 1954-75 summit cone of Ngauruhoe volcano. In J. D. Eccles, M. R. Grigor, P. W. O. Hoskin & D. C. H. Hikuroa (Eds.), *Abstract Volume, GeoNZ 2010 Conference, Auckland, New Zealand, 21-24 November 2010* (pp. 216). Geoscience Society of New Zealand.

Platz, T., Cronin, S. J., Cashman, K. V., Stewart, R. B., & Smith, I. E. (2007). Transition from effusive to explosive phases in andesite eruptions—A case-study from the AD1655 eruption of Mt. Taranaki, New Zealand. *Journal of Volcanology and Geothermal Research, 161*(1-2), 15-34.

Polacci, M., Burton, M. R., La Spina, A., Murè, F., Favretto, S., & Zanini, F. (2009a). The role of syn-eruptive vesiculation on explosive basaltic activity at Mt. Etna, Italy. *Journal of Volcanology and Geothermal Research, 179*(3-4), 265-269.

Polacci, M., Baker, D. R., Mancini, L., Favretto, S., & Hill, R. J. (2009b). Vesiculation in magmas from Stromboli and implications for normal Strombolian activity and paroxysmal explosions in basaltic systems. *Journal of Geophysical Research: Solid Earth, 114*(B1).

Price, R. C., Gamble, J. A., Smith, I. E. M., Stewart, R. B., Eggins, S., & Wright, I. C. (2005). An integrated model for the temporal evolution of andesites and rhyolites and crustal development in New Zealand's North Island. *Journal of Volcanology and Geothermal Research, 140*(1–3), 1-24.

Price, R. C., Turner, S., Cook, C., Hobden, B., Smith, I. E. M., Gamble, J. A., Handley, H., Maas, R., & Möbis, A. (2010). Crustal and mantle influences and U–Th–Ra disequilibrium in andesitic lavas of Ngauruhoe Volcano, New Zealand. *Chemical Geology, 277*(3), 355-373.

Procter, J., Cronin, S., Zernack, A., Lube, G., Stewart, R., Nemeth, K., & Keys, H. (2014). Debris flow evolution and the activation of an explosive hydrothermal system; Te Maari, Tongariro, New Zealand. *Journal of Volcanology and Geothermal Research, 286*, 303-316.

Putirka, K., Johnson, M., Kinzler, R., Longhi, J., & Walker, D. (1996). Thermobarometry of mafic igneous rocks based on clinopyroxene-liquid equilibria, 0–30 kbar. *Contributions to Mineralogy and Petrology, 123*(1), 92-108.

Putirka, K. (2016). *Clinopyroxene P-T* [Microsoft Excel spreadsheet]. Department of Earth and Environmental Sciences, California State University, Fresno. Retrieved 14 May, 2019, from http://www.fresnostate.edu/csm/ees/faculty-staff/putirka.html.

Putirka, K. D., Mikaelian, H., Ryerson, F., & Shaw, H. (2003). New clinopyroxene-liquid thermobarometers for mafic, evolved, and volatile-bearing lava compositions, with applications to lavas from Tibet and the Snake River Plain, Idaho. *American Mineralogist, 88*(10), 1542-1554.

Putirka, K. D. (2008). Thermometers and barometers for volcanic systems. *Reviews in Mineralogy and Geochemistry, 69*(1), 61-120.

Quantachrome Instruments. (2007). *Operating Manual for Ultrapycnometer 1000, Micro-Ultrapycnometer 1000 and Ultrafoam 1000.* Boynton Beach, FL.

Ray, D., Rajan, S., Ravindra, R., & Jana, A. (2011). Microtextural and mineral chemical analyses of andesite–dacite from Barren and Narcondam islands: Evidences for magma mixing and petrological implications. *Journal of Earth System Science, 120*(1), 145-155.

Rogan, W., & Blake, S. (1994). Trace element zonation of phenocrysts from Ngauruhoe Volcano, New Zealand: constraints on magmatic processes. *Mineral Magazine, 58*, 783-784.

Rowe, M. C., Nielsen, R. L., & Kent, A. J. (2006). Anomalously high Fe contents in rehomogenized olivine-hosted melt inclusions from oxidized magmas. *American Mineralogist, 91*(1), 82-91.

Rowland, J. V., & Sibson, R. H. (2001). Extensional fault kinematics within the Taupo Volcanic Zone, New Zealand: Soft-linked segmentation of a continental rift system. *New Zealand Journal of Geology and Geophysics, 44*(2), 271-283.

Rowlands, D., White, R., & Haines, A. (2005). Seismic tomography of the Tongariro Volcanic Centre, New Zealand. *Geophysical Journal International, 163*(3), 1180-1194.

Rutherford, M. J., Gardner, J. E., & Sigurdsson, H. (2000). Rates of magma ascent. *Encyclopedia of Volcanoes*, 207-217.

Sanders, F. (2010). *Rheology and Flow Emplacement Processes of the 1954 Lavas, Mount Ngauruhoe.* MSc thesis, University of Waikato, Hamilton.

Sas, M., Kawasaki, N., Sakamoto, N., Shane, P., Zellmer, G. F., Kent, A. J. R., & Yurimoto, H. (2019). The ion microprobe as a tool for obtaining strontium isotopes in magmatic plagioclase: A case study at Okataina Volcanic Centre, New Zealand. *Chemical Geology, 513*, 153-166.

Schipper, C. I., Mandon, C., Maksimenko, A., Castro, J. M., Conway, C. E., Hauer, P., Kirilova, M., & Kilgour, G. (2017). Vapor-phase cristobalite as a durable indicator of magmatic pore structure and halogen degassing: an example from White Island volcano (New Zealand). *Bulletin of Volcanology, 79*(10), 74.

Scott, B. (1977). *Observed activity at Ngauruhoe.* N.Z. Volcanological Record, "DSIR unpublished report". 44p.

Scott, B. J., & Potter, S. H. (2014). Aspects of historical eruptive activity and volcanic unrest at Mt. Tongariro, New Zealand: 1846–2013. *Journal of Volcanology and Geothermal Research, 286*, 263-276.

Simons, B. C. (2014). *Volcanic History and Eruption Processes of Blue Lake Crater, Tongariro.* MSc thesis, University of Waikato, Hamilton.

Sparks, R. S. J., & Wright, J. V. (1979). Welded air-fall tuffs. *Geological Society of America Special Paper, 180*, 155-166.

Sparks, S. R., Sigurdsson, H., & Wilson, L. (1977). Magma mixing: a mechanism for triggering acid explosive eruptions. *Nature, 267*(5609), 315.

Spera, F. J. (1984). Carbon dioxide in petrogenesis III: role of volatiles in the ascent of alkaline magma with special reference to xenolith-bearing mafic lavas. *Contributions to Mineralogy and Petrology, 88*(3), 217-232.

Steiner, A. (1958). Petrogenetic implications of the 1954 Ngauruhoe lava and its xenoliths. *New Zealand Journal of Geology and Geophysics, 1*(2), 325-363.

Stix, J., Torres, R. C., Narváez, L., Raigosa, J. A., Gómez, D., & Castonguay, R. (1997). A model of vulcanian eruptions at Galeras volcano, Colombia. *Journal of Volcanology and Geothermal Research, 77*(1-4), 285-303.

Stormer Jr, J. (1972). Mineralogy and petrology of the Raton-Clayton volcanic field, northeastern New Mexico. *Geological Society of America Bulletin, 83*(11), 3299-3322.

Streck, M. J., & Wacaster, S. (2006). Plagioclase and pyroxene hosted melt inclusions in basaltic andesites of the current eruption of Arenal volcano, Costa Rica. *Journal of Volcanology and Geothermal Research, 157*(1-3), 236-253.

Streck, M. J. (2008). Mineral textures and zoning as evidence for open system processes. *Reviews in Mineralogy and Geochemistry, 69*(1), 595-622.

Sumner, J., Blake, S., Matela, R., & Wolff, J. (2005). Spatter. *Journal of Volcanology and Geothermal Research, 142*(1-2), 49-65.

Sumner, J. M. (1998). Formation of clastogenic lava flows during fissure eruption and scoria cone collapse: the 1986 eruption of Izu-Oshima Volcano, eastern Japan. *Bulletin of Volcanology, 60*(3), 195-212.

Sun, C., & Liang, Y. (2017). A REE-in-plagioclase–clinopyroxene thermometer for crustal rocks. *Contributions to Mineralogy and Petrology, 172*(4), 24.

Taddeucci, J., Edmonds, M., Houghton, B., James, M. R., & Vergniolle, S. (2015). Hawaiian and Strombolian eruptions. In *The Encyclopedia of Volcanoes* (pp. 485-503). Elsevier.

Tanguy, J.-C., Ribière, C., Scarth, A., & Tjetjep, W. (1998). Victims from volcanic eruptions: a revised database. *Bulletin of Volcanology, 60*(2), 137-144.

Tepley, F., Davidson, J., & Clynne, M. (1999). Magmatic interactions as recorded in plagioclase phenocrysts of Chaos Crags, Lassen Volcanic Center, California. *Journal of Petrology, 40*(5), 787-806.

Thomas, R., & Sparks, R. (1992). Cooling of tephra during fallout from eruption columns. *Bulletin of Volcanology, 54*(7), 542-553.

Topping, W. (1973). Tephrostratigraphy and chronology of late Quaternary eruptives from the Tongariro Volcanic Centre, New Zealand. *New Zealand Journal of Geology and Geophysics, 16*(3), 397-423.

Troll, V. R., Deegan, F. M., Jolis, E. M., Harris, C., Chadwick, J. P., Gertisser, R., Schwarzkopf, L. M., Borisova, A. Y., Bindeman, I. N., Sumarti, S., & Preece, K. (2013). Magmatic differentiation processes at Merapi Volcano:

inclusion petrology and oxygen isotopes. *Journal of Volcanology and Geothermal Research, 261*(SI), 38-49.

Tsuchiyama, A. (1985). Dissolution kinetics of plagioclase in the melt of the system diopside-albite-anorthite, and origin of dusty plagioclase in andesites. *Contributions to Mineralogy and Petrology, 89*(1), 1-16.

Turner, R., Moore, S., Pardo, N., Kereszturi, G., Uddstrom, M., Hurst, T., & Cronin, S. (2014). The use of numerical weather prediction and a Lagrangian transport (NAME-III) and dispersion (ASHFALL) models to explain patterns of observed ash deposition and dispersion following the August 2012 Te Maari, New Zealand eruption. *Journal of Volcanology and Geothermal Research, 286*, 437-451.

Vance, J. A. (1965). Zoning in igneous plagioclase: patchy zoning. *The Journal of Geology, 73*(4), 636-651.

Vasseur, J., Wadsworth, F. B., Lavallée, Y., Hess, K. U., & Dingwell, D. B. (2013). Volcanic sintering: timescales of viscous densification and strength recovery. *Geophysical research letters, 40*(21), 5658-5664.

Vergniolle, S., & Jaupart, C. (1986). Separated two-phase flow and basaltic eruptions. *Journal of Geophysical Research: Solid Earth, 91*(B12), 12842-12860.

Vergniolle, S., & Jaupart, C. (1990). Dynamics of degassing at Kilauea volcano, Hawaii. *Journal of Geophysical Research: Solid Earth, 95*(B3), 2793-2809.

Vergniolle, S., & Mangan, M. (2000). Hawaiian and Strombolian Eruptions. In H. Sigurdsson (Ed.), *Encyclopedia of Volcanoes*. Academic Press, New York.

Vigouroux, N., Wallace, P. J., Williams-Jones, G., Kelley, K., Kent, A. J. R., & Williams-Jones, A. E. (2012). The sources of volatile and fluid-mobile elements in the Sunda Arc: A melt inclusion study from Kawah Ijen and Tambora volcanoes, Indonesia. *Geochemistry Geophysics Geosystems, 13*, 22.

Villamor, P., & Berryman, K. R. (2006). Evolution of the southern termination of the Taupo Rift, New Zealand. *New Zealand Journal of Geology and Geophysics, 49*(1), 23-37.

Wadsworth, F., Kennedy, B., Branney, M., von Aulock, F., Lavallée, Y., & Menendez, A. (2015). Exhumed conduit records magma ascent and drain-back during a Strombolian eruption at Tongariro Volcano, New Zealand. *Bulletin of Volcanology, 77*(9), 1-10.

Watt, S., Mather, T., & Pyle, D. (2007). Vulcanian explosion cycles: Patterns and predictability. *Geology, 35*(9), 839-842.

Williams, K. (1989). *Volcanoes of the South Wind : a Field Guide to the Volcanoes and Landscape of Tongariro National Park*. (2nd ed.). Wellington: Tongariro Natural History Society.

Wilson, C. J. N., Houghton, B. F., McWilliams, M. O., Lanphere, M. A., Weaver, S. D., & Briggs, R. M. (1995). Volcanic and structural evolution of Taupo Volcanic Zone, New Zealand: a review. *Journal of Volcanology and Geothermal Research, 68*(1), 1-28.

Wilson, L., & Head III, J. W. (1981). Ascent and eruption of basaltic magma on the Earth and Moon. *Journal of Geophysical Research: Solid Earth, 86*(B4), 2971-3001.

Winter, J. D. (2013). *Principles of Igneous and Metamorphic Petrology*. (Pearson New International ed.). Harlow, United Kingdom: Pearson Education Limited.

Wolff, J., & Sumner, J. (2000). Lava fountains and their products. In H. Sigurdsson, B. F. Houghton, S. R. McNutt, H. Rymer & J. Stix (Eds.), *Encyclopedia of Volcanoes* (pp. 321-329). San Diego, CA: Academic Press.

Wood, C. P. (1994). Mineralogy at the magma-hydrothermal system interface in andesite volcanoes, New Zealand. *Geology, 22*(1), 75-78.

Woods, A. W. (1995). A model of vulcanian explosions. *Nuclear Engineering and Design, 155*(1-2), 345-357.

Zellmer, G. F., Sakamoto, N., Matsuda, N., Iizuka, Y., Moebis, A., & Yurimoto, H. (2016). On progress and rate of the peritectic reaction Fo+ SiO_2→ En in natural andesitic arc magmas. *Geochimica et Cosmochimica Acta, 185*, 383-393.

Zobin, V. M., & Levina, V. I. (1998). Rupture history of the January 1, 1996, Ms 6.6 volcanic earthquake preceding the simultaneous eruption of Karymsky and Akademia Nauk volcanoes in Kamchatka, Russia. *Journal of Geophysical Research: Solid Earth, 103*(B8), 18315-18324.